ALMA MATER STUDIORUM
UNIVERSITÀ DI BOLOGNA

DOTTORATO DI RICERCA IN

INGEGNERIA ELETTRONICA, TELECOMUNICAZIONI E TECNOLOGIE DELL'INFORMAZIONE

Ciclo 38

Settore Concorsuale: 09/F1 - CAMPI ELETTROMAGNETICI

Settore Scientifico Disciplinare: ING-INF/02 - CAMPI ELETTROMAGNETICI

DESIGN OF RADIOFREQUENCY WIRELESS SENSING DEVICES BASED ON RESONANCE TECHNIQUES

Presentata da: Alessandra Di Florio Di Renzo

Coordinatore Dottorato

Davide Dardari

Supervisore

Alessandra Costanzo

Co-supervisore

Marco Tartagni

Esame finale anno 2026

Contents

Abstract

Microwave sensing based on resonance microwave techniques has emerged as a powerful approach to address the increasing demand for portable, cost-effective, and stand-alone diagnostic tools. By exploiting the interaction between electromagnetic (EM) fields and the material under test (MUT), these systems provide accurate and reliable information across diverse application domains. In this context, the integration of resonant structures with machine learning (ML) models plays a key role, enabling adaptive and real-time sensing while enhancing the ability to process complex and variable data.

This Thesis focuses on the design and experimental validation of microwave sensors developed for applications in precision agriculture and biomedical scenarios. In particular, novel solutions have been studied to secure the sensing accuracy and at the same time to ensure portability of the sensing system, thus getting rid of cumbersome laboratory instruments, as is usual the case for microwave sensing scenarios.

Two sensing approaches are studied in this Thesis: one for in-situ tree trunk moisture content monitoring, and another for skin hydration assessment. For tree trunk moisture monitoring, a low-profile self-oscillating antenna-based sensor is developed, introducing an innovative sensing strategy based on monitoring the oscillator's steady-state regimes, which vary with the antenna loads. By tracking the DC power consumption of each oscillator regime only, this approach provides a robust

alternative to conventional and cumbersome radiofrequency (RF) measurement instruments. In the biomedical domain, non-invasive and electrode-less resonators are developed to assess skin hydration for different operating frequency. In particular a high-resolution resonator is designed to isolate and characterize the most superficial, non-vascularized layer of the skin, enabling the detection of microscopic fissures associated with atopic dermatitis (AD).

The design of each sensor, including the choice of operating frequency and resonant structure, is driven by the required field penetration depth.

The presented systems are compact, cost-effective, and demonstrate the effectiveness of combining resonance-based microwave sensing with machine learning, enabling robust, autonomous, and adaptable diagnostic platforms for a wide range of applications.

List of Acronyms

Acronyms	**Explanation**
AD	Atopic Dermatitis
BIA	Bioelectrical Impedance Analysis
BJT	Bipolar Junction Transistor
CSRR	Complementary Split-Ring Resonator
DC	Direct Current
DR	Dermis
EM	Electromagnetic
EP	Epidermis
FN	False Negative
FP	False Positive
HB	Harmonic Balance

Acronyms	**Explanation**
IoT	Internet of Things
ISM	Industrial, Scientific, and Medical (band)
LVs	Latent Variables
MC	Moisture Content
ML	Machine Learning
MUT	Material Under Test
nanoVNA	Nano Vector Network Analyzer
NIPALS	Nonlinear Iterative Partial Least Squares
PCA	Principal Component Analysis
PLSR	Partial Least Squares Regression
pHEMT	Pseudomorphic High Electron Mobility Transistor
PCB	Printed Circuit Board
PET	Polyethylene Terephthalate
PVC	Polyvinyl Chloride
Q	Quality Factor
Q-point	Quiescent Point

Acronyms	**Explanation**
RMSEC	Root Mean Square Error of Calibration
RMSECV	Root Mean Square Error of Cross-Validation
SC	Stratum Corneum
SRR	Split-Ring Resonator
SWaP-C	Size, Weight, Power, and Cost
TEWL	Transepidermal Water Loss
TN	True Negative
TP	True Positive
VNA	Vector Network Analyzer
WSN	Wireless Sensor Network

List of Figures

List of Tables

Chapter 1

Introduction

Microwave sensing based on resonance techniques has recently emerged as a reliable, non-invasive, solution to allow for real-time and accurate monitoring of materials across a wide range of applications, including biological monitoring, precision agriculture, structural health assessment, and environmental sensing. The ability of electromagnetic waves to penetrate materials allows the extraction of crucial information without damaging the sample, making microwave sensors particularly attractive for on-field and wearable applications. Moreover, these sensors are compact, cost-effective and easy to manufacture, aligning with the increasing demand for portable and stand-alone diagnostic devices [1–5].

In agricultural applications, monitoring the moisture content of tree trunks is crucial for maintaining plant health, facilitating cellular processes, and supporting sustainable growth, particularly under changing climate conditions. Similarly, in biomedical applications, monitoring skin hydration levels is of particular interest, as deviations from normal hydration can impair cognitive and physical abilities and contribute to dermatological conditions such as burns, edema, inflammation, and atopic dermatitis.

Nonetheless significant challenges remain, as conventional resonator-based systems typically rely on bulky, laboratory-based, or invasive instruments, which are incompatible with IoT and SWaP-C (Size, Weight, Power, and Cost) requirements, limiting their applicability in real-time, in-field, or wearable scenarios. Furthermore, most existing skin sensors are subject to measurement variability caused by external factors, including sensor pressure, skin deformation, and sweating, which can compromise the accuracy and reliability of the readout. In addition, they often lack the spatial resolution necessary to discriminate multilayered structures or detect biomarkers associated with conditions such as atopic dermatitis.

This thesis aims to overcome these challenges by developing and experimentally validating autonomous microwave sensors tailored for both agricultural and biomedical applications. These sensors exploit resonance-based sensing principles in combination with low-complexity machine learning models to provide compact, cost-effective, real-time monitoring solutions. The proposed devices are validated by rigorous circuital and electromagnetic simulations, followed by the fabrication process and experimental campaign. The development of the predictive models presented in this thesis has been carried out in close collaboration with Professor Marco Tartagni's research group.

1.1 Self-Oscillating Antenna for Tree-Trunk Moisture Content Monitoring

In recent years, microwave-based moisture content sensors have gained increasing interest, as they enable the acquisition of critical information in a non-destructive manner and with high sensitivity. Traditional approaches typically employ resonant structures, such as split ring resonators (SRRs) or open-end probes, connected to vector network analyzers (VNAs) or spectrum analyzers to monitor shifts in resonance frequency or output power. However, these solutions are bulky, expensive, and unsuitable for IoT deployment [6, 7].

To overcome these limitations, this Thesis introduces a compact, lightweight, and stand-alone self-oscillating antenna, operating in the 2.4 GHz band, capable of monitoring tree trunk moisture content. The operating principle is based on the nonlinear relationship between the oscillator's steady-state regimes, under different loading conditions, and its DC operating points. By monitoring the DC power consumption of the self-oscillating antenna, it is possible to retrieve the correct moisture content of the wood sample with a simple microcontroller, avoiding the need for any bulky and expensive RF instrumentation [8, 9].

A combination of nonlinear and electromagnetic simulations is performed to analyze the self-oscillating antenna's behavior in both unloaded and loaded conditions across the relevant frequency range. Extensive experimental campaigns validated that the moisture content of the wood could be accurately inferred by observing only the static drain current. The robustness of the sensor in varying in-vivo conditions is enhanced through the integration of partial least squares regression (PLSR), a low-computational machine learning method capable of handling small datasets, managing missing values, and extracting latent features from raw DC power measurements. This represents the first demonstration of a portable microwave moisture sensor assisted by machine learning, fully compatible with IoT constraints.

Building on this technology, ongoing work is exploring its extension to biomedical and sport-related applications, where non-invasive and localized monitoring of tissue hydration and other tissue characteristics could provide new insights and practical tools for real-time physiological assessment.

1.2 Resonator-Based Sensor for Skin Hydration Monitoring

The application of microwave sensors in biomedical fields has been growing, due to their non-invasive nature, use of non-ionizing radiation, and cost-effective fabrication. Accurate measurement of skin hydration is crucial for maintaining overall health, as deviations in epidermal water content are associated with various disorders, including burns, edema, inflammation, and even skin cancer. Several technologies have been proposed in the literature or assessing skin hydration status. However, these approaches are often costly and not easily accessible. In addition, their implementation in routine screening is limited by the large size and non-portable nature of the devices [10–12]. Moreover, most of these methods do not incorporate machine learning algorithms, which could enhance their accuracy.

This Thesis presents a resonator-based skin hydration sensor employing a low-cost complementary split-ring-resonator (CSRR) operating in the 2-3 GHz frequency band. The sensor is integrated with machine learning algorithms to classify hydration levels directly from skin measurements, thereby enabling real-time and automatic monitoring. The system is non-invasive, portable and wearable, demonstrating the feasibility of combining microwave sensing with low-complexity data processing for biomedical applications [13, 14].

1.3 High-Resolution Resonator for Atopic Dermatitis Detection

Atopic dermatitis is a common skin condition affecting hundreds of millions of people worldwide. One of its key features is the structural and functional impairment of the *stratum corneum* (SC), the outermost layer of the skin, leading to increased trans-epidermal water loss (TEWL), dryness, inflammation, and susceptibility to infection [15]. Most existing skin sensors treat the skin as a single and homogeneous layer, neglecting its multilayered structure, including the *stratum corneum* (SC), epidermis (EP), and dermis (DR). Some studies specifically focus on the SC, however, literature lacks well defined dehydration threshold or quantitative hydration values specific to AD affected skin, making it difficult to distinguish between normal and pathological dryness [16, 17].

To overcome these limitations, this Thesis introduces a novel high-resolution EM sensing approach capable of probing the superficial, non-vascularized layers of the skin, where AD biomarkers are localized. The proposed system detects local EM variations induced by structural alterations in the *stratum corneum* caused by atopic dermatitis. These alterations serve as specific markers of the AD rather that general indicators of hydration or dryness. The system is designed for non-invasive and cost-effective monitoring of AD-related alterations, providing a more specific and reliable detection of AD-induced structural changes in the skin. [18].

Chapter 2

Predictive-Model-Assisted Self-Oscillating Antenna for Moisture Content Sensing

This Chapter is based on the following publications:

A. Di Florio Di Renzo, S. Trovarello, O. Afif, M. Tartagni, D. Masotti and A. Costanzo, "A Predictive-Model-Assisted Moisture Content Sensor by Monitoring the DC-Unstable States of a Microwave Self-Oscillating Antenna," in *IEEE Transactions on Microwave Theory and Techniques*, vol. 73, no. 8, pp. 5580-5591, Aug. 2025.

A. Di Florio Di Renzo et al., "A Stand-Alone Moisture Content Sensor Based on a Loaded Self-Oscillating Antenna," in *2024 IEEE/MTT-S International Microwave Symposium - IMS 2024*, Washington, DC, USA, 2024, pp. 284-287.

2.1 Introduction of the Chapter

The continuous expansion of the Internet of Things (IoT) and wireless sensor networks (WSNs) is deeply transforming the way the physical world is observed and interpreted. In fact, the next generation of IoT devices will increasingly rely on compact, low-cost, and portable solutions, as these characteristics are essential for guaranteeing scalability in real-world deployment scenario. Typical applications range from structural and biomedical monitoring to smart home systems and precision agriculture, where many sensors must cooperate autonomously and reliably to provide meaningful information about the surrounding environment. Through widespread and distributed data collection, WSNs enable real-time understanding of environmental dynamics, thereby supporting smarter and more sustainable resource management [19].

Given the intensifying climate crisis, monitoring the water content of trees has become essential, as it plays a decisive role in preserving plant health, maintaining cellular functionality, ensuring leaf turgidity, and supporting overall plant growth [20]. Accordingly, in recent years, the use of sensors for real-time plant hydration monitoring has gained increasing importance. Conventional technologies for measuring moisture content typically rely on resistive or capacitive methods. Resistive sensors estimate moisture by detecting changes in electrical resistance between inserted probes, which vary with humidity. However, they are invasive, as the insertion of probes causes physical damage to the material. Additionally, these sensors tend to degrade over time, since electrodes exposed to humidity are prone to corrosion, resulting in reduced measurement accuracy. Capacitive sensors, in contrast, retrieve moisture content information by tracking variations in capacitance between two electrodes that embed the sample. Although these sensors are generally considered non-invasive, their use is limited to surface-level monitoring due to their superficial penetration depth of less than 10 mm. In trees, this limitation confines the sensor's sensitivity to the outermost layers beneath the bark, preventing a comprehensive assessment of the internal hydration state [21].

For these reasons, microwave-based approaches have been widely investigated in the literature as promising alternatives. Thanks to their ability to penetrate materials, electromagnetic waves enable the non-destructive acquisition of moisture-related information. Several implementations have been proposed, including sensors based on resonant components, such as SRRs or open-end probes. These architectures typically operate by detecting shifts in resonance frequency and return loss under varying loading conditions using RF measurements. In addition, oscillator-based microwave sensors have been developed for material characterization, where changes in oscillation frequency or output power are analyzed with external RF instruments, such as vector VNAs or spectrum analyzers. Despite their high sensitivity, such solutions are not fully compatible with IoT-oriented applications, as they rely on bulky and expensive instrumentation, which significantly increases the overall size, weight, power consumption, and cost of the system. Attempts have been made to partially overcome these limitations by incorporating additional circuitry to convert RF signals into DC values; however, this approach increases system complexity and reduces suitability for large-scale deployment [22–27].

This work addresses the challenges of moisture content (MC) sensing by developing a compact, lightweight, and stand-alone system. The architecture is based on a self-oscillating antenna operating in the 2.4 GHz band, which is placed directly in contact with the tree trunk. The operating principle exploits the nonlinear relationship between the oscillator's steady-state regimes under different loading conditions and its DC operating point. In particular, sensing is performed by monitoring only the DC drain-source driven current value, which reflects how the antenna's loading conditions, governed by the moisture-dependent dielectric properties of the wood, affect the oscillator steady-state behavior. The direct coupling between oscillator and antenna, with the antenna acting as a dispersive load, provides two main advantages: it relaxes constraints on oscillation conditions, thanks to the lower quality factor compared to a common split resonator, and it allows deeper penetration of wave inside the wood, enabling the detection of internal moisture.

Extensive theoretical and simulation analyses are conducted to characterize the system under different loading conditions. Experimental results confirm that varying hydration levels can be distinguished simply by monitoring the static drain current, without the need for complex RF measurement equipment. This approach ensures non-invasive operation and allows access to internal moisture information, avoiding destructive sampling or drilling. Such capability is particularly valuable for assessing tree health and detecting early signs of internal decay. To address the variability in in-vivo scenarios, where both the material's electrical characteristics and ambient conditions fluctuate, raw DC power data alone is insufficient for precise MC identification. To overcome this limitation, partial least squares regression is employed. PLSR is particularly suited for modeling the relationship between environmental factors and moisture content in wood, as it can handle small datasets, accommodate missing values, and identify latent variables that capture the underlying data variance [28–30]. This capability enables real-time MC prediction, extracting insights from raw data that are otherwise remain imperceptible.

This research presents the first demonstration of a fully portable microwave moisture content sensor, enhanced with low-computational machine learning techniques capable of distinguishing different hydration states of tree trunks. The system seamlessly converts the RF sensing signal into DC information, eliminating the need for RF instrumentation or additional external circuits, representing a significant step toward practical, IoT-ready solutions for precision agriculture, smart forestry, and sustainable environmental monitoring. A schematic overview of the complete system

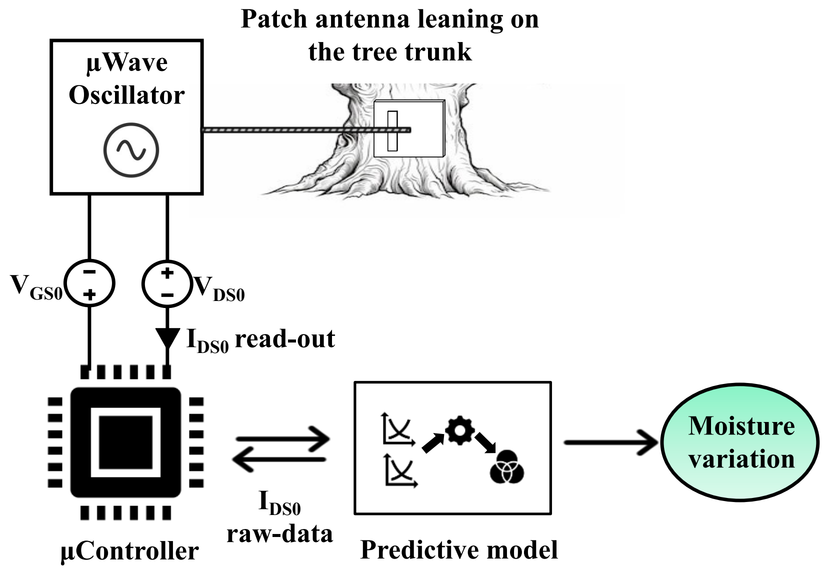

Figure 2.1: Tree trunk moisture sensor using a patch-loaded microwave oscillator, with a predictive model detecting moisture from DC current variations [9] © 2025 IEEE.

is shown in Fig. 2.1. The self-oscillating antenna, polarized with a DC gate-source voltage and a DC drain-source voltage, is directly attached to the tree-trunk. Depending on the moisture content inside the trunk, the self-oscillating antenna modifies its steady-state oscillatory regime, affecting the generated RF output power, the oscillation frequency, and the DC power consumption. By monitoring only a DC parameter, the DC driven drain-source current, the system can distinguish different levels of moisture within the tree trunk. For each moisture content level, the corresponding curve of drain-source current as function of gate-source voltage is measured and provided to a predictive model. The model exploits the entire curve shape to accurately infer the moisture content, since its shape reflects the dielectric proprieties variation of the wood with humidity. Both the read-out and the model can be implemented on a lightweight, low-cost microcontroller, eliminating the need for RF instrumentation.

2.2 Microwave Self-Oscillating Antenna: Design and Performance Evaluation

As anticipated in the introductory chapter, most microwave-based approaches presented in the literature rely on near-field resonators. While such devices provide high sensitivity, they are mainly suited for retrieving the electrical properties of thin samples. In contrast, a resonant antenna, such as a patch antenna, is more appropriate for characterizing thicker materials, since it exploits the radiative near-field. This aspect is particularly relevant in the context of moisture content detection, where MC detection may involve even larger volumes of wood.

Taking into account the typical SWaP-C constraints critical for IoT-oriented systems, a multilayer self-oscillating antenna architecture is developed. In this design, the circuit is implemented on a thin substrate (0.6 mm ROGERS4360G2, $\epsilon_r =$ 6.15, $\tan\delta = 0.0038$ at 2.45 GHz), improving field confinement and reducing fringing effects, while the antenna is realized on a thicker layer (1.52 mm ISOLA FR408HR, ϵ_r = 3.68, $\tan\delta = 0.0092$ at 2.45 GHz) to ensure good radiation. Both substrates share the same ground plane, which simplifies fabrication and reduces cost. This multilayer approach optimizes footprint, weight, power consumption, and cost, making the system well suited for compact, low-power, and cost-sensitive IoT applications.

2.2.1 Characterization of the Aperture-Coupled Patch Antenna Resonator

The selected antenna, an aperture-coupled patch, is designed to be attached to the tree trunk. Its compact profile, and low thickness make it particularly suitable for this application. The aperture-coupled patch antenna is shown in Fig. 2.2, and its dimensions are summarized in Table 2.1 (all values are given in mm).

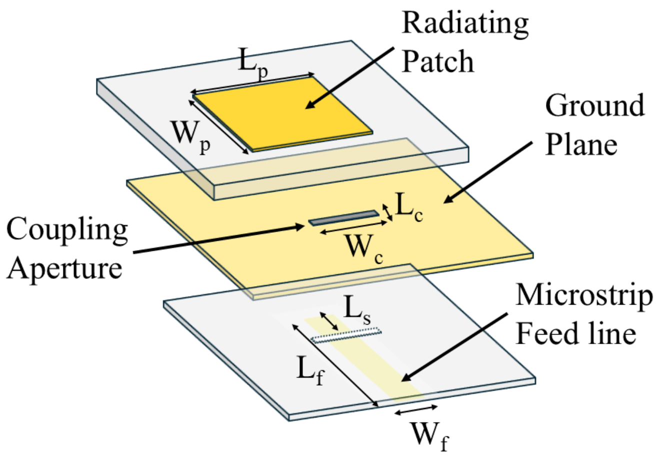

Figure 2.2: Exploded view of the aperture-coupled patch antenna structure serving as the oscillator load.

$L_p = W_p$	L_c	W_c	W_f	L_f	L_s
30.1	2.15	13.74	0.85	20	12.5

Table 2.1: Geometrical dimensions of the aperture-coupled patch antenna.

The aperture-coupled feeding scheme enables a compact dual-layer layout, where the resonant antenna is placed on the top layer, minimizing interference effects. The operating frequency is chosen within the Industrial, Scientific, and Medical (ISM) band, as a compromise between circuit miniaturization and electric field penetration in the wood.

In this application, the antenna operates in the radiative near-field region of the tree-trunk, where the electromagnetic fields are strongly influenced by the proximity of the dielectric load. In this region, parameters such as radiation patterns, gain, and efficiency are less straightforward to measure or interpret. Under this condition, the reflection coefficient is strongly sensitive to the nearby load, making it the primary parameter for assessing antenna performance directly on the tree. This approach allows monitoring how the antenna responds to variations in the trunk's dielectric properties without relying on far-field measurements.

The one-port reflection coefficient quantifies the fraction of the incident wave at the antenna port that is reflected back due to impedance mismatch. In the context of scattering parameters, the reflection coefficient at the antenna input is represented by S_{11}, defined as:

$$S_{11} = \frac{b_1}{a_1} \tag{2.1}$$

where a_1 and b_1 denote the amplitudes of the incident and reflected waves at the antenna port, respectively. Although S-parameters are generally used to describe a multi-port networks, for a single-port antenna only the diagonal element S_{11} is present.

The comparison between simulated and measured $|S_{11}|$, shown in Fig.2.3 , shows excellent agreement at the fundamental operating frequency of 2.45 GHz, while a less precise but still acceptable agreement is observed at higher harmonics.

In self-oscillating designs, resonators such as split-ring resonators or complementary split ring resonators are commonly employed as the sensing element due to their favorable sensing properties. These structures exhibit a high quality factor (Q), resulting in sharp resonance peaks and high sensitivity to small variations in the surrounding environment. Their reactive near-field is strongly confined, allowing precise detection of materials located adjacent to the resonator. However, for applications requiring penetration beyond the surface layer of a wooden trunk, patch antennas are preferred, as their radiative near-field penetrates deeper into the the wood, whereas the reactive near-field of SRRs, or CSRRs interacts only with very thin layer near the surface, providing limited sensitivity to deeper regions. To further investigate this behavior, a comparison with a CSRR is carried out, both

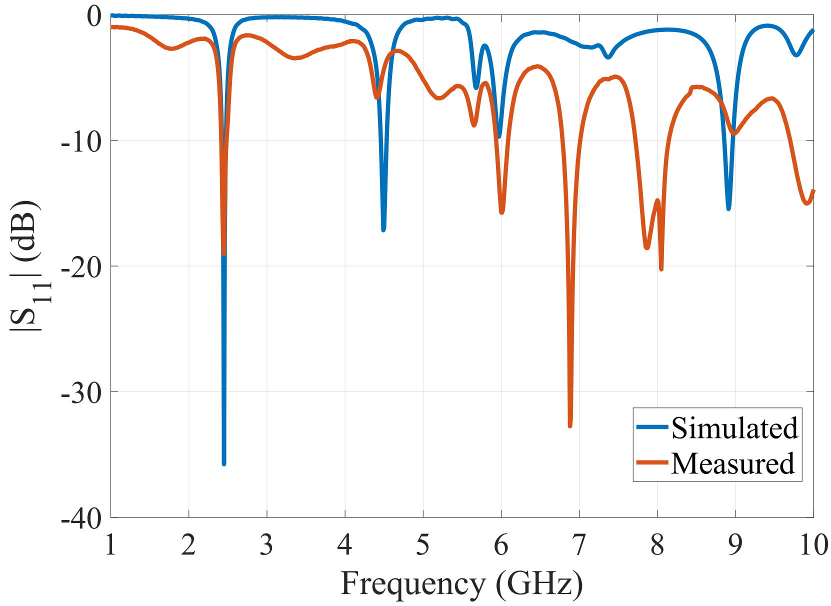

Figure 2.3: Comparison of simulated and measured $|S_{11}|$ of the patch antenna in free-space, intended as the oscillator load, over the 1–10 GHz frequency range, covering up to the fourth harmonic of the oscillator [9] © 2025 IEEE.

designed to operate at the same frequency. A detailed description of the CSRR structure, which has been tuned to operate in vacuum, will be provided in the following chapter. Each device is tested using a wooden block phantom measuring 95 x 95 x 150 mm^3, with a relative permittivity of $\epsilon_r = 2.33$ when dry and $\epsilon_r = 11.3$ when wet, and the corresponding loss tangent of $\tan\delta = 0.013$ and 0.22, at 2.45 GHz, respectively, as reported in [31]. Electromagnetic simulations performed in CST Microwave Studio highlighted the different behavior of the two resonators.

The mean value of the discrete samples of the electric field norm, taken over an area in the XY-plane, is monitored along the Z-direction, which corresponds to the penetration depth inside the material, at different penetration levels z_k. For consistency, the same area, corresponding to the dimensions of the patch antenna, is considered for both the CSRR and the patch antenna, as it is larger than the area circumscribed around the CSRR and thus adequately covers both cases. The result-

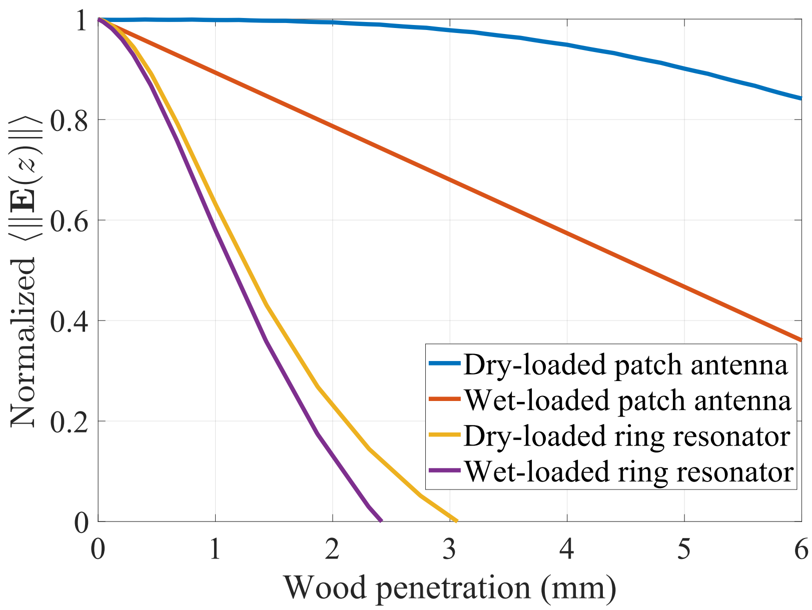

Figure 2.4: EM simulation of the mean value of the normalized E-field norm within a wood sample, excited by a patch antenna and a CSRR resonator, at 2.45 GHz for varying moisture levels [9] © 2025 IEEE.

ing values are normalized to their respective maxima, since the different structures exhibit different field intensities, and calculated as:

$$\langle \|\mathbf{E}(z_k)\| \rangle = \frac{1}{N_x N_y} \sum_{i=1}^{N_x} \sum_{j=1}^{N_y} \frac{\|\mathbf{E}(x_i, y_j, z_k)\|}{\max_k \|\mathbf{E}(z_k)\|} \tag{2.2}$$

where N_x and N_y are the number of cells along the X- and Y- directions, respectively, and z_k denotes the longitudinal position of the k-th XY-plane. As illustrated in Fig. 2.4, the normalized mean E-field inside the wooden block decreases much more rapidly when excited by the CSRR, becoming negligible after approximately 2.5 mm in wet wood and 3 mm in dry wood. In contrast, the aperture-coupled patch antenna preserves a significant E-field intensity beyond 3 mm in both conditions, confirming its superior ability to probe deeper regions of the material and thus to sense thicker volumes.

To validate the extended penetration depth of the electric field excited by the

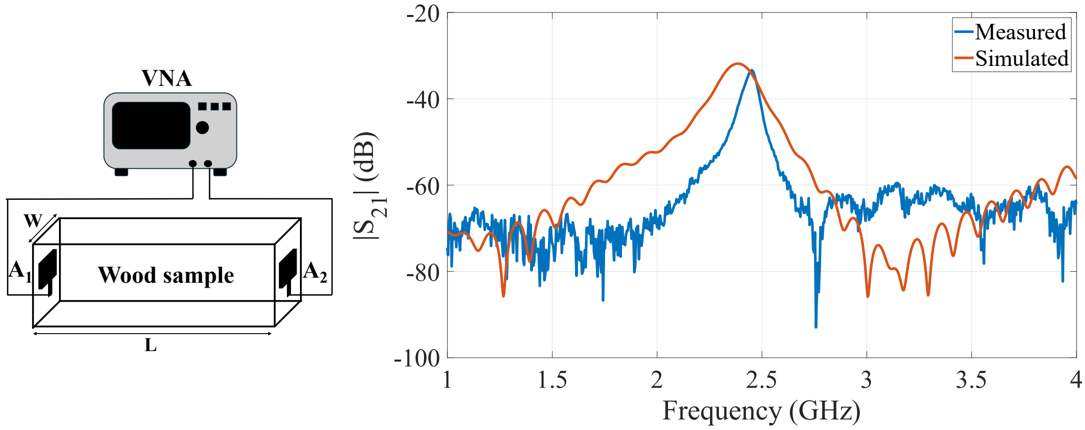

Figure 2.5: (a) Experimental setup and (b) measured transmission coefficient ($|S_{21}|$) of a wireless link formed by two aperture-coupled patch antennas positioned face-to-face on opposite sides of a 150 mm thick dry-wood block [9] © 2025 IEEE.

patch antenna inside the wood, an experiment is carried out in which two identical aperture-coupled antennas are placed face-to-face on opposite sides of a 150 mm dry-wood block ($\epsilon_r = 2.33$, $\tan\delta = 0.013$, at 2.45 GHz), thus establishing a wireless link through the material. The measurement setup and the corresponding transmission coefficient $|S_{21}|$ are shown in Fig.2.5, compared with the results obtained from EM simulations. The parameter $|S_{21}|$ represents the transmission from port 1 to port 2, providing a direct indication of the efficiency with which the electromagnetic field propagates through the sample. A satisfactory agreement between simulation and measurement is observed around the operating frequency, although a slight difference in the resonant frequency can be noticed. This discrepancy is attributed to the fact that the dielectric properties of wood used in the simulations are taken from literature, whereas the actual material employed in the measurements may exhibits slightly different permittivity values. Since the same wood sample is used throughout the experimental campaign, the measured data are considered more representative of its true EM behavior. At the resonant frequency, the measured transmission coefficient $|S_{21}|$ reaches $-33\,\mathrm{dB}$. Despite the relatively high losses of the wooden material, a clear coupling between the two antennas is still observed. The introduction of the wooden block leads to a resonant frequency shift of 70 MHz compared to the free-space case, and a reduction in the transmitted signal, due to the dielectric absorption and to the impedance mismatch between the antenna and the load. Regardless of these degradations, the persistence of a distinct transmission peak confirms that the electromagnetic field effectively penetrates the block and interacts with its entire volume, thus supporting the validity of the proposed sensing approach.

In practical applications, the cylindrical shape of tree trunks introduces natural curvatures that may affect the performance of planar and rigid sensors. In particular, the imperfect contact between a flat sensing surface and the curved bark could lead to small air gaps, potentially influencing the electromagnetic coupling and, consequently, the accuracy of the measurements. For this reason, it is crucial to evaluate the robustness of the proposed system with respect to variations in trunk curvature and diameter.

For this purpose, numerical simulations are performed using dry-wood cylindrical models with diameters ranging from 10 mm to 200 mm. The results, reported in Fig. 2.6, show that the shift in resonant frequency between the smallest diameter case and the ideal flat configuration is approximately 15 MHz. In addition, the effect of trunk curvature on the reflection coefficient magnitude is found to be limited, with only minor variations observed over the considered diameter range. This relatively minor deviation highlights the robustness of the antenna and confirms its suitability even for slender trunks, where curvature effects are most pronounced. Moreover, to account for possible air gaps arising not only from curvature but also from surface irregularities of the trunk, additional numerical simulations are carried out by in-

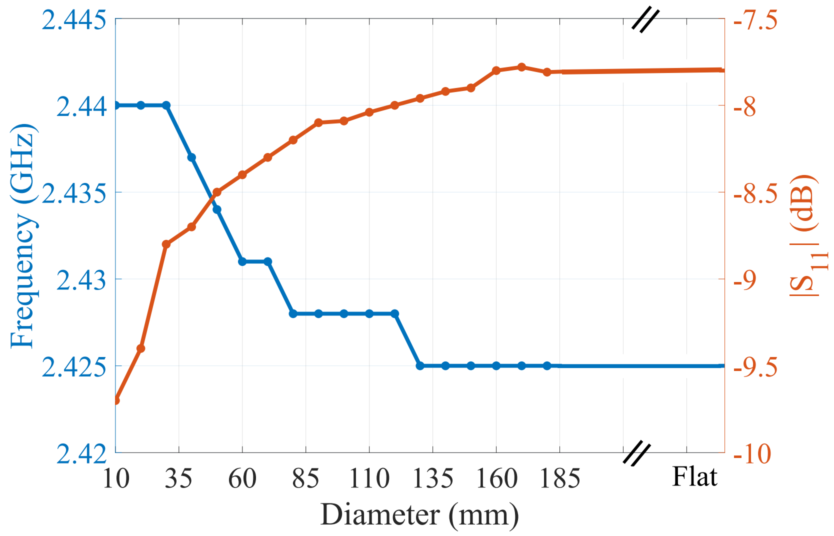

Figure 2.6: Variation of the predicted resonant frequency and $|S_{11}|$ of the proposed aperture-coupled patch antenna as a function of dry-wood sample diameter [9]

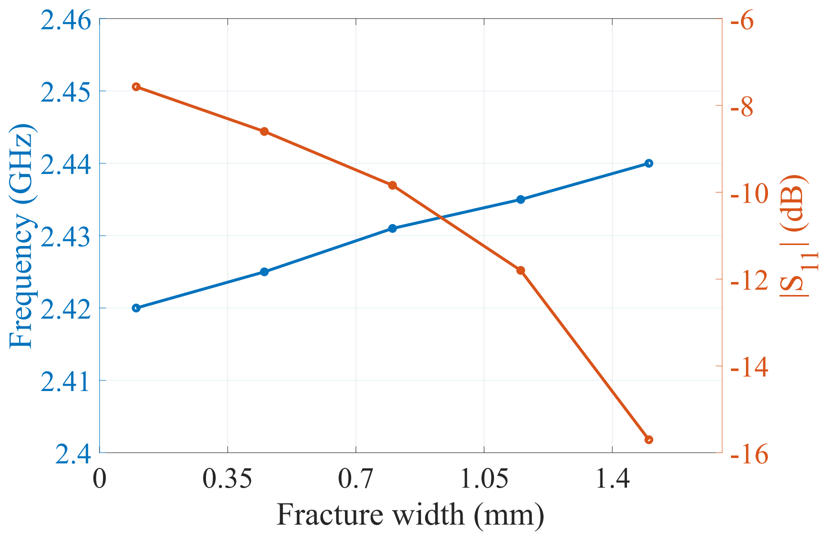

Figure 2.7: Variation of the predicted resonant frequency and $|S_{11}|$ of the proposed aperture-coupled patch antenna as a function of the air-gap (fracture) width in the dry-wood sample.

troducing a periodic distribution of air-filled fractures within the wood sample. The air-filled fractures span the entire YZ cross-section of the sample and are periodically repeated along the X-direction, so that varying the fracture width effectively controls the volumetric fraction of air. The results, reported in Fig. 2.7, show that as the fracture width increases, both the resonant frequency and the $|S_{11}|$ progressively approach the free-space response, consistent with the increasing dominance of air in the effective medium. Conversely, narrow fractures, corresponding to a low air fraction, result in an antenna response very close to that obtained with a homogeneous dry-wood load. In all cases, the observed variations remain small, indicating that moderate air gaps may result only in a slight underestimation of the effective dielectric permittivity and loss tangent. In all cases, the observed variations remain limited, indicating that moderate air gaps lead only to a slight underestimation of the effective dielectric permittivity and loss tangent. Based on these results, the assumption of a flat and continuous wood surface is therefore considered adequate for this thesis work.

2.2.2 Design of the Self-Oscillating Loaded Antenna: NL/EM Co-Design Approach

A Microstrip oscillator based on the ROGERS4360G2 substrate is designed using Harmonic Balance (HB) simulations [32–34]. The selected active component is the SAV-331+, a depletion-mode pHEMT manufactured by Mini-Circuit. A pHEMT device is chosen due to its superior efficiency, output power, and frequency stability compared to alternative devices, such as BJTs [35]. The circuit schematic is presented in Fig.2.8. The pHEMT is embedded in a microstrip layout comprising a stub matching network at the drain port, two capacitive stubs at the source terminal and an inductive stub at the gate, forming the feedback network.

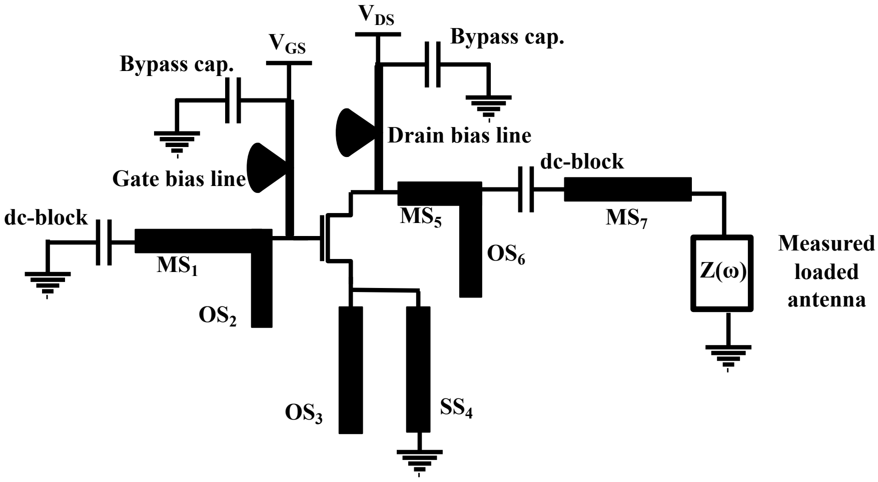

Figure 2.8: Schematic circuit of the proposed system [9] © 2025 IEEE.

The design variables includes the widths (w) and the lengths (l) of the microstrip lines, as well as the external gate and drain biases. Frequency tuning is achieved using the gate and source open stubs, combined with gate bias adjustments. The output network is designed in conjunction with the other active antenna subcircuits to simultaneously optimize the RF output power (i.e., the antenna input power) and the oscillator stability range under varying antenna loading conditions. To achieve this, the output network is co-designed with the oscillator and incorporated into the overall optimization process. This approach ensures stable RF oscillations and high DC-to-RF conversion efficiency across all antenna loads of interest, despite the significantly different equivalent load impedance values resulting from varying moisture conditions.

Before connecting the dispersive antenna load, the oscillator is first evaluated using a standard $50\,\Omega$ termination. This preliminary step allows a precise assessment of the loop gain and phase and provides a baseline for verifying the conditions required for oscillation. The design procedure is based on the Barkhausen criterion, which states that the steady-state oscillations occur when the loop gain magnitude is unity and the total phase shift around the feedback loop is $0°$ or an integer multiple

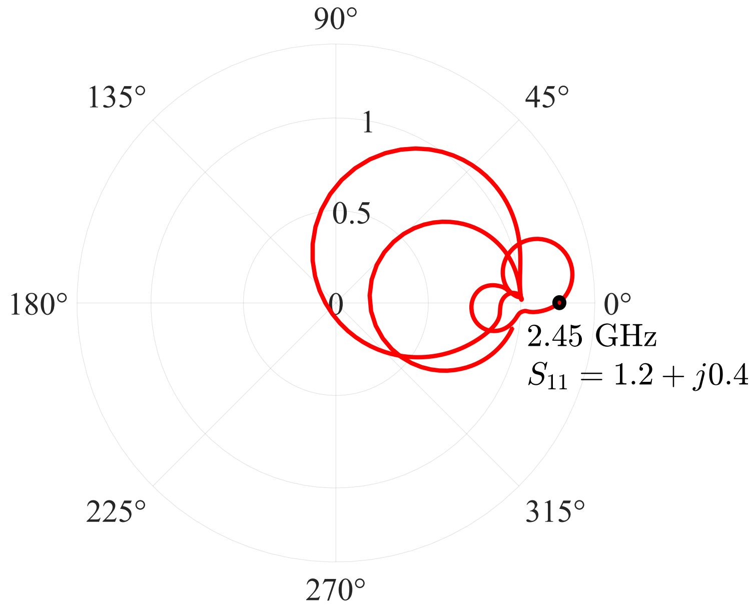

Figure 2.9: Nyquist plot of the oscillator with a 50Ω load. At 2.45 GHz, the loop gain is 1.26 with phase equal to 18°, satisfying the Barkhausen criterion and confirming stable oscillation.

of 360°. In mathematical terms, this condition can be expressed as:

$$|\beta(j\omega_0)A_v(j\omega_0)| = 1, \quad \angle\big(\beta(j\omega_0)A_v(j\omega_0)\big) = 2\pi n, \quad n \in \mathbb{Z}. \tag{2.3}$$

where $\beta(j\omega_0)A_v(j\omega_0)$ denotes the loop gain at the oscillation angular frequency ω_0. This condition can be derived from the classical feedback oscillator model, in which $A_v(j\omega)$ represents the amplifier gain and $\beta(j\omega)$ the feedback network. In the absence of an external input signal, the closed-loop transfer function requires its denominator to vanish, leading to the fundamental relation:

$$1 - \beta(j\omega)A_v(j\omega) = 0 \;\;\Rightarrow\;\; \beta(j\omega)A_v(j\omega) = 1 \tag{2.4}$$

This condition corresponds to a pair of complex-conjugate poles entering the right-half plane (RHP), indicating that the feedback is sufficient to sustain oscillations.

To systematically assess these conditions in practice, the loop gain is evaluated using a small-signal loop-breaking methodology. The oscillator loop is conceptually opened at a point in the feedback path where the signal propagates along a single path and the source impedance is much smaller than the load impedance. A small-signal perturbation is injected at this point, and the returning wave is measured. Under these conditions, the loop gain is directly obtained as a one-port scattering parameter. In this configuration, S_{11} is equivalent to the loop gain product $\beta(j\omega_0)A_v(j\omega_0)$, allowing verification of the Barkhausen criterion without explicitly separating the amplifier and feedback networks. The resulting S_{11} inherently contains both magnitude and phase information as a function of frequency and is therefore directly suitable for representation on a polar or Nyquist diagram. The Nyquist diagram provides a systematic approach to verify whether the oscillation condition is satisfied. In particular, clockwise encirclements of the critical point $1 + j0$ indicates the presence of RHP poles, generated by the closed-loop system. Fig. 2.9 shows the Nyquist plot of the oscillator with $50\,\Omega$ load.
At 2.45 GHz, the loop-gain magnitude and phase, computed as:

$$|\beta(j\omega)A_v(j\omega)| = |S_{11}| = \sqrt{\big(\mathrm{Re}\{S_{11}\}\big)^2 + \big(\mathrm{Im}\{S_{11}\}\big)^2} \tag{2.5}$$

$$\angle\big(\beta(j\omega)A_v(j\omega)\big) = \angle S_{11} = \arctan \frac{\mathrm{Im}\{S_{11}\}}{\mathrm{Re}\{S_{11}\}} \tag{2.6}$$

are 1.26 and 18°, respectively, satisfying the Barkhausen criterion and confirming that the circuit can sustain stable oscillations at the desired frequency. This preliminary evaluation ensures that the active device and feedback network are properly biased, and that the oscillator loop exhibits sufficient gain and appropriate phase conditions to initiate oscillations.

Following the preliminary optimization with the $50\,\Omega$ termination, the oscillator is connected to the patch antenna, where the output microstrip line feeds the patch antenna through aperture coupling, with the patch antenna acting as the oscillator's dispersive load. The assembly layout is shown in Fig.2.10a and a perspective view of the entire system is reported in Fig.2.10b.

To ensure proper mechanical robustness and prevent damage to the active circuitry, a multilayer structure is employed. In this configuration, only the microstrip patch, acting as the resonator, is placed in direct contact with the wood sample under different hydration conditions, while the active components and biasing network are positioned on the lower substrate layer. This arrangement guarantees that the electromagnetic interaction occurs primarily between the resonator and the wood, while simultaneously protecting the oscillator circuitry from environmental stress and mechanical contact with the sample surface.

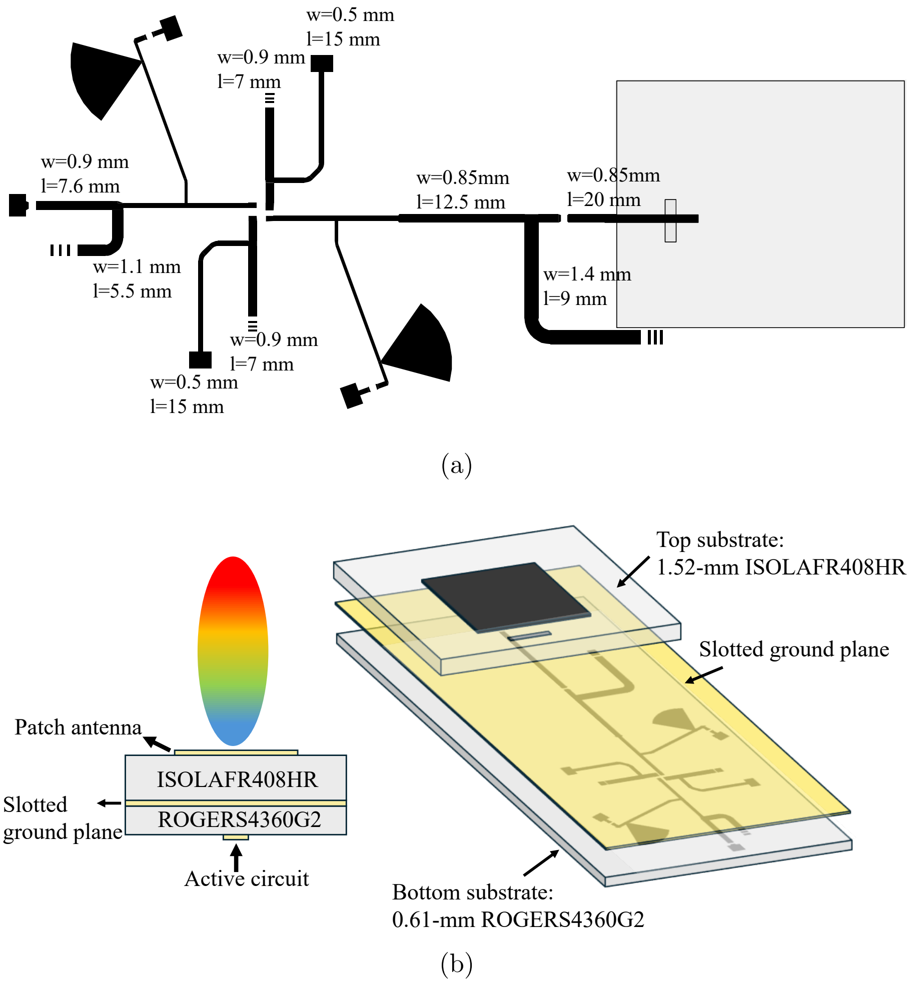

Figure 2.10: (a) Layout view of the self-oscillating antenna, with all dimensions in millimeters, and (b) 3D representation of the proposed system, showing its radiation direction. The antenna, positioned on the top substrate, is aperture-coupled to the active circuit located on the bottom substrate [9] © 2025 IEEE.

The combined use of HB simulations and full-wave electromagnetic simulations allows the characterization of the steady-state oscillatory regimes, taking into account the frequency-dependent behavior of the antenna at all harmonics of interest. The oscillator is subsequently analyzed with the antenna in free space, accounting for eight harmonics plus the DC component in HB simulations. The entire microstrip network is optimized to maximize RF output power and ensure high DC-to-RF conversion efficiency. The optimized microstrip line dimensions (in mm) are reported

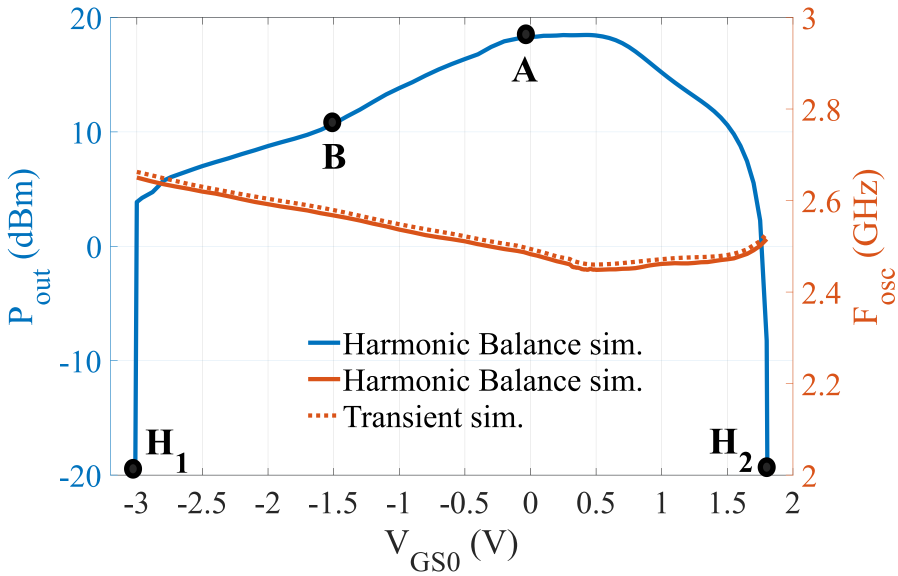

Figure 2.11: Predicted bifurcation diagram of the self-oscillating antenna for different V_{GS0} values at $V_{DS0} = 2.5$ V, and predicted tuning range and validation of the HB analysis through transient simulation. All results refer to the unloaded self-oscillating antenna [9] © 2025 IEEE.

in Fig.2.10a.

To evaluate the stability of the oscillatory regimes, a bifurcation analysis is performed by tuning the gate bias while simultaneously tracking both the oscillator frequency and the RF output power. This approach provides a convenient method to characterize circuit states using a single scalar quantity. Hopf bifurcations play a central role in this analysis, as they identify the transition points between the DC-stable and oscillatory states. Specifically, a supercritical Hopf bifurcation indicates the gradual onset of stable oscillations, whereas a subcritical Hopf bifurcation can indicate region of potential instability. Mapping these bifurcations allow the determination of safe operating regions for the oscillator and provides insight into the dynamic response of the system under varying load conditions, such as the dispersive antenna in contact with wood.

The results, depicted in Fig.2.11 , show two critical points, H_1 and H_2, corresponding to the Hopf bifurcations of the DC bias conditions [36]. The bifurcation is supercritical at H_1, while H_2 corresponds to an inverse Hopf bifurcation when V_{GS0} is increased. Along the branch H_1AH_2, all RF states are stable, including the nominal operating point A, corresponding to a DC gate-source voltage $V_{GS0} = -0.1$ V with the drain-source voltage maintained fixed at $V_{DS0} = 2.5$ V. On the contrary, all the DC states lying between H_1 and H_2 are unstable due to a couple of complex conjugate natural frequencies with positive real parts as solutions of the system characteristic equation. Oscillation buildup is ensured when V_{DS0} is fixed at 2.5 V and V_{GS0} is varied between -3.1 and 1.8 V. For the selected operating point, the maximum predicted output power, corresponding to the antenna input power, is approximately 16.4 dBm at $V_{GS0} = -0.1$ V. Fig. 2.11 illustrates the predicted tuning range of the self-oscillating antenna in free-space condition. A monotonic trend is observed for all negative values of V_{GS0}, driven by the strong nonlinear dependence of the gate-source capacitance (C_{GS}) on V_{GS0}. Oscillations are still achievable for slightly positive V_{GS0} values, though with a modified trend, as they are sustained by nonlinear reactive effects other than C_{GS}. Given the electrical characteristics of the depletion-mode device, where a positive V_{GS0} may compromise the device integrity, all subsequent measurements are performed using only non-positive V_{GS0} values.

The predicted steady-state oscillatory regimes have been validated through transient analysis. For transient analysis, a time step of 25 ps and a total simulation time of 1 ns are used. The system operates at a fundamental frequency of 2.45 GHz and accounts for harmonics up to the eighth order, corresponding to a maximum frequency of 19.6 GHz. The time step is chosen in accordance with the Nyquist-Shannon theorem, which requires a sampling interval:

$$\Delta t \leq \frac{1}{2 f_{\max}} \tag{2.7}$$

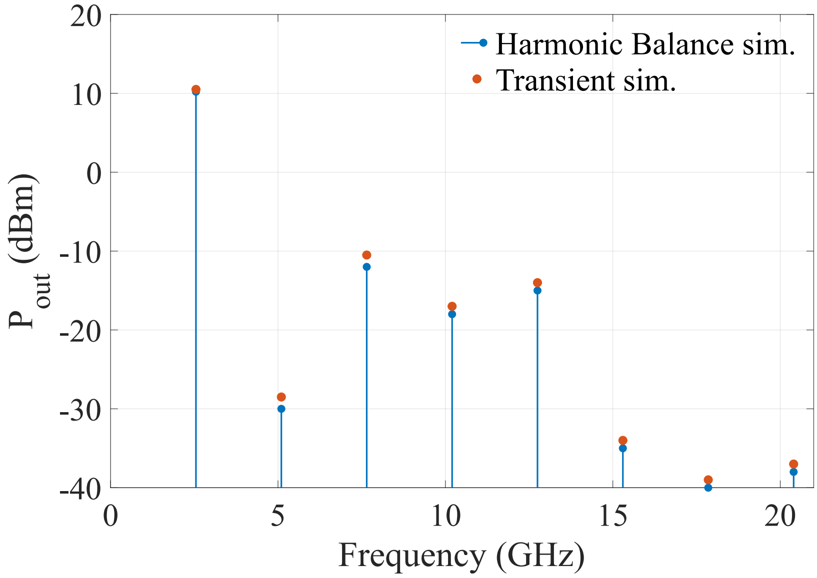

Figure 2.12: Output power spectrum of the self-oscillating antenna, computed at $V_{DS} = 2.5$ V and $V_{GS} = -1.5$ V, under unloaded conditions, with both HB and transient simulations [9] © 2025 IEEE.

to accurately represent a signal. The selected value of 25 ps, smaller than the Nyquist limit of about 25.5 ps for 19.6 GHz, ensures sufficient temporal resolution to capture both the waveform and fast transient. The total simulation time covers multiple cycles of the fundamental frequency, providing a complete evaluation of the system's dynamic behavior. Fig.2.11 compares the Self-Oscillating antenna frequency range as function of V_{GS0} for $V_{DS0} = 2.5$ V, predicted by both HB and transient simulations, showing a good agreement between the two approaches. Fig. 2.12 presents the predicted output power spectrum for a DC bias of $V_{DS0} = 2.5$ V e $V_{GS0} = -1.5$ V, corresponding to the regime "B". The results demonstrate close correspondence between the simulations. The small discrepancies are attributed to the different modeling of dispersive linear components.

2.3 Moisture Content Assessment and Analysis of the Dispersive Oscillator Load

The experimental characterization of the antenna-loaded wood specimen is carried out by systematically measuring both the moisture content ($MC_{\%}$) of the sample and the complex input impedance of the antenna throughout the drying process. This approach enables the creation of a synchronized dataset linking the temporal evolution of the wood moisture to the corresponding input impedance of the loaded antenna. The simultaneous acquisition of $MC_{\%}$ and input impedance of the wood-loaded antenna provides a solid foundation for analyzing the sensing capabilities of the Self-Oscillating Antenna. In particular, the measured input impedances serve as load conditions in the NL-EM co-simulations of the dispersive oscillator, allowing a direct correlation between the antenna response and the moisture inside the specimen.

The following analysis discusses in detail the gravimetric procedure employed to determine the moisture content and the methodology used to measure the complex input impedance of the antenna under different moisture conditions, highlighting both the measurement times and the frequency ranges considered.

2.3.1 Moisture Content Measurements by Drying Process

An independent and standardized gravimetric drying procedure is carried out to determine the MC of the wood specimen. This method, widely reported in international standards [14, 37], provides a reliable reference for subsequent validation of the sensing approach. In fact, the oven-dry technique is generally regarded as the most accurate method for determining wood moisture, since it directly measures the mass of water removed from the specimen. Unlike indirect electrical techniques, its

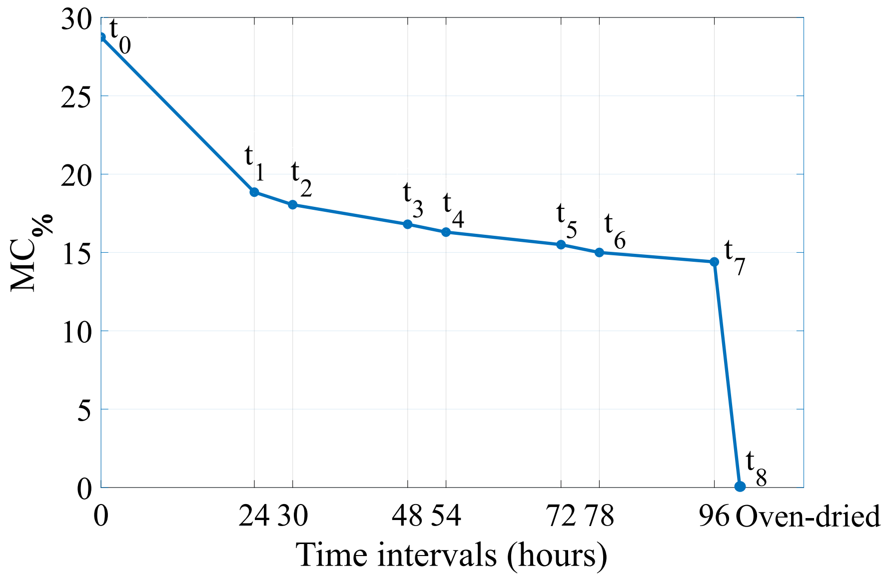

Figure 2.13: Measured $MC_{\%}$ over the 4-day drying process [9] © 2025 IEEE.

outcome is not influenced by wood species, or grain orientation, and when performed under controlled conditions it offers excellent reproducibility. For these reasons, it has been universally adopted as the reference method and is employed to validate alternative non-destructive approaches.

The moisture content percentage at a given time t_i, denoted as $MC_{\%}(t_i)$, is calculated as:

$$MC_{\%}(t_i) = \frac{m_{t_i} - m_{\text{dry}}}{m_{\text{dry}}} \cdot 100 \tag{2.8}$$

where, where m_{t_i} is the specimen mass at time t_i, and m_{dry} is the oven-dry mass. Both quantities are measured in grams (g). A standard scale with a sensitivity of 1 g has been used for the proposed measurements. The fir-wood specimen used in the study is first dried in a microwave oven for one hour, yielding an oven-dry mass of $m_{\text{dry}} = 626$ g. The same specimen is then immersed in water for three days to achieve full saturation, and its mass is recorded again. At this initial condition ($t = t_0$), the measured moisture content is $MC_{\%}(t_0) = 28.75\%$, corresponding to a mass of $m_{t_0} = 806$ g. After saturation, the specimen is left to dry at controlled room temperature for four days, with measurements taken twice daily. On the last day, an additional measurement is performed after the specimen is returned to the oven-dry state, confirming the correct determination of m_{dry}. The temporal evolution of the $MC_{\%}$ during the drying process is reported in Fig. 2.13. It should be noted that no measurement is taken between t_7 and t_8, as the specimen is transferred directly from the last room-temperature drying step to the microwave oven to reach its final oven-dry condition. Consequently, the transition from t_7 to the oven-dry state occurs in a single step.

2.3.2 The Dispersive Oscillator Load

Simultaneously with the moisture content measurements, the complex input impedance of the antenna loaded with the wood sample is measured using a VNA at the same time intervals. This procedure allowed the creation of a dataset of the corresponding scattering parameters, which is then used as the oscillator load in NL-EM co-simulations. This approach allows correlating the measured impedance variations with the oscillator's output behavior under realistic load conditions.

Measurements are performed performed not only across the fundamental frequency band but also at higher harmonics up to 20 GHz. The results are presented in Fig. 2.14, showing the real and imaginary parts of the antenna input impedance loaded with the wood sample over all time steps, from $t = t_0$, after the sample had been immersed in water for three days, to $t = t_8$, when the sample is oven-dried. For clarity,only the first three harmonics are shown. The input impedance differs significantly from the ideal $50 + j0\,\Omega$ both at the fundamental frequency and at higher harmonics, for all moisture conditions considered. At $t = t_0$, the input impedance Z_{11} is $301+j227.5\,\Omega$, while at $t = t_8$ is $78+j100\,\Omega$. It should be noted that, when the

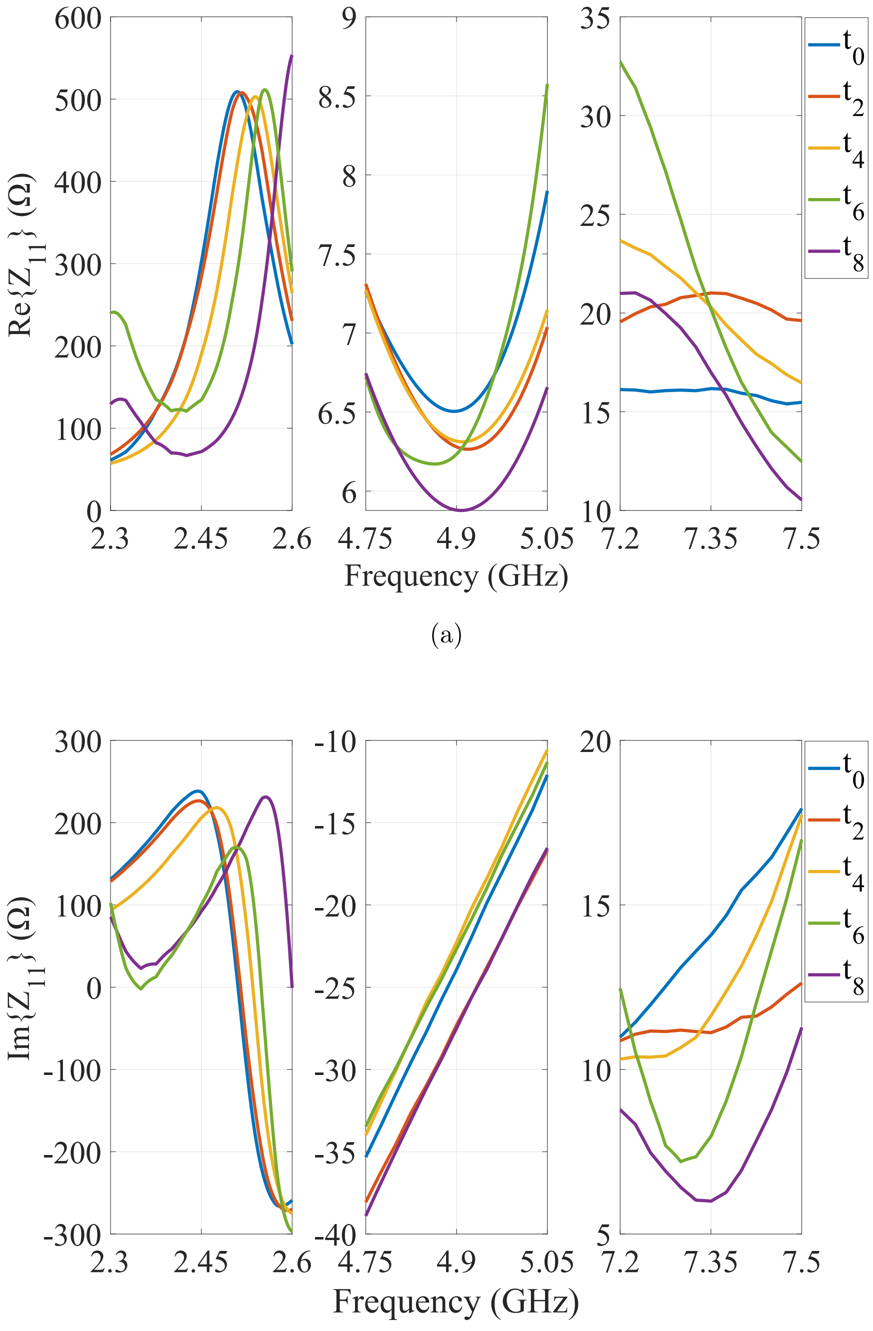

(a)

(b)

Figure 2.14: (a) Real and (b) imaginary components of the input impedance of the antenna loaded with the wood sample, measured across the frequency bands corresponding to the first three harmonics of the oscillator. Measurements are performed at multiple time intervals throughout the sample's drying process [9] © 2025 IEEE.

antenna is loaded by a wooden medium, its resulting input impedance deviates from the ideal $50 + j0\,\Omega$ condition observed in free space. The presence of the material effectively loads the antenna, thereby altering both the real and imaginary components of its input impedance. This impedance variation constitutes the fundamental operating principle of the proposed stand-alone sensor. These results confirm that the dispersive behavior of the loaded antenna enables the sensing capabilities when attached to cm-thick materials. A resonator would not differentiate moisture content effectively, as the wood surface would dry out in just a few hours. In contrast, the patch antenna can monitor humidity changes continuously over extended periods, making it suitable for thick materials.

2.4 HB Simulations of the Loaded Self-Oscillating Antenna

The experimentally measured antenna data are incorporated into the nonlinear oscillator design framework to realistically represent the actual load condition over a frequency band covering both the fundamental free-running oscillator frequency and its higher harmonics up to the eighth order. This approach accounts for the dispersive impedance behavior of the loaded antenna across all the harmonics of interest, which significantly deviates from the ideal $50\,\Omega$ reference load. By integrating experimentally derived impedance information into the HB simulations, the oscillator's performance can be predicted under realistic electromagnetic interaction conditions. Consequently, the steady-state oscillatory regime is evaluated under different scenarios corresponding to the measured moisture content levels, ranging from t_0 to t_8.

For clarity, only the two limiting cases, t_0 and t_8, are presented in Fig.2.15.

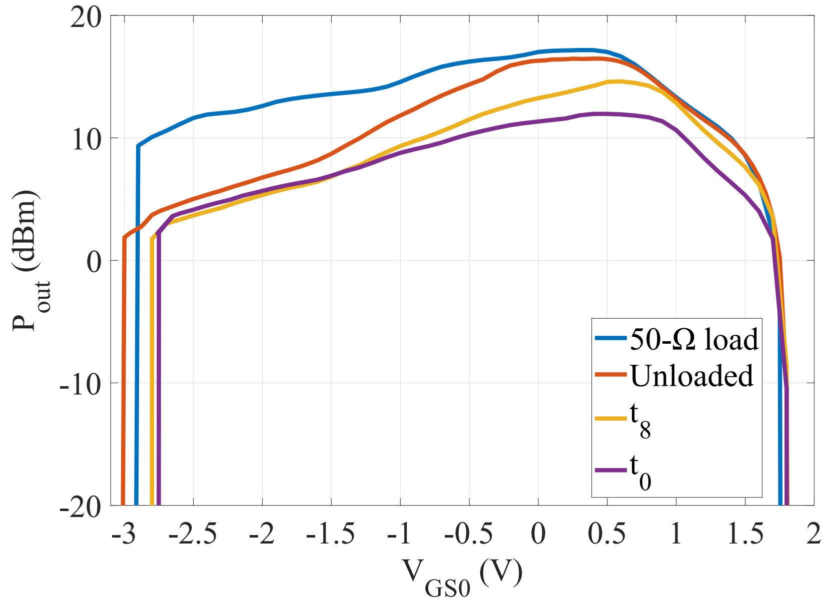

(a)

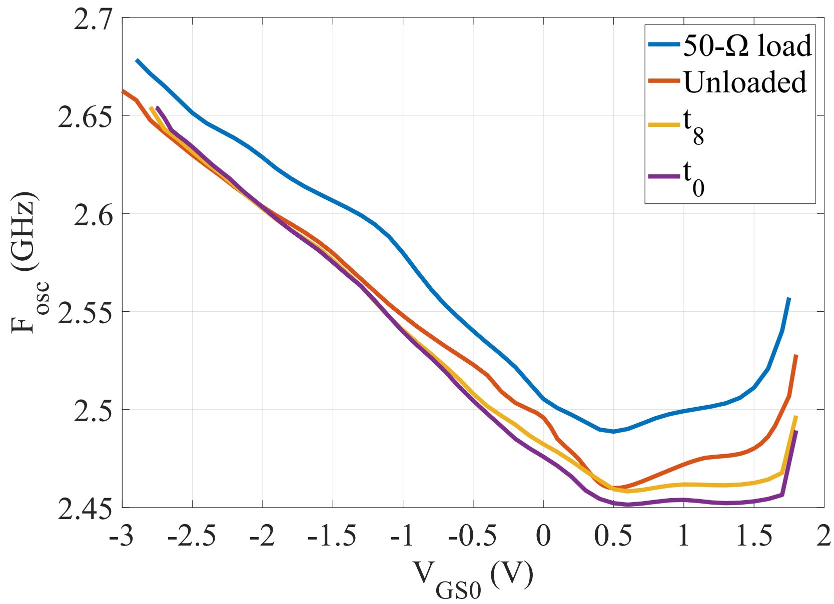

(b)

Figure 2.15: (a) Predicted bifurcation diagrams and (b) steady-state oscillation frequencies for a 50–Ω load and three different loading conditions: unloaded, t_8, and t_0. Simulations are based on the measurements shown in Fig. 2.14 [9] © 2025 IEEE.

These graphs show the HB-simulated bifurcation diagrams and the steady-state oscillation frequencies, with the unloaded antenna and the ideal 50–Ω load included as reference cases for comparison. In the simulations, the drain-source bias is fixed at $V_{DS0} = 2.5$ V, while the gate-source bias V_{GS0} is swept to investigate the system's nonlinear response. For $V_{GS0} = -0.1$ V, the computed RF power delivered through the antenna reached 16.3, 13.2, and 11.3 dBm for the unloaded, t_8, and t_0 cases, respectively. When an ideal 50–Ω load is assumed, the RF is overestimated compared to real cases, particularly in the lower V_{GS0} region, since the ideal case neglects the intrinsic losses and dispersive effects associated with varying moisture content. Indeed, as the moisture level increases, the electromagnetic losses within the wood and the dielectric dispersion of the antenna structure become more pronounced, leading to a significant reduction in the available RF power of the self-oscillating system. This phenomenon highlights the sensitivity of the oscillator's behavior to its load impedance characteristics. As expected, the oscillation frequency F_{OSC} shows a strong dependence on the antenna's complex input impedance, and therefore on the moisture conditions. For instance, with $V_{DS0} = 2.5$ V and $V_{GS0} = -0.1$ V, the predicted oscillation frequencies are 2.498 GHz, 2.48 GHz, and 2.47 GHz for the unloaded,t_8, and t_0 conditions, respectively, whereas the ideal 50–Ω load yields $F_{\mathrm{OSC}} = 2.52$ GHz. These results clearly demonstrate that including the measured dispersive load responses across the relevant harmonics leads to distinct oscillatory regimes and improved prediction accuracy.

In this case, a patch antenna is employed as a load element instead of a high Q-resonant structure. This is motivated by the fact that the quality factor of the patch is lower, resulting in a broader impedance bandwidth and, consequently, a more tolerant oscillation condition. For self-oscillating circuits, the feedback loop must satisfy both the phase and amplitude conditions over a frequency range determined by the active device and the load. Using an element with low Q-factor, such as a patch antenna, simplifies the fulfillment of these conditions, allowing the system to sustain oscillations even in the presence of significant variations in the load impedance or in the material characteristics. Further, the application of a radiating element as a load directly couples the oscillation to the EM field in the surrounding medium, enabling the generation and sensing of radiation without requiring an additional resonant element within the loop. This reduces the complexity of the self-oscillating antenna structure and makes it more robust for sensing applications involving lossy or dispersive materials.

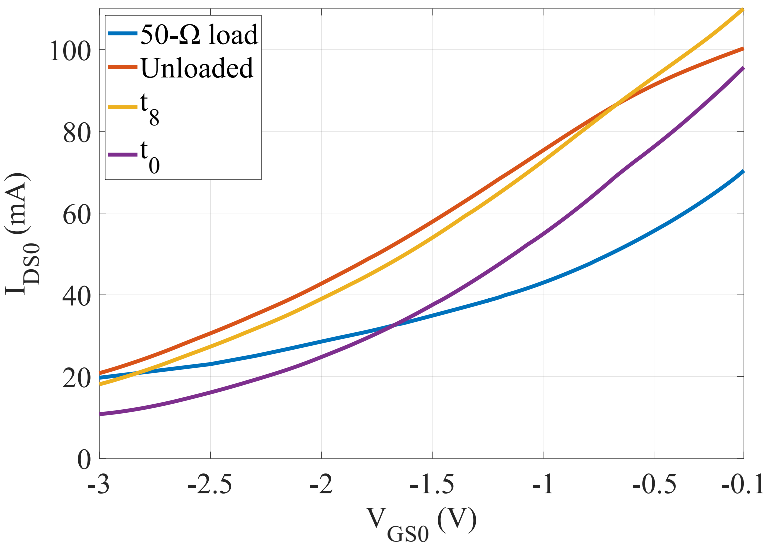

Figure 2.16: Simulated DC drain current, I_{DS0}, versus V_{GS0} at $V_{DS0} = 2.5$ V [9] © 2025 IEEE.

Additionally, the variation of the DC operating point of the active device with the antenna load is evaluated as a proof of concept. Fig.2.16 shows the simulated DC drain-source current, I_{DS0}, as a function of V_{GS0} at $V_{DS0} = 2.5$ V, for the selected cases of MC levels t_0 and t_8, along with the unloaded and 50–Ω ideal-load as reference.

In the self-oscillating, the quiescent point (Q-point) of the active device varies with the load impedance of the loaded patch antenna, which is influenced by the dielectric properties of the wood under different hydration conditions. The resulting steady-state oscillating regime therefore determines the circuit's electrical quantities, such as the RF output power, the oscillation frequency, and the DC operating point, from which the relevant information about the loading conditions can be obtained.

Nonlinear simulations for a wide range of V_{GS0} reveal that distinct I_{DS0} values, and therefore various DC power consumption, are associated with each moisture content condition. The variations in wood's moisture content directly regulate the Q-point of the active device, providing a measurable signature in the DC characteristics that can be utilized for continuous sensing. This correlation indicates that the oscillator's DC bias values reflect the antenna load, and in turn, the wood's moisture content, providing a low-cost, energy-efficient method for continuous sensing. It enables the extraction of environmental parameters, such as material moisture content, directly from the DC characteristics of the self-oscillating antenna circuit, without requiring additional RF measurement hardware.

2.5 Fabrication and Experimental Validation of the Loaded Self-Oscillating Antenna

The fabrication of the self-oscillating antenna system is carried out through a two-step process, wherein the patch antenna and the oscillator circuit are manufactured separately. Both components are produced using a precision laser-etching techniques,ensuring minimal fabrication tolerances. After individual fabrication, the two modules are carefully aligned and glued back-to-back, sharing a common ground plane. A rectangular aperture is etched in the shared ground plane, as illustrated in Fig.2.10, to enable electromagnetic coupling between the oscillator and the patch antenna.

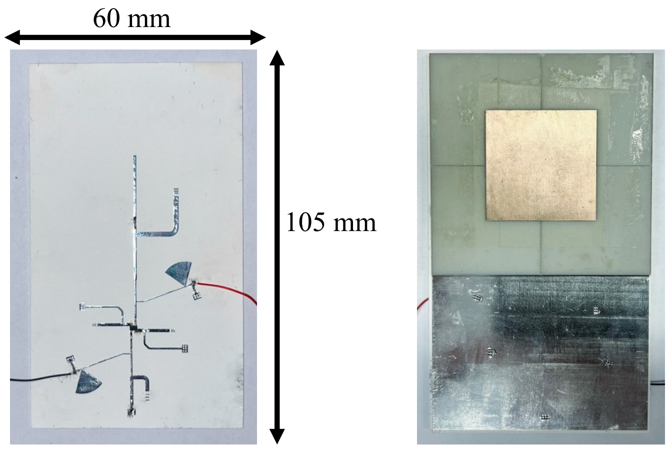

Figure 2.17: (Left) Top view and (right) bottom view of the fabricated device. The overall dimensions are $105 \times 60 \times 2.2$ mm^3 [9] © 2025 IEEE.

Photos of the assembled system are presented in Fig.2.17. It is particularly noteworthy that the fabrication strategy ensures compact dimensions and lightweight construction, which are essential for practical deployment, as they allow the sensor to be easily mounted on tree trunks of varying sizes without imposing mechanical stress.

The performance of the self-oscillating antenna is first evaluated in free-space conditions, with the antenna unloaded, to characterize its nominal oscillatory behavior. Subsequently, the system is tested in wood-loaded conditions, where the antenna interacts with samples exhibiting different moisture content levels. These measurements provide a comprehensive understanding of how the self-oscillating antenna's oscillatory behaviors are influenced by the electromagnetic properties of the attached material, enabling the correlation of the measured DC and RF responses with the wood's hydration state. The proposed fabrication methodology combines precision, compactness and adaptability, allowing the self-oscillating antenna system to operate as a portable, reliable, and versatile sensor for environmental monitoring applications.

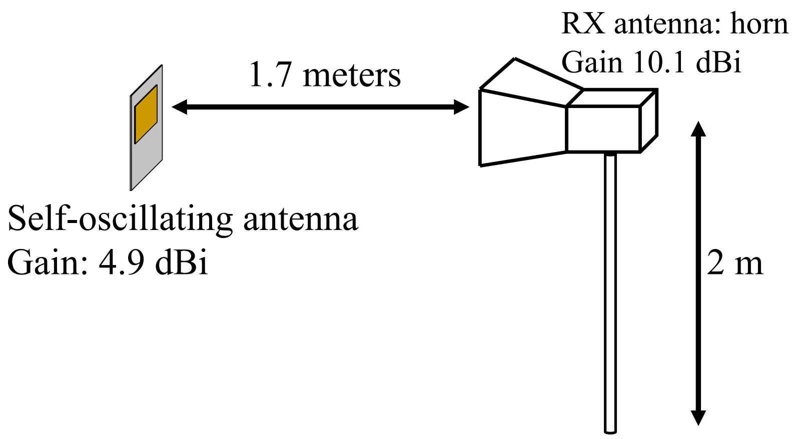

Figure 2.18: Rendering of the measurement setup for the unloaded self-oscillating antenna in free-space conditions [9] © 2025 IEEE.

2.5.1 Free-Space Characterization of the Self-Oscillating Antenna

The performance of the self-oscillating antenna are initially assessed in free-space conditions, with the antenna operating in transmission mode and unloaded, to validate the fabricated prototype. A horn antenna, with a gain of 10.1 dBi, is employed as the receiving element and positioned at a distance of 1.7 m from the transmitting antenna. Both antennas are placed at a height of 2 m above ground level to minimize ground effects and ensure unobstructed propagation. At this distance, the far-field criteria are satisfied in terms of wavelength and with respect to the receiving horn antenna's aperture. The received power and the oscillation frequency are measured using a spectrum analyzer connected to the receiving horn antenna.

Fig.2.18 illustrates the experimental free-space setup, while Fig.2.19 presents the

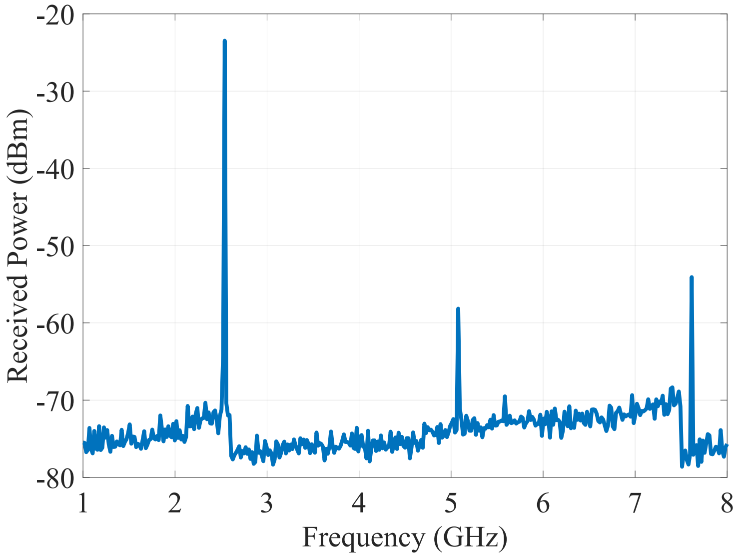

Figure 2.19: Measured power spectrum of the signal received from the self-oscillating antenna with the active device biased at $V_{DS0} = 2.5$ V and $V_{GS0} = -1.5$ V in free-space conditions [9] © 2025 IEEE.

measured received power spectrum, which includes the fundamental component and its first three harmonics. The reported measurements correspond to a representative bias point, $V_{DS0} = 2.5$ V and $V_{GS0} = -1.5$ V. Under these conditions, a received power of -23 dBm and an oscillation frequency of 2.52 GHz are recorded. The measured harmonic suppression levels are approximately 35 dBc for the second harmonic and 31 dBc for the third harmonic, demonstrating the oscillator's ability to maintain spectral purity under the specified biasing condition. Similar spectral purity is also observed for other polarization states.

The effective radiated power of the self-oscillating antenna in free-space condition is estimated indirectly. The estimation accounts for the free-space path loss, the gains of the transmitting and receiving antennas ($G_t = 4.9$ dBi, $G_r = 10.1$ dBi), and the losses introduced by coaxial cables and connectors ($L_c = 3$ dB). The free-space path loss ($FSPL$) is calculated using the standard Friis formula:

$$\mathrm{FSPL}\,[\mathrm{dB}] = 20\log_{10}(d) + 20\log_{10}(f) + 20\log_{10}\left(\frac{4\pi}{c}\right) \tag{2.9}$$

where d is the distance between the antennas in km and f is the frequency in MHz. For the present setup, this corresponds to approximately 45 dB at the measured frequency. The received power can then be estimated as:

$$P_r\,[\mathrm{dBm}] = P_t\,[\mathrm{dBm}] + G_t\,[\mathrm{dBi}] + G_r\,[\mathrm{dBi}] - \mathrm{FSPL}\,[\mathrm{dB}] - L_c\,[\mathrm{dB}] \tag{2.10}$$

This indirect valuation allows for an accurate estimation of the oscillator's radiated performance without the need for direct on-board RF probing, which could perturb the oscillatory behavior.

The tuning capabilities of the proposed self-oscillating antenna are measured by sweeping V_{GS0} over the range $[-3\text{ V}, 0\text{ V}]$, while maintaining $V_{DS0} = 2.5$ V. Both the oscillation frequency and the radiated RF power are measured and compared with the nonlinear simulations results, as shown in Fig. 2.20, demonstrating good agreement across the entire bias range and thereby validating the accuracy of the NL-EM co-simulation approach. At $V_{DS0} = 2.5$ V, and $V_{GS0} = -1.5$ V, the measured radiated power is 10 dBm, in close agreement with the 10.7 dBm predicted by HB simulations. The corresponding oscillation frequency is 2.52 GHz in measurement and 2.56 GHz in simulation, confirming the reliability of the proposed modeling approach.

Measurements are performed exclusively for $V_{GS0} < 0$ V to prevent potential degradation or damage to the pHEMT device, ensuring reliable long-term operation.

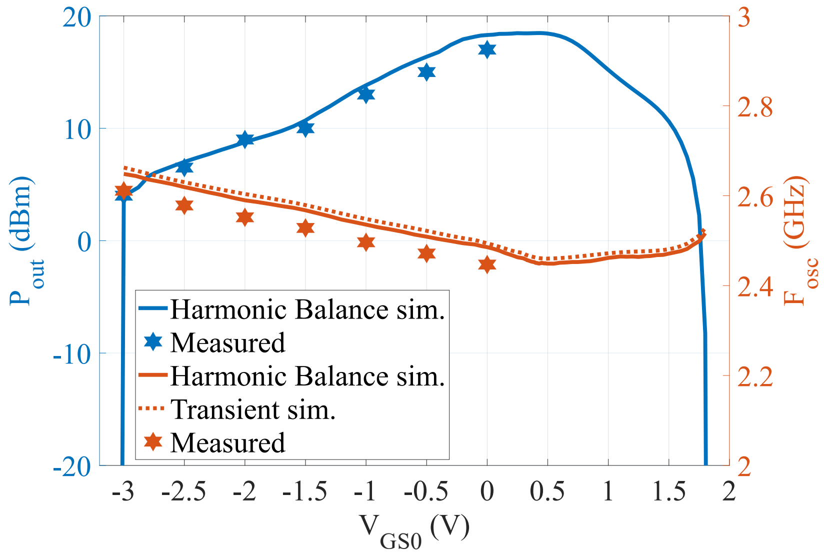

Figure 2.20: Comparison between predicted and measured bifurcation diagrams and oscillation frequency of the self-oscillating antenna in the unloaded configuration, for different V_{GS0} values at $V_{DS0} = 2.5$ V [9] © 2025 IEEE.

2.5.2 Measurements of the DC-States of the Self-Oscillating Antenna

The DC drain source current measurements for moisture content detection are carried out over a four-day experimental campaign. To guarantee uniform and repeatable humidity conditions, the measurements procedure followed the same controlled drying protocol described in 2.13 ensuring that each measurement corresponded to a well-defined moisture content state. A photo of the experimental setup is presented in Fig.2.21 where the self-oscillating antenna is placed in direct contact with the wood sample.

As a representative result, Fig.2.22 shows the measured I_{DS0} at $V_{DS0} = 2.5$ V for the nine distinct loading conditions, while varying V_{GS0}.

The plots exhibit clearly distinguishable curves corresponding to each MC level, demonstrating good agreement with the prediction of 2.16. These results confirm that the DC operating point of the self-oscillating antenna can reliably reflect the

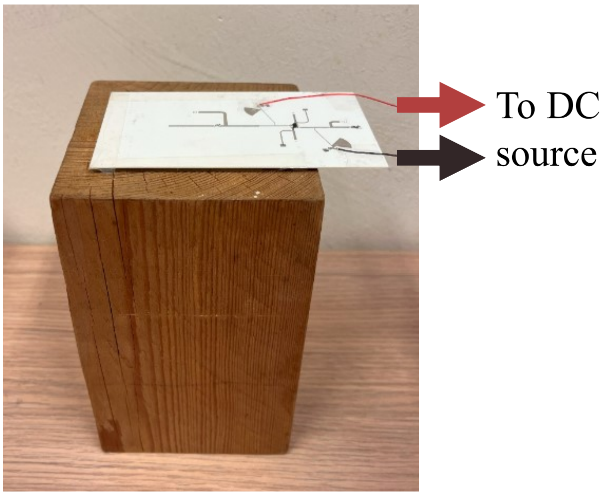

Figure 2.21: Measurement setup for MC detection: the system is in direct contact with the wood sample [9] © 2025 IEEE.

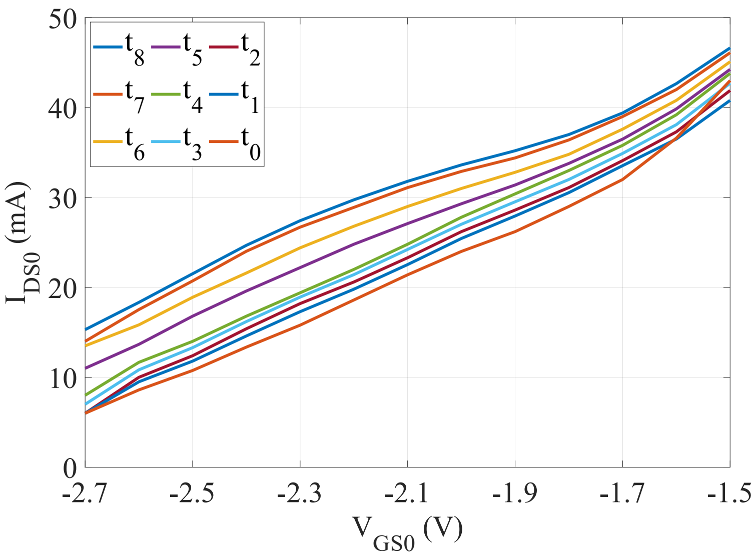

Figure 2.22: Measured I_{DS0} as a function of V_{GS0}, with $V_{DS0} = 2.5$ V, under the same moisture content conditions as in Fig 2.13 [9] © 2025 IEEE.

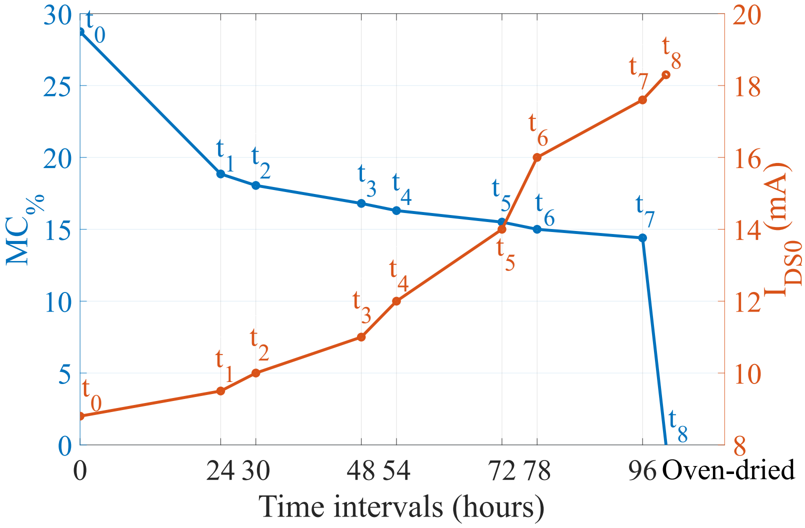

Figure 2.23: (Left) Measured moisture content (%) over the 4-day drying process. (Right) Measured DC drain-source current of the oscillator for $V_{GS0} = -2.6$ V and $V_{DS0} = 2.5$ V [9] © 2025 IEEE.

material's moisture content. In Fig.2.23, the measured DC drain-source current is superimposed on the measured $MC_{\%}$ data over the same time intervals (from t_0 to t_8), revealing a clear and predictable correlation between the wood's moisture content and the DC states of the self-oscillating antenna. These experimental observations fully corroborate the behavior predicted by the harmonic-balance simulations, confirming the feasibility of DC-based moisture sensing without requiring RF measurements.

By correlating the measured wood moisture content with the measured DC drain-source current under different bias conditions, it is possible to uniquely establish an analytical relationship between the actual moisture level and the nonlinear DC operating states of the self-oscillating antenna. A possible closed-form expression representing this behavior has been found to be a decreasing sigmoidal function:

$$f(x) = \frac{1}{1 + e^{x}} \tag{2.11}$$

which naturally captures the saturation behavior of the I_{DS0} with respect to $MC_{\%}$. To fit the measured data, this function is extended by introducing a translation along the I_{DS0} axis and a scaling factor to adjust the amplitude. The resulting analytical model is then expressed in closed form as:

$$I_{DS0}\big(MC_{\%}(t_i), V_{DS0}, V_{GS0}\big) = a(V_{DS0}) \cdot \frac{1}{1 + e^{b(V_{GS0})\cdot MC_{\%}(t_i)}} + c(V_{DS0}, V_{GS0}) \quad (2.12)$$

where $a(V_{DS0}) = 6 \cdot 10^4 \cdot V_{DS0}^2$, $b(V_{GS0}) = -0.28 \cdot V_{GS0}$, and $c(V_{DS0}, V_{GS0}) = V_{DS0}^3 - V_{GS0}^2$. The coefficients are determined by fitting the measured I_{DS0} across the full range of bias conditions. This procedure ensures that the model reproduces both the nonlinear shape of the I_{DS0} response and its dependence on the V_{DS0} and V_{GS0}. Fig. 2.24 illustrates the superposition between the measured and modeled values of $I_{DS0}\big(MC_{\%}(t_i), V_{DS0}, V_{GS0}\big)$ for three representative drain voltage ($V_{DS0} = 2.5\,\mathrm{V}, 3\,\mathrm{V}$ and $3.5\,\mathrm{V}$), while keeping $V_{GS0} = -2.6\,\mathrm{V}$ constant. Comparable agreement is achieved across a wider range of biasing conditions ($V_{DS0} = 2.5$–$3.5\,\mathrm{V}$ and $V_{GS0} = -2.7$ to $-1.5\,\mathrm{V}$), confirming the model's robustness and its ability to reproduce the nonlinear interaction between the active device and the moisture-dependent dispersive load. No data point is reported for the lowest moisture content condition (t_8), as the oven-dry state represents a limiting case corresponding to $MC_{\%} = 0$. Due to the limited number of measurements between approximately 14% moisture and the fully dried condition, the inclusion of this point would result in an excessively coarse interpolation over a wide interval, ultimately providing a misleading representation of the underlying trend. Therefore, the oven-dry point is omitted from Fig. 2.24 to unsure physical consistency and data readability.

From the measured DC states, a system sensitivity (S) can be defined as the incremental ratio between the variation of I_{DS0} and a 1% change in the measured

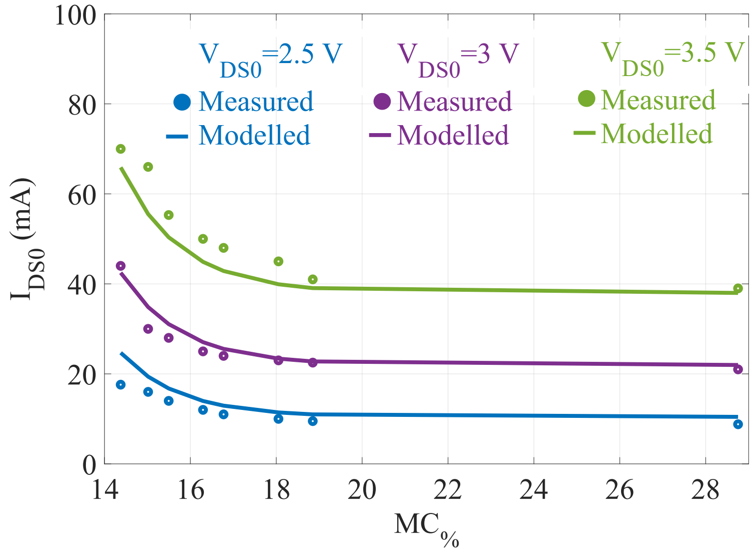

Figure 2.24: Comparison between measured and modeled $I_{DS0}(MC\%, V_{DS0}, V_{GS0})$ [9] © 2025 IEEE.

$MC_{\%}$, that is:

$$S = \frac{\Delta I_{DS0}}{\Delta MC_{\%}} = \frac{I_{DS0}(V_{DS0}, V_{GS0}, t_i) - I_{DS0}(V_{DS0}, V_{GS0}, t_j)}{MC_{\%}(t_i) - MC_{\%}(t_j)} \tag{2.13}$$

where t_i and t_j correspond to two time instants separated by a 1% variation in the moisture content, according to the available measurement resolution.

As shown in Fig.2.24, the sensor exhibits maximum sensitivity at low moisture levels, where even a minimal humidity changes induce significant variations in the DC drain current. This high responsivity is particularly relevant for critical hydration conditions, such as those encountered in partially dried or stressed wood tissues. Conversely, as the $MC_{\%}$ increases, the sensor's ability to discern small variations gradually decreases, although the correlation remains monotonic and easily recognizable. It is worth noting that the apparently flat interval of the curve, while exhibiting lower sensitivity, still show measurable and monotonic variations in I_{DS0}, which are sufficient to ensure reliable sensing. This behavior can be physically interpreted by considering that, at higher moisture levels, the antenna impedance departs considerably from a purely resistive behavior, introducing additional reactive components that attenuate the influence of the moisture variation on the oscillator's steady-state regime. In contrast, as the material approaches its dry state, the impedance tends to a more resistive behavior, thus reinforcing the nonlinear coupling between the active device and the dispersive load and resulting in higher I_{DS0} sensitivity.

Quantitatively, the lowest sensitivity of approximately $2\,\frac{\mu\mathrm{A}}{MC_{\%}}$, measured at $V_{DS0} = 2.5\,\mathrm{V}$, $V_{GS0} = -2.7\,\mathrm{V}$, is observed around $MC_{\%} \approx 28\%$, while the highest sensitivity reaching $9\,\frac{\mathrm{mA}}{MC_{\%}}$ is achieved at $MC_{\%} \approx 15\%$ under bias condition of $V_{DS0} = 3.5\,\mathrm{V}$ and $V_{GS0} = -2\,\mathrm{V}$.

2.6 Statistical Inference and Predictive Model

In the context of data analysis from self-oscillating antenna, the $MC_{\%}$ can be derived from the raw data of the DC steady states. However, the use of manual monitoring methods can be slow and prone to errors, especially when the number of measurements and the complexity of the data increase. In this scenario, the adoption of Machine Learning algorithms represents a strategic approach, as it allows the simultaneous handling of multiple variables and nonlinear relationships, providing more accurate, consistent, and scalable results [38].

For the present study, a regression-based predictive model is chosen, representing I_{DS0} data versus V_{GS0} values, using a limited set of experimental measurements. These measurements are organized into a data matrix $\mathbf{X}\,(N \times K)$, where N represents the number of acquired observations and K the number of independent V_{GS0} variables considered. The matrix $\mathbf{X}$ therefore constitutes the starting dataset for the predictive analysis. Moisture content information, which is the target of prediction, is collected in an output vector $\mathbf{Y}\,(N \times 1)$. To model the relationship between the independent (predictor) and dependent (response) variables, the Partial Least Squares Regression (PLSR) technique is adopted. This method allows the identification of latent variables LVs, that capture the shared variance between $\mathbf{X}$ and $\mathbf{Y}$, thus describing the underlying data structures. Thanks to this representation,the model remains robust even in presence of collinearity among predictor variables or when the number of variables exceed the number of observations, ensuring reliable predictions even with limited or highly correlated data [39].

Using a conventional regression, the dataset matrix $\mathbf{X}$ can be expressed as a linear combination of latent components according to

$$\mathbf{X} = \mathbf{T}\mathbf{P}^{\top} + \mathbf{E} \tag{2.14}$$

where $\mathbf{P}^{\top}(A \times K)$ defines an orthonormal subspace composed of A latent variables, $\mathbf{T}\,(N \times A)$ represents the corresponding projection scores of the observation onto these latent directions, and $\mathbf{E}$ denotes the residual matrix. When the directions of $\mathbf{P}^{\top}$ are optimized to minimize $\mathbf{E}$, an approximation of the dataset can be obtained as

$$\hat{\mathbf{X}} = \mathbf{T}\mathbf{P}^{\top} \tag{2.15}$$

where $\hat{\mathbf{X}}$ is a lower-dimensional representation of $\mathbf{X}$ onto a subspace defined by $A < K$ orthogonal components that capture the maximum variance. In this context, the $\mathbf{T}$ scores effectively summarize the information contained in $\mathbf{X}$ through the loadings $\mathbf{P}$, as in the classical Principal Component Analysis (PCA).

In PLSR, however, it is also necessary to consider the output dataset $\mathbf{Y}$, which can be decomposed in an analogous manner as

$$\mathbf{Y} = \mathbf{U}\mathbf{Q}^{\top} + \mathbf{G} \tag{2.16}$$

where $\mathbf{U}$ and $\mathbf{Q}$ are the score and loading matrices for $\mathbf{Y}$, respectively. Since the score matrix $\mathbf{T}$ derived from $\mathbf{X}$ is also predictive of $\mathbf{Y}$, the model can be rewritten as:

$$\mathbf{Y} = \mathbf{T}\mathbf{Q}^\top + \mathbf{F} \tag{2.17}$$

where $\mathbf{F}$ represents the residuals of $\mathbf{Y}$.

The optimal set of loadings is obtained by simultaneously maximizing: i) the variance captured in $\mathbf{X}$; ii) the variance captured in $\mathbf{Y}$; and iii) the correlation between $\mathbf{X}$ and $\mathbf{Y}$. This is achieved by maximizing the covariance between the score matrices $\mathbf{T}$ and $\mathbf{U}$.

In summary, the regression model can be described as:

$$\mathbf{X} = \mathbf{T}\mathbf{P}^T + \mathbf{E} \tag{2.18}$$

$$\mathbf{Y} = \mathbf{T}\mathbf{Q}^T + \mathbf{F} \tag{2.19}$$

where $\mathbf{E}$ and $\mathbf{F}$ are the residual matrices for $\mathbf{X}$ and $\mathbf{Y}$, respectively. Consequently, the output model can be expressed as:

$$\mathbf{Y} = \mathbf{T}\mathbf{Q}^T + \mathbf{F} = \mathbf{X}\mathbf{P}\mathbf{Q}^T + \mathbf{F} = \mathbf{X}\boldsymbol{\beta} + \beta_0 \tag{2.20}$$

In the context of this work, the PLSR model allows the prediction of the moisture content $MC_{\%}$ from the measured I_{DS0} values by estimating a set of regression coefficients $\beta\,(K \times 1)$. These coefficients enable the computation of the predicted output $\hat{\mathbf{Y}}$ for any newly acquired dataset $\hat{\mathbf{X}}$.

Fig.2.25 provide a visual representation of the entire PLSR workflow as applied in this work. Fig.2.23a illustrates the calibration dataset $\mathbf{X}$, which corresponds

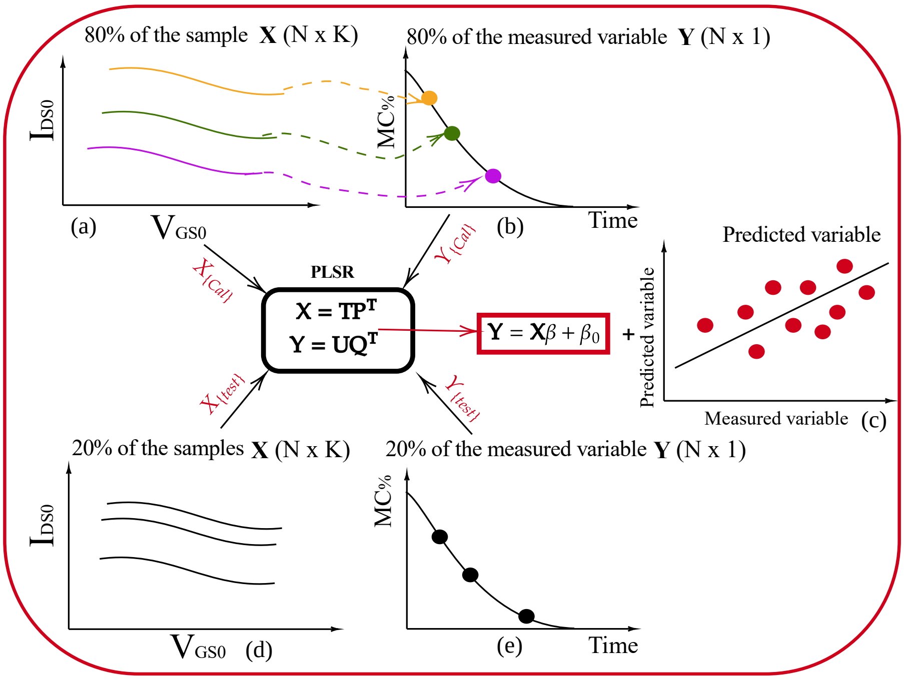

Figure 2.25: Map of the adopted PLSR model: (a) first calibration variable set **X**; (b) first output **Y**; (c) the predictive model behavior; (d) new input **X**; (e) new predictions [9] © 2025 IEEE.

to various moisture conditions, while Fig.2.23b shows the associated **Y** calibration dataset derived from independent reference measurements. The PLSR model estimates the coefficients $\beta\,(K \times 1)$ to predict $MC_{\%}$, and the relationship between predicted and actual values is presented in Fig.2.23c, where points closer to the bisector indicate higher predictive accuracy. Once calibrated, the model can process new inputs, as shown in Fig.2.23d, and generate new predictions, as shown in Fig.2.23e.

The PLSR algorithm employed here is based on the Nonlinear Iterative Partial Least Squares (NIPALS) method, a robust iterative procedure for determining eigenvalues and eigenvectors of matrices, which is particularly suitable for regression analysis when dealing with datasets containing missing values [40].

2.6.1 The Self-Oscillating Antenna Predictive Model and Results

The predictive model described in this work relies on the dataset obtained from the conducted measurement campaign. Specifically, the independent variables are the I_{DS0}, measured $N = 9$ times over the drying period (96 hours plus 1 hour in oven) for $K = 43$ values of V_{GS0}. To validate the procedure, several PLSR models are derived for differentV_{DS0} values. The data are organized into the matrix $\mathbf{X}\,(N \times K)$, while the dependent outputs (dataset moisture contents) are stored in $\mathbf{Y}$, which in this case is a 9-element vector.

Prior to model building, outliers are identified in $\mathbf{X}$, and test validations are performed to evaluate the model's predictive ability with unusual samples, avoiding the need for additional measurements. The performance of the PLSR models is assessed using the following metrics, calculated across all y_i and $\hat{y}_i$:

$$\mathrm{RMSE} = \sqrt{\frac{1}{N}\sum_{i=1}^{N}(y_i - \hat{y}_i)^2} \tag{2.21}$$

$$R^2 = 1 - \frac{\sum_{i=1}^{N}(y_i - \hat{y}_i)^2}{\sum_{i=1}^{N}(y_i - \bar{y}_i)^2} \tag{2.22}$$

$$\mathrm{Bias} = \frac{1}{N}\sum_{i=1}^{N}(y_i - \hat{y}_i) \tag{2.23}$$

Here, $RMSE$ (root mean square error) quantifies model accuracy relative to the ideal case (RMSE $= 0$). R^2 measures the correlation between predicted and observed values, with $R^2 = 1$ indicating perfect correlation. Bias represents the mean difference between predicted and actual values, indicating systematic errors (Bias $=$ 0 in ideal conditions). The performance of the models is summarized in Table 2.2. The best results are obtained at $\mathbf{V}_{DS0} = 2.5$ V, with $R^2 = 0.869$ (explaining 86.9%

Table 2.2: PLSR Performance Parameters for Different V_{DS0}

	$V_{DS0} = 2.5V$	$V_{DS0} = 3V$	$V_{DS0} = 3.5V$
LVs	3	3	3
R^2	0.869	0.511	0.695
RMSE	0.066	0.0197	0.0659
Bias	-0.0491	-0.018	-0.011

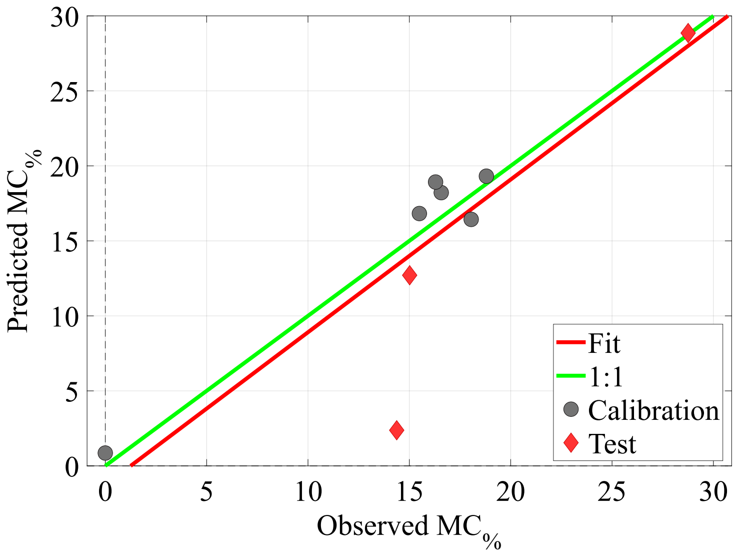

Figure 2.26: Observed versus predicted $MC_{\%}$ from the PLSR model [9] © 2025 IEEE.

of the variance) and RMSE = 0.066, indicating high predictive accuracy and minimal error. The Bias of -0.05 shows only a slight underestimation, confirming the model's reliability.

Fig.2.26 compares observed and predicted moisture contents for the first model ($\mathbf{V}_{DS0} = 2.5$ V). The green line represents the ideal 1:1 relationship, while the red line shows the model fit, closely following the ideal line. Calibration points (gray dots) cluster near the 1:1 line, and test points (red diamonds) remain close, confirming strong predictive accuracy and low Bias. Two of the three test points align closely with the ideal line, while the third exhibits a larger residual. This deviation is considered acceptable for two main reasons. First, the gravimetric reference $MC_{\%}$, computed according to Eq. 2.8, represents a bulk-average moisture content. During the drying process, moisture distribution within the specimen may be non-uniform, therefore, the bulk-average $MC_{\%}$ does not necessarily correspond to the region most strongly influencing the sensor-based predictors at a given time. Second, due to the necessarily limited dataset (N=9), the 80/20 calibration-validation split results in only three validation samples. Consequently, a single atypical point can have a noticeable visual impact without indicating a systematic generalization issue. Overall, the regression performance at $V_{DS0} = 2.5$ V remains strong ($R^2 = 0.869$ with low bias), and the fitted line closely follows the ideal trend. The limited number of test points reflects the controlled experimental conditions and the discrete nature of the drying measurements. Validation samples are randomly selected to ensure representative coverage of both low and high moisture content levels throughout the drying cycle. Due to its low computational demand, the predictive model can be stored on the sensor's µController, allowing calculation of moisture content $\hat{\mathbf{Y}}$ from a new measurement $\hat{\mathbf{X}}$, as in Eq.2.20. The performance metrics confirm the PLSR model's accuracy and efficiency in dimensionality reduction, making it suitable for resource-constrained applications such as IoT, highlighting its practicality and reliability.

2.7 Ongoing Project: Muscle Hydration Assessment Exploiting the Self-Oscillating Antenna

The operating principle of the self-oscillating antenna, paves the way for extending this technology from wood moisture monitoring to muscle hydration sensing.

Monitoring muscle hydration is important because fluid balance directly affects muscle function, metabolism, and recovery. Adequate hydration supports optimal blood flow, nutrient delivery, and waste removal within the muscle tissue [41–43]
Compared to traditional systems based on Bioelectrical Impedance Analysis (BIA), the self-oscillating antenna offers significant advantages. BIA systems measure the resistance and reactance of the human body to alternating currents, typically using multiple frequencies (from 1 kHz to 1 MHz), to estimate the intra- and extracellular water content and overall body composition. However, these systems rely on global and segmental electrical models of the body, require multiple electrodes, usually wight, positioned on the hands and feet, and measure the impedance across the entire anatomical segments such as limbs and trunk. Consequently, while providing an overall assessment of body composition, these methods are not sensitive to localized hydration variations, particularly in the trunk or specific muscle regions, where small impedance changes correspond to minimal variations in the estimated parameters [44]. In contrast, the self-oscillating antenna enables direct and localized monitoring of tissue hydration, enabling the detection of local variations in permittivity associated with the water content of the tissue, making this technology inherently sensitive and spatially localized, eliminating the need for complex RF measurements. Furthermore, the self-oscillating antenna system is portable, and low-cost, paving the way for wearable and real-time sensing systems for non-invasive assessment of muscle hydration. This approach therefore represents an evolution toward more precise monitoring, capable of detecting localized variations that traditional BIA-based methods cannot identify.

2.7.1 Experimental Validation of the Muscle Hydration Content

To verify the feasibility of employing the same antenna architecture used in wood moisture sensor for muscle hydration sensing, both EM simulations and experimental measurements are carried out. Seven biological phantoms are designed and fabricated, in collaboration with the University of Pavia, to replicate the dielectric properties of human tissues, including skin, fat, and muscle. While the skin and fat layers are kept constant to maintain realistic tissue properties, the muscle layer is represented by a mixture of water and oil, with the oil content varied from 10%, corresponding to the most hydrated condition, to 70%, corresponding to the most dehydrated condition, in increments of 10% to simulate a range of muscle hydration levels. Each phantom is characterized to determine its complex electric permittivity over the frequency range from 0.5 GHz to 40 GHz using a probe measurement technique.

The measured complex permittivity values, reported in Fig. 2.27, are used as input parameters in the EM simulations to accurately model the different tissue layers. The simulations predict the mean E-field norm according to the Eq.2.2, indicating that the E-field effectively penetrates the superficial layers and reaches the muscle region. Throughout the tissue volume of interest, the E-field preserves a significant intensity, confirming the patch antenna's capabilities to perform localized sensing and probe deeper muscle regions, thereby demonstrating its suitability for non-invasive muscle hydration monitoring.

As previously carried out for moisture content detection in wood sample (see Subsection 2.3.2), a dataset of S_{11} measurements is developed to investigate the relationship between muscle hydration and the patch antenna response. Specifically, S_{11} is measured on all seven phantoms, with each measurement repeated three times

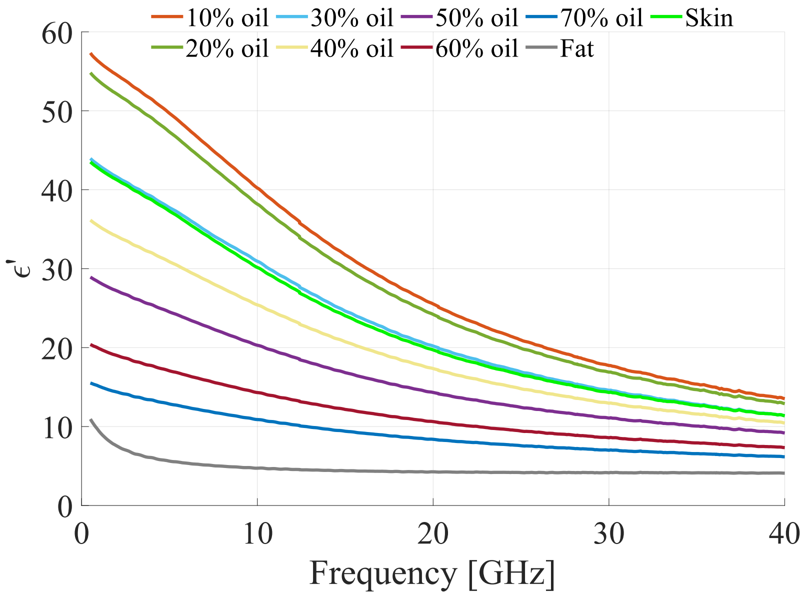

(a)

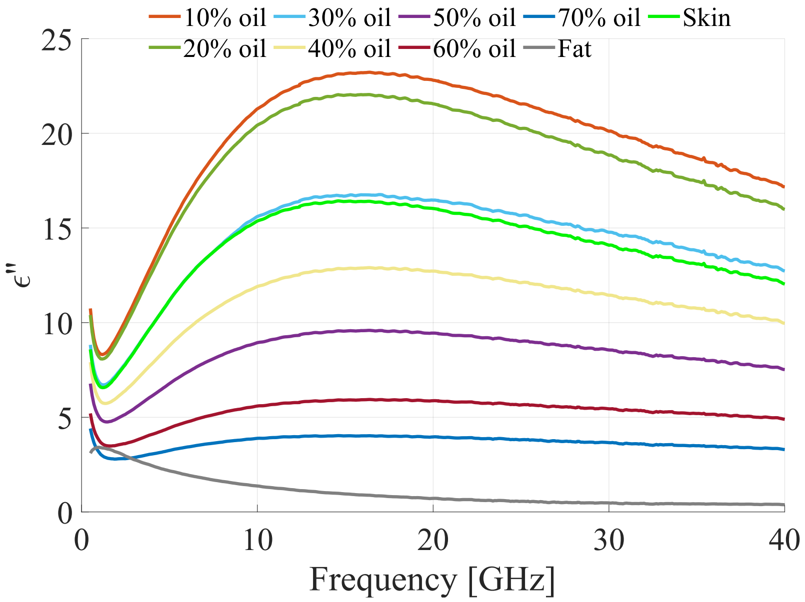

(b)

Figure 2.27: Measured complex relative permittivity of the phantoms with varying muscle hydration levels: (a) real part, (b) imaginary part.

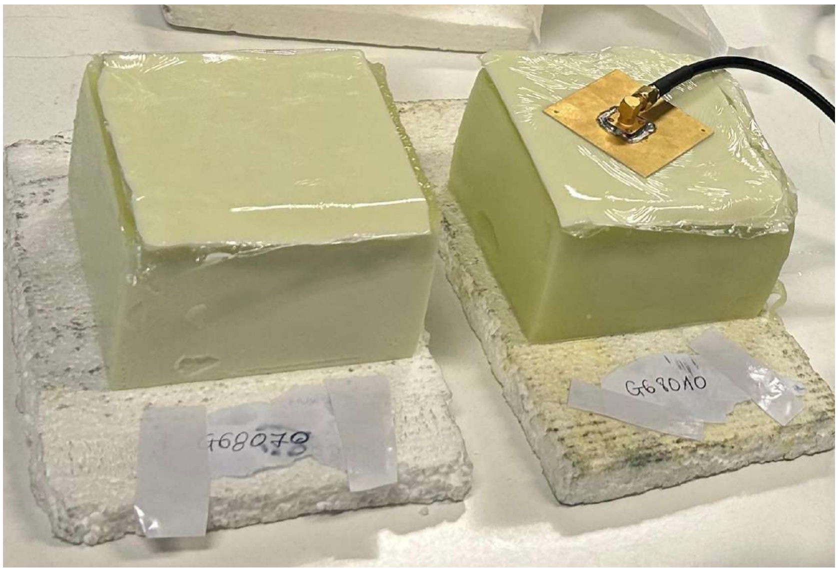

Figure 2.28: Measurement setup of the patch antenna in contact with two tissue-mimicking phantoms, showing the muscle layer with 10% oil (most hydrated) and 70% oil (most dehydrated), along with the skin and fat layers.

to ensure data consistency. The measurement setup, shown in Fig. 2.28, illustrates the patch antenna placed on the phantom, allowing clear visualization of the tissue layers and ensuring consistent contact during the testing.

The dataset, illustrated in Fig. 2.29, will subsequently be employed in NL-EM co-simulations of the self-oscillating antenna to predict variations in the steady-state regime and, consequently, in the sensing parameter I_{DS0} as a function of muscle hydration. To obtain reliable S_{11} measurements, its is essential to ensure measurement repeatability by maintaining identical electrical and geometrical properties of the skin and fat layers across all phantoms. The S_{11} response spectra demonstrate that the patch antenna is sensitive to variations in the oil-to-water ratio, which reflect different hydration levels. Nevertheless, efforts are ongoing to enhance the detectability of these variations by isolating the muscle contribution from the superficial skin and fat layers.

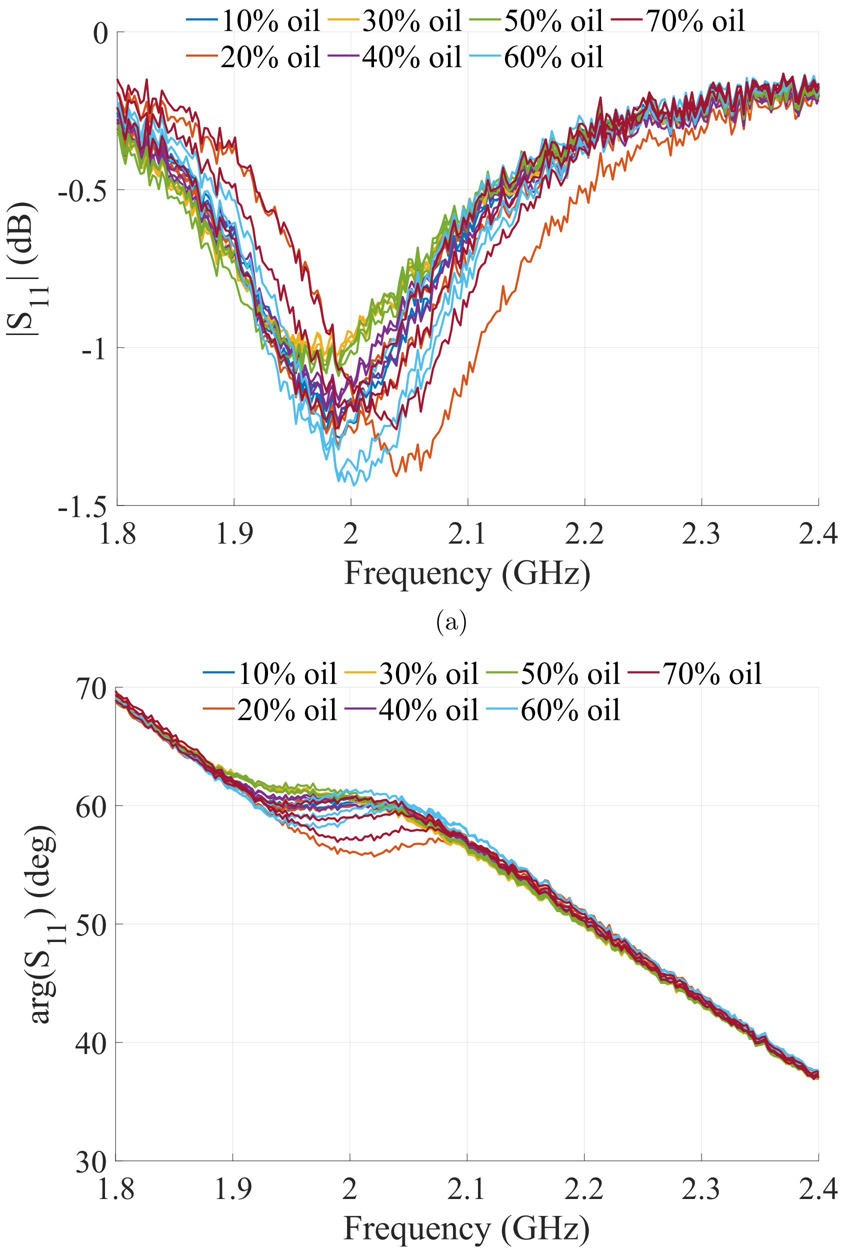

(a)

(b)

Figure 2.29: Measured S_{11} variations of the phantoms with different oil-to-water ratio levels: (a) magnitude, (b) phase.

2.8 Conclusions of the Chapter

In summary, this chapter presented the design, implementation, and experimental validation of a self-oscillating antenna operating in the 2.4 GHz band, for non-invasive moisture content sensing by monitoring the DC behavior of the nonlinear circuit. The design process involved a detailed investigation of the impact of different load conditions on the oscillatory steady-state regimes, using Harmonic balance simulations to ensure a robust and stable operation under realistic scenarios. Particular attention is devoted to the resonant structure design, where both electromagnetic simulations and measurements confirmed the superior field penetration and sensing performance of patch antenna compared to conventional resonant structures. The fabricated prototype is characterized under free-space and wood-loaded conditions, clearly revealing variations in its oscillation regimes and in the corresponding DC operating points. These experimental results validate the effectiveness, repeatability, and sensitivity of the proposed system, demonstrating that accurate $MC_{\%}$ estimation can be achieved solely through DC monitoring, without the need for complex RF measurement setups. Furthermore, to enhance the practical usability of the system, an offline predictive model based on PLSR is developed and trained using the experimental data. The integration of predictive model with the proposed hardware design allows for real-time autonomous operation, meeting the constraints of low-power and embedded IoT platforms. The self-oscillating antenna is lightweight, energy-efficient, and fully portable, making it a promising candidate for next-generation smart sensing systems, enabling continuous and distributed monitoring of moisture-related phenomena in environmental applications. Extending the demonstrated capabilities of the self-oscillating antenna, ongoing work is exploring its application for non-invasive monitoring of muscle hydration. Preliminary studies using biological phantoms have demonstrated the patch antenna's sensitivity to localized variations in muscle water content, highlighting its potential as precise alternative to BIA systems. The approach offers significant advantages, including spatially localized sensing, portability, low-cost implementation, making it suitable for wearable and real-time monitoring applications. These developments indicate that the self-oscillating antenna technologies can be extended beyond environmental sensing for biomedical and sport-related applications, providing a versatile platform for continuous, non-invasive, and high resolution assessment.

Chapter 3

Machine Learning-Enhanced Microwave Sensor for Skin Hydration Monitoring

This Chapter is based on the following publications:

S. Trovarello, O. Afif, A. Di Florio Di Renzo, D. Masotti, M. Tartagni, and A. Costanzo, "A Non-Invasive, Machine Learning Assisted Skin Hydration Microwave Sensor," in *2024 54th European Microwave Conference (EuMC)*, Paris, France, 2024, pp. 932-935.

O. Afif, A. Di Florio Di Renzo, S. Trovarello, A. Costanzo and M. Tartagni, "Boosting Microwave Hydration Sensors Performance with Machine Learning Techniques," in *2024 International Microwave and Antenna Symposium (IMAS),* Marrakech, Morocco, 2024, pp. 1-4.

3.1 Introduction of the Chapter

In recent years there has been a growing interest in the application of microwave-based sensing technologies within the biomedical domain. These sensors offer distinct advantages, including their non-invasive operation, the use of non-ionizing electromagnetic fields, and the ability to provide fast, repeatable, and low-cost measurements. Such characteristics make microwave sensors particularly attractive for continuous and real-time physiological monitoring, especially in the context where safety and user comfort are essential. The majority of microwave biomedical sensors reported in the literature rely on resonance-based mechanism, leveraging devices such as split-ring resonators, complementary split-ring resonators,and planar antenna structures. Meanwhile, machine learning has emerged as a pivotal technology in numerous research fields. This acceleration is largely driven by the increased availability of computational resources and the proliferation of digital data collected from a wide array of sensing systems. In the biomedical field, ML has been successfully applied to tasks including dielectric property estimation, temperature and thermal variation monitoring, tumor and breast cancer detection, and non-invasive glucose level estimation [45–48]. The synergy between microwave sensors and ML method thus represents a promising pathway toward intelligent, adaptive, and personalized health monitoring solutions.

Maintaining a proper level of hydration is essential for human physiology, as even mild deviations can significantly affect cognitive performance, thermo-regulation, and metabolic efficiency. Variations in epidermal water concentration are associated with numerous dermatological conditions, including edema, inflammation, burns, and early-stage skin cancer. Consequently, accurate and accessible skin hydration assessment has become an important diagnostic and preventive goal. Although several technologies exist for evaluating skin hydration, they often suffer from high implementation costs, large and cumbersome hardware, and limited portability, which restrict their usability in routine clinical screening or wearable applications. Additionally, many of these systems lack integrated ML-based, data-driven intelligence, which reduces their ability to adapt to individual variability or environmental fluctuation that influence the dielectric response of skin tissue. Recent studies [49] have highlighted the importance of robust data acquisition strategies and the need for compact, energy-efficient, and user-friendly hardware. These insights have guided the development of next-generation microwave sensors, emphasizing the miniaturization, on-board processing, and smart calibration mechanism.

In this context, the work presented in this Thesis introduces a resonator-based skin hydration sensor that emplys a low-cost CSRR topology operating in the 2.4 GHz ISM band. The proposed system combines a portable, non-invasive, and wearable microwave sensing probe with an embedded classification algorithm capable of predicting hydration levels from measured reflection coefficients. The algorithm is based on a small dataset and statistical analysis to predict the hydration status of the human body directly from skin-sensing measurements.

Through this combination of hardware innovation and data-driven algorithms, the presented approach demonstrates the potential for next-generation microwave sensors that are compact, intelligent, and easy to use, paving the way for continuous and non-invasive skin health monitoring.

3.2 Coaxial-fed CSRR Design and and Electromagnetic Characterization

Microwave sensors based on complementary split-ring resonators have attracted significant attention for superficial biological sensing applications due to their intrinsic ability to strongly confine the electromagnetic field in the near-field region. Unlike radiating structures such as patch antennas, CSRRs operate predominantly in purely reactive near-field region, enabling a localized interaction between electromagnetic field and the material under test. This characteristic makes CSRR-based sensors particularly suitable for applications requiring sensitivity to dielectric variations confined within the outermost region of biological tissues, such as non-invasive skin hydration monitoring. In addition, CSRRs can be fabricated using standard printed circuit board processes and easily integrated with standard RF connectors, resulting in compact, low-cost, and mechanically robust sensing devices, well suited for biomedical implementations [50].

From a theoretical perspective, the electromagnetic behavior of the CSRR can be effectively described using an equivalent parallel LC circuit. In this representation, the inductance L_{eq} is associated with the circulating currents flowing along the metallic rings surrounding the etched slots, while the capacitance C_{eq} arises from the narrow gaps of the resonator and from the capacitive coupling between adjacent rings. Under the assumption of a homogeneous surrounding medium, the resonance frequency of the CSRR can be expressed as:

$$f_0 = \frac{1}{2\pi\sqrt{L_{eq}C_{eq}}} \tag{3.1}$$

Although simplified, this equivalent circuit provides valuable physical insight and serves as a first-order design tool for predicting the resonant behavior of the structure. In particular, it highlights the direct relationship between geometry and operating frequency. The inductive contribution increases with the total effective length of the current paths, which depends on the ring radii, the number of rings, and the spacing between the inner and outer rings. Conversely, the capacitive contribution is mainly governed by the gap width and by the inter-ring separation, which control the intensity of the fringing electric fields. Narrower gaps and smaller inter-ring distances lead to increased capacitance and stronger electric-field confinement, whereas wider gaps reduce capacitance and shift the resonance toward higher frequencies.

In this implementation, the CSRR is directly excited by a coaxial SMA connector. Therefore, a more complete circuit representation must include the feeding structure. The coaxial feed can be modeled as a transmission line with characteristic impedance $Z_0 = 50\,\Omega$. For electrically short lengths at the operating frequency, this section can be approximated by an equivalent series inductance L_f, accounting for the parasitic effects of the conductor. Additional shunt capacitance associated with the dielectric regions between the hot wire and the nut of the SMA is represented by C_f. Moreover, the finite conductivity of the coaxial cable conductors, both the nut and the hot wire, introduces ohmic losses, which can be represented by a series resistance R_f in the equivalent circuit. This resistance accounts for the power dissipated as heat due to the current flowing through the metallic conductors. Furthermore, the dielectric material filling the coaxial structure exhibits a non-zero loss tangent, this effect can be modeled by a shunt conductance G_f placed in parallel with C_f, accounting for dielectric losses. Accordingly, the complete equivalent circuit of the coaxial-fed CSRR, shown in Fig. 3.1, consists of a series inductance L_f, a series resistance R_f, a shunt capacitance C_f, a shunt conductance G_f, and the intrinsic parallel resonant tank formed by L_{eq} and C_{eq}, which models the CSRR itself.

Eq. 3.1 assumes a homogeneous surrounding medium such as vacuum and therefore cannot directly predict the behavior of a CSRR operating in contact with biological tissue. When the resonator is loaded by skin, the effective permittivity of the surrounding medium increases significantly, modifying the electric field distribution, particularly in the gap region. From an equivalent circuit point of view, this effect can be modeled as an additional capacitance C_{load} in parallel with C_{eq},

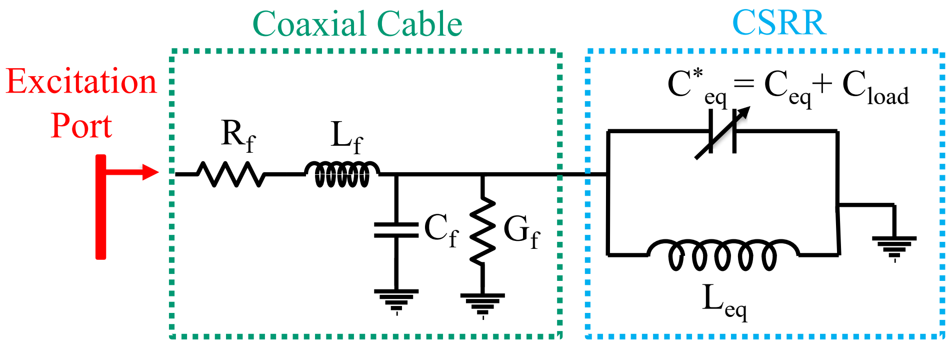

Figure 3.1: Lumped-element equivalent circuit of the coaxial-fed CSRR sensor, including the equivalent circuit model of the coaxial cable, and the parallel resonant tank formed by L_{eq} and the effective capacitance $C^*_{eq} = C_{eq} + C_{load}$.

yielding an effective capacitance:

$$C^*_{eq} = C_{eq} + C_{load} \tag{3.2}$$

The new resonance frequency becomes:

$$f^*_0 = \frac{1}{2\pi\sqrt{L_{eq}C^*_{eq}}} \tag{3.3}$$

An increase in the effective permittivity results in a higher equivalent capacitance and therefore a downward shift in resonance frequencies. This circuit interpretation provides a clear physical explanation for the frequency variations observed under different hydration conditions.

For design purpose, the CSRR dimensions are initially tuned and optimized in vacuum to obtain a preliminary resonance within the desired frequency range. Subsequently, the structure is further refined through full-wave electromagnetic simulations including a realistic multilayer skin model. This approach allow the dielectric loading effects introduced by biological tissue to be accurately captured and ensures that the final operating frequency lies within the desired range under actual sensing conditions.

The electromagnetic response of the sensor is modeled using a three-layer skin phantom representing the epidermis, dermis and hypodermis. The adopted layer thicknesses are 1 mm for the epidermis, 1 mm for the dermis, and 4 mm for the hypodermis, consistent with literature data for the palmar region [51]. The dielectric properties of skin at 2.4 GHz are taken from the literature [52, 53], with a relative permittivity of 38.1 and an electrical conductivity of 1.44 $\frac{\mathrm{S}}{\mathrm{m}}$. To account for variations in skin hydration, these dielectric parameters are modified by $\pm 5\%$. Dehydrated skin is modeled with a 5% lower relative permittivity and a 5% higher conductivity, while hydrated skin is modeled with 5% higher relative permittivity and 5% lower conductivity. These variations reflect the expected dielectric changes associated with water content and ion concentration in biological tissues. The dielectric properties of the hypodermis are kept unchanged, as adipose tissue exhibits limited sensitivity to hydration compared to the epidermal and dermal layers. Table 4.2 summarizes the dielectric properties and thicknesses adopted for the three-layer skin model under different hydration conditions.

Layer	**Thickness (mm)**	**Dehydrated**		**Normal**		**Hydrated**	
		ε_r	σ (S/m)	ε_r	σ (S/m)	ε_r	σ (S/m)
Epidermis	1 mm	36.2	1.51	38.1	1.44	40.0	1.37
Dermis	1 mm	36.2	1.51	38.1	1.44	40.0	1.37
Hypodermis	4 mm	10.8	0.26	10.8	0.26	10.8	0.26

Table 3.1: Thickness and dielectric properties of skin layers under different hydration states. The layer dimensions refer to the palmar region.

The sensor is fabricated on a low-cost FR4 substrate ($\varepsilon_r = 4.3$, $\tan\delta = 0.025$ at 2.4 GHz) with a thickness of 1.52 mm. This substrate is selected to ensure mechanical stability, ease of fabrication, and compatibility with standard PCB manufacturing process. To achieve seamless integration with the measurement instrumentation, the

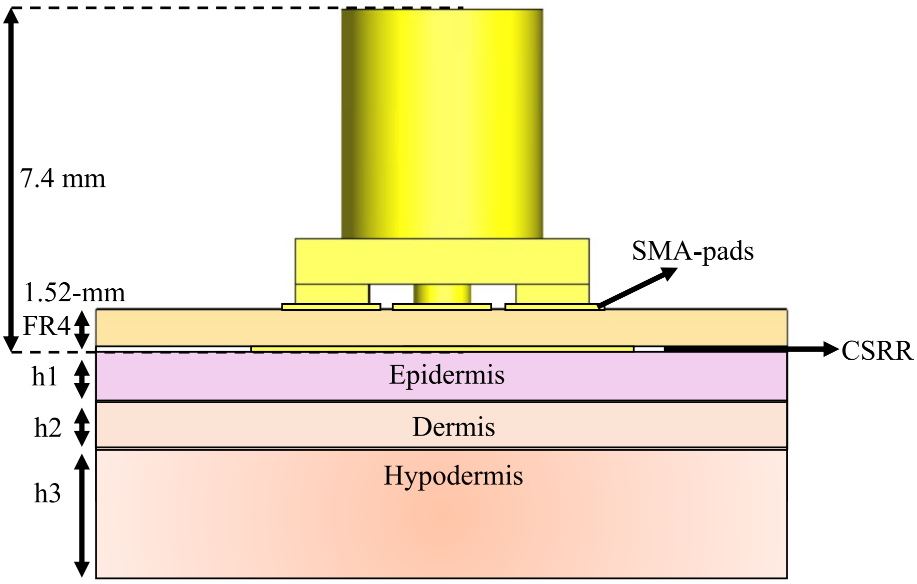

(a)

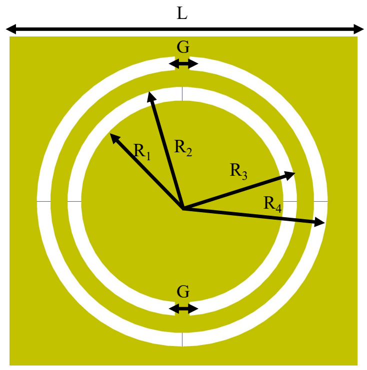

(b)

Figure 3.2: (a) Lateral and (b) bottom view of the proposed CSRR-based skin hydration sensor [13] © 2024 EuMA.

CSRR is directly mounted on a low-profile SMA connector. In this configuration, the ground plane is connected to the outer conductor of the SMA connector, while the central conductor is connected to the inner ring of the CSRR. Five via holes electrically connect the top and bottom layers of the PCB, minimizing parasitic inductance and improving electrical continuity. To prevent direct contact between

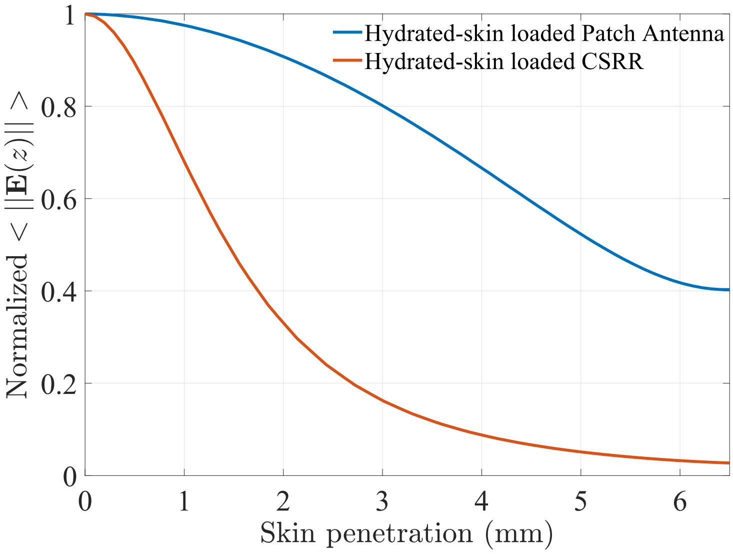

Figure 3.3: EM simulation of the mean value of the normalized E-field norm within a skin layer, excited by a patch antenna and a CSRR resonator at 2.4 GHz, considering the hydrated-skin condition [13] © 2024 EuMA.

the metallic resonator and the skin, an 8 μm PET layer is placed beneath the CSRR, enabling electrode-free operation while preserving the near-field coupling between the resonator and the skin surface. The lateral and bottom views of the fabricated CSRR and its geometrical parameters ($G = 0.2$ mm, $R_1 = 1.5$ mm, $R_2 = 1.7$ mm, $R_3 = 1.9$ mm, $R_4 = 2.1$ mm, $L = 8$ mm) are shown in Fig.3.2.

Full-wave electromagnetic simulations are performed in CST Studio Suite to evaluate both the electric field penetration and the resonance behavior of the skin-loaded CSRR. The mean electric field norm penetration depth is computed according to the method described in Chapter 2 (see Eq. 2.2). For comparison, a patch antenna operating at the same frequency is simulated under identical conditions. As shown in Fig.3.3, the CSRR confines the majority of the electric field near the skin surface, whereas the patch antenna allows deeper penetration beyond 6 mm, retaining approximately $\sim 40\%$ of its field strength. In contrast, the CSRR exhibits an $\sim 85\%$ reduction in electric-field intensity within the first 3 mm, confirming its oper-

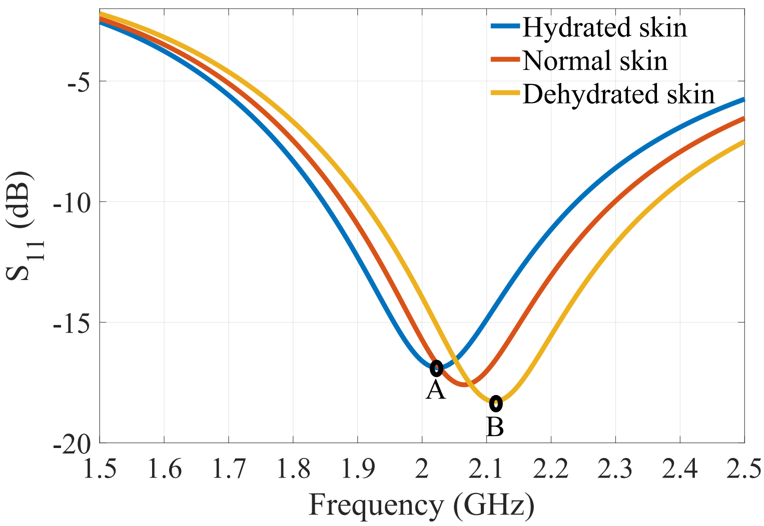

Figure 3.4: Reflection coefficient at the SMA port, with a 92 MHz shift observed across the simulated hydration range [13] © 2024 EuMA.

ation in the non-radiative near-field region and its suitability for superficial sensing.

To assess sensitivity to hydration-induced dielectric variations, the CSRR is simulated in contact with the skin model under different hydration conditions. The reflection coefficient at the SMA port is evaluated for each case, as shown in Fig.3.4. For normally hydrated skin, the return loss reaches 17.6 dB at 2.06 GHz, while for hydrated and dehydrated states, the resonance peaks shift to 2.024 GHz and 2.116 GHz, respectively. These results confirm the high sensitivity of the CSRR to small dielectric variations associated with skin water content, validating the proposed sensing approach for non-invasive, real-time skin hydration monitoring.

3.3 Experimental Validation and Integration with Machine Learning

This section presents the experimental validation of the CSRR-based skin hydration sensor and the integration of machine learning techniques for hydration assessment. A systematic measurement campaign is conducted across multiple anatomical sites, including the thenar eminence, proximal wrist crease, and cheek, capturing spectral responses under varying hydration conditions. Measurements are performed using a portable, low-cost setup combining the CSRR sensor with a compact nanoVNA controlled via a Raspberry Pi, enabling repeated and reproducible data acquisition in real-life conditions.

The collected spectral data are used to develop a multivariate classification model capable of distinguishing between hydrated and dehydrated skin states. Statistical analysis based on the Soft Independent Modeling of Class Analogy (SIMCA) method is applied to derive the model, which is validated through cross-validation and confusion matrix analysis. In addition, an extended measurement campaign is performed over multiple days and time slots to capture natural daily variations in skin hydration. For this larger and more complex dataset, a Principal Component Analysis (PCA)-based multivariate approach is adopted to perform unsupervised clustering, revealing natural grouping in the spectral data corresponding to multiple hydration levels. The use of compact, non-invasive sensing hardware together with data-driven algorithms demonstrates the feasibility of accurate and adaptive skin hydration monitoring.

3.3.1 Data Acquisition Procedures and SIMCA-Based Multivariate Modeling

The CSRR sensor is fabricated on an FR4 substrate, with the overall dimensions of $1.4 \times 1.4 \times 0.74\,\mathrm{cm}$, as illustrated in Fig. 3.5.

Spectral acquisitions are systematically performed twice per day across multiple anatomical sites: the thenar eminence, the proximal wrist crease, and the cheek. Measurements are obtained using a custom setup, which combined a low-

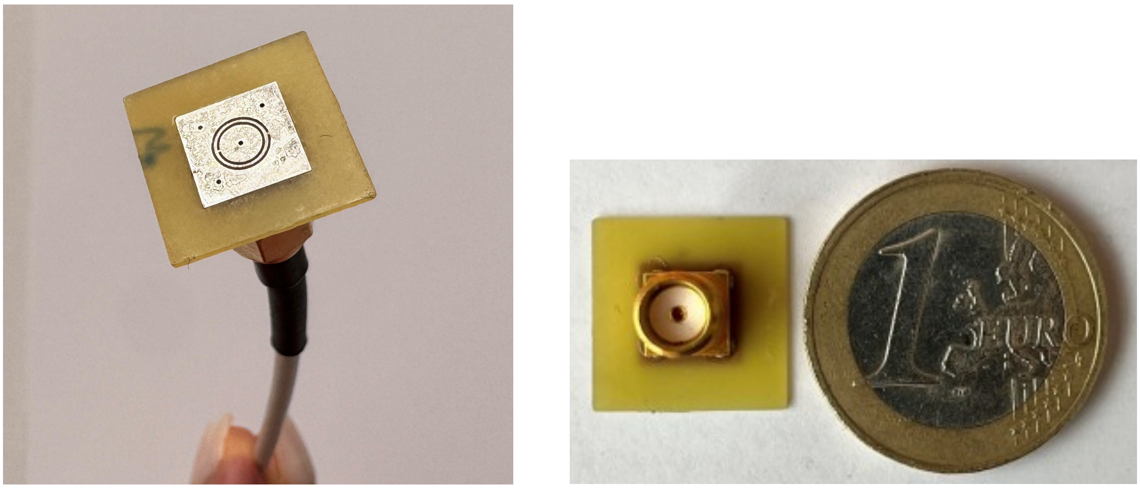

(a) (b)

Figure 3.5: (a) Top view and (b) bottom view of the fabricated CSRR-based skin hydration sensor [13] © 2024 EuMA.

cost nanoVNA controlled via a Raspberry Pi connected to the CSRR, enabling flexible and portable data collection at different body locations.

During the initial validation phase, the volunteer followed a 12-hour fasting protocol, abstaining from both food and liquids. The first measurement (t_1) is conducted 6 hours after the start of fasting, and the second (t_2) 14 hours after, resulting in approximately an 8-hour interval between acquisitions. The experimental procedure is repeated over two consecutive days to ensure consistency and reliability of the collected spectra. At each anatomical site, $2 \times N$ measurements (with $N > 3$) are acquired, each lasting roughly one minute, to ensure the spectral data is reliable.

A classification model is developed to distinguish between hydrated and dehydrated skin based on the amplitude of the measured reflection coefficient. For this purpose, a Soft Independent Modeling of Class Analogy (SIMCA) is employed, a multivariate statistical technique suitable for handling spectral datasets [54,55]. The process is divided into three steps: model creation, cross-validation, and validation, as depicted in Fig.3.6

For calibration, measurements collected from the selected anatomical region on

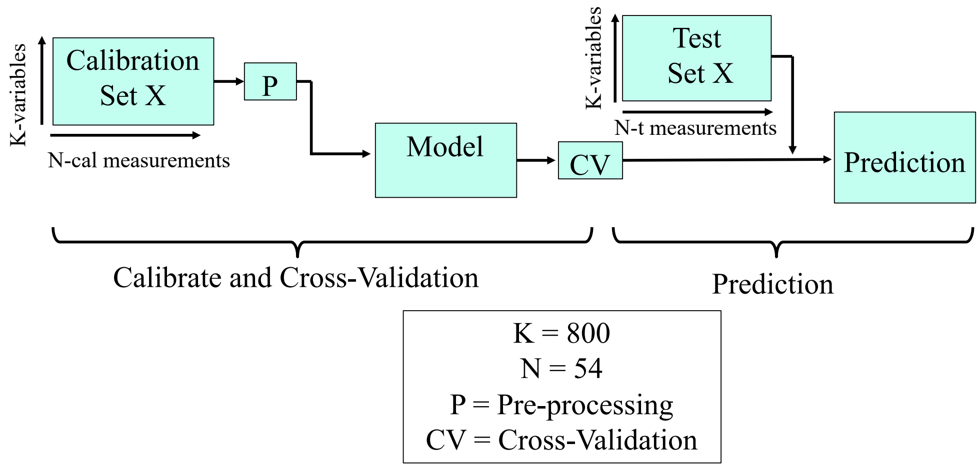

Figure 3.6: Illustration of the procedure followed by the SIMCA algorithm [13] © 2024 EuMA.

the volunteer's body are used as independent variables (X). These data are organized into a matrix of K = 800 variables (frequency points) x N = 54 measurements. The full dataset is then divided into training and test sets, with 80% of the sample used for model calibration and 20% reserved for testing. The split is performed randomly and uniformly across all classes. Once trained, the model classified the spectra into their respective hydration categories. The predicted class labels are compared to the actual classes, generating a confusion matrix, where rows represent the true class and columns the predicted class. This matrix, along with additional statistical metrics, provides a quantitative assessment of the robustness and accuracy of SIMCA-based classification model.

The experimental setup and the recorded spectra are shown in Fig. 3.7. The CSRR, operating in the RF range, is interfaced with a compact measurement unit that integrates a NanoVNA and a Raspberry Pi Zero W platform. This arrangement facilitates easy measurement and recording of the frequency response from 50 kHz up to 4.4 GHz. The measurements reveal a clear frequency shift across all three examined anatomical sites. Specifically, the resonant frequency of the CSRR

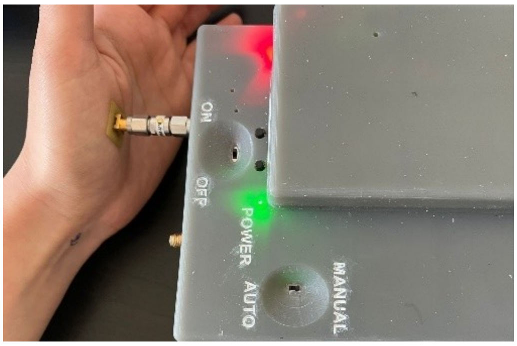

(a)

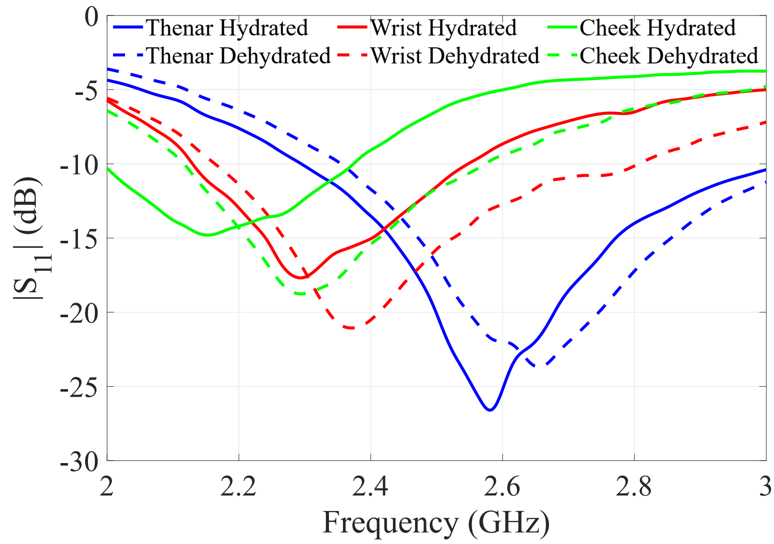

(b)

Figure 3.7: (a) Measurement setup and (b) the average of N spectra acquired at each position, for times t_1 and t_2 [13] © 2024 EuMA.

increases when comparing the t_1 and t_2 measurements. The cheek exhibited a shift of 143 MHz, the proximal wrist crease showed a shift of 90 MHz, and the thenar eminence had a shift of approximately 75 MHz. These trends provide a solid foundation for the development of statistical models aimed at classifying skin hydration levels. Moreover, the measured spectra are in good agreement with the simulated reflection coefficients reported in Fig. 3.4, confirming the sensor's predicted response. It is reasonable to interpret that the t_2 spectra correspond to a higher resonant frequency because the t_1 measurements are taken shortly after the onset of fasting, still reflecting the effects of recent food and fluid intake. Therefore, t_1 can be considered representative of hydrated skin, while t_2 corresponds to the dehydrated condition. This distinction is crucial for accurate model calibration and validation in subsequent multivariate analysis.

The acquired spectra are inevitably affected by noise originating from both instrumentation and human factor. To mitigate these effects, the underwent preprocessing before being fed into the SIMCA analysis. This preprocessing included outlier removal, autoscaling, and application of the Savitzky-Golay filter to the X dataset, ensuring each variable is centered and scaled to unit standard deviation. Additionally, the spectra are transformed using polynomial terms and cross-terms to account for non-linear trends in the data.

Model performance is evaluated using two standard metrics: the Root Mean Square Error of Cross-Validation (RMSECV) and the Root Mean Square Error of Calibration (RMSEC). The RMSEC quantifies the deviation between the model's predictions and the actual observed values in the calibration dataset, indicating how well the model fits the training data. it is calculated as:

$$\text{RMSEC} = \sqrt{\frac{1}{N}\sum_{i=1}^{N}(y_i - \hat{y}_i)^2} \tag{3.4}$$

where y_i represents the measured value, $\hat{y}_i$ is the predicted value form the model, and N is the total number of calibration samples. The RMSECV, on the other hand, evaluates the model's predictive capability on unseen data during cross-validation.In this procedure, each sample is temporarily excluded from the training set, the model is rebuilt, and the prediction error is computed for the excluded sample. This process is repeated for all samples, and the RMSECV is defined as:

$$\text{RMSECV} = \sqrt{\frac{1}{N}\sum_{i=1}^{N}(y_i - \hat{y}_{i,\text{cv}})^2} \tag{3.5}$$

where $\hat{y}_{i,\text{cv}}$ is the predicted value for the i-th sample when it is excluded form model training.

For the t_1 condition, the RMSEC and RMSECV are 0.2397 and 0.3908, respectively, while for t_2, they are 0.2511 and 0.4359. The slightly higher error observed at t_2 suggest that the model experiences increased prediction uncertainty under the dehydration condition. These metrics, together with the subsequent confusion matrix analysis, provide a comprehensive view of the model's reliability and its ability to generalize across different hydration states.

The confusion matrix, reported in Table 3.2, further evaluates the performance of the SIMCA classification model by comparing the predicted and the actual hydration states. Each row corresponds to the true class of the measured data, while each column represent the class predicted by the model. Correct classification appear along the diagonal, indicating agreement between measured and predicted hydration states, whereas off-diagonal entries highlight misclassified instances. this representation provides a direct and intuitive understanding of the model's accuracy and error distribution across classes.

	Predicted Hydrated in t_1	**Predicted Hydrated in t_2**
Actual Hydration in t_1	27	0
Actual Hydration in t_2	3	24
Unsigned Class	0	0

Table 3.2: Confusion matrix of the SIMCA classification model.

From the confusion matrix, two additional statistical parameters are derived and are

Class	Err	F1
Hydration in t_1	0.26	0.80
Hydration in t_2	0.26	0.75

Table 3.3: Statistical Parameters Calculated from the Confusion Matrix

summarized in Table 3.3: the misclassification error (Err) and the F1 score. The misclassification error quantifies the proportion of incorrectly predicted samples and is calculated as:

$$\text{Err} = \frac{TP + TN + FP + FN}{FP + FN} \tag{3.6}$$

where TP, TN, FP, and FN denote true positives, true negatives, false positives, and false negatives, respectively. A lower Err value indicates a higher overall accuracy of the classification model. The F1 core, instead, combines precision and recall into a single metric that balances false positives and false negatives, particularly useful when dealing with unbalanced dataset. It is defined as:

$$1 = 2 \times \frac{\text{Precision} \times \text{Recall}}{\text{Precision} + \text{Recall}} \tag{3.7}$$

where Precision $= \frac{TP}{TP+FP}$, and Recall $= \frac{TP}{TP+FN}$. The F1 score ranges from 0 to 1, with values closer to 1 denoting high accuracy and a good trade-off between sensitivity and precision. In this study, the confusion matrix (Table 3.2) shows that the vast majority of samples are correctly classified, and the associated statistical metrics (Table 3.3) confirm low Err values and high F1 scores for both t_1 and t_2 conditions. These results validate the robustness of the SIMCA model, demonstrating that it can effectively discriminate between hydrated and dehydrated skin states even with a limited dataset size.

3.3.2 PCA-Based Multiclass Analysis for Extended Hydration Monitoring

Although the SIMCA-based classification model successfully validated the feasibility of using microwave resonators for non-invasive skin hydration monitoring, its performance is limited by the relatively small dataset and the binary nature of the classification problem. This study, focused on two hydration states (t_1 and t_2), served as a proof of concept, demonstrating the sensor's capability to distinguish between hydrated and dehydrated conditions under controlled fasting protocol. However, to achieve a more comprehensive characterization of hydration dynamics and to assess the robustness of the sensor under more realistic physiological conditions, an extended experimental campaign is performed. The measurement protocol is expanded, and measurements are performed over six consecutive days and at four distinct time intervals per day, capturing natural daily variations in skin hydration. This allowed the collection of a larger dataset and the move from a binary to a multiclass problem. In this case, a Principal Component Analysis (PCA) is adopted instead of SIMCA to perform an unsupervised multivariate analysis. Unlike SIMCA, where PCA is used internally to model known classes, in this case PCA is employed to reveal and quantify the natural clustering of spectral data without predefined class labels. The objective is to investigate whether the sensor response could differentiate multiple hydration levels throughout the day, beyond the simple hydrated and dehydrated classes. The PCA is used to reduce the size of the spectral dataset while keeping most of the variance. The resulting principal component clearly revealed distinct clusters corresponding to different measurement time slots, confirming that the sensor is sensitive to gradual variations in skin permittivity and conductivity associated with hydration changes.

The extended measurement campaign is conducted on the same volunteer to

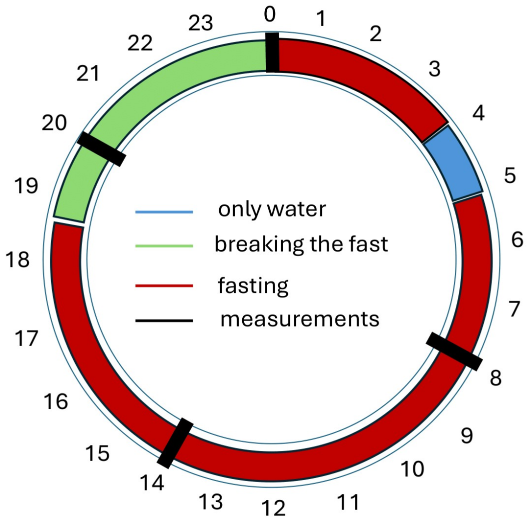

Figure 3.8: Schedule of the measurement campaigns.

ensure consistency with the previous study. The experimental protocol is set up to monitor hydration dynamics over six consecutive days, with four scheduled measurement sessions per day corresponding to specific time slots (7 am, 2 pm, 8 pm, and 12 pm). This schedule, summarized in Fig.3.8, allowed the observation of daily changes in skin hydration under real-life conditions, including periods of fasting and after meals. Spectral measurements are systematically acquired using the same CSRR-based sensor operating in the 2–3 GHz range. Each acquisition consisted of 128 spectra. The measured reflection coefficients amplitude, illustrated in Fig.3.9, exhibited noticeable shifts in resonance frequency across different time slots. In particular, frequency shift up to 250 MHz are observed between aftrnoon and evening measurements, while smaller but consistent variation ($\sim$ 90 MHz) occurred between morning and night acquisitions. These results confirm the high sensitivity of the sensor to changes in dielectric properties of the skin, which are directly correlated with hydration levels. To analyze these spectral variations, a PCA is applied to the complete dataset. The spectral data matrix, composed of 128 spectra $\times$ 400 frequency points, is mean-centered and scaled before analysis. PCA is used to re-

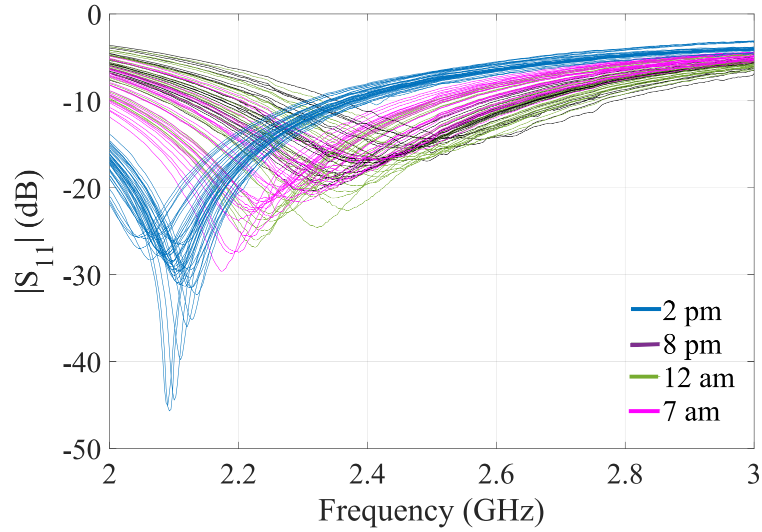

Figure 3.9: Spectra measured across time slots [14] © 2024 IEEE.

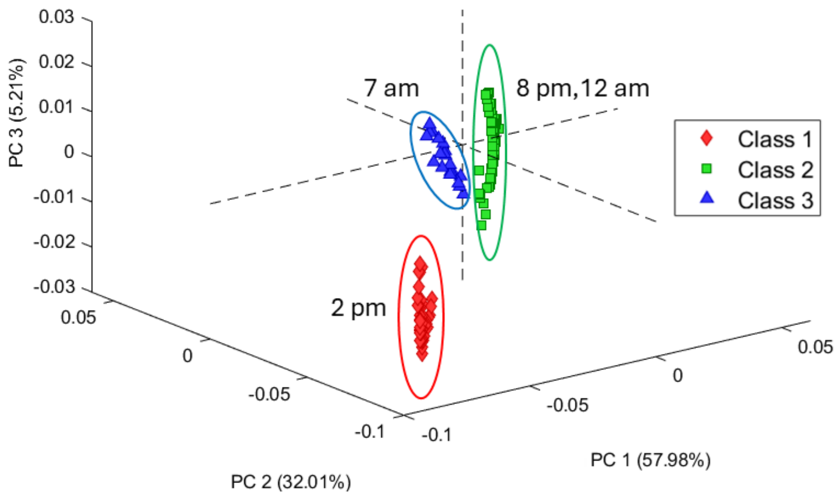

Figure 3.10: First three principal components derived from PCA [14] © 2024 IEEE.

duce the dimensionality of the data and to identify the principal sources of variance while retaining most of the information contained in the original spectra. Principal Components (PCs) are new variables derived form the original data that capture the largest sources of variations. The first three principal components (PC_1, PC_2, and PC_3) accounted for more than 95% of the total variance, highlighting the dominant features associated with hydration-related spectra changes. The three-dimensional PCS score plot, as shown in Fig. 3.10, shows a clear clustering of data points corresponding to different measurement times. The first principal component (PC_1), explaining 57.98% of the total variance, primarily captures the frequency shift associated with gradual dehydration throughout the day. The second and third principal components, PC_2, and PC_3, explain 32.01% and 5.21% of variance, respectively, and describe secondarily variations related, for example, to skin temperature and environmental factors.

	Observed For 2 pm	**Observed For 7 am**	**Observed For 8 pm and 12 am**
Predicted For 2 pm	37	0	0
Predicted For 7 am	0	20	0
Predicted For 8 pm and 12 am	0	0	55
Unsigned	5	0	3

Table 3.4: Confusion Matrix PCA-based Classification.

This separation demonstrates that the spectral data naturally group into distinct clusters corresponding to different hydration levels, confirming the sensor's ability to discriminate intermediate conditions without predefined class labels.

To further evaluate classification performance, the clusters identified in the PCA space are subsequently assigned to three hydration classes corresponding to the main time interval: class 1 (2 pm), class 2 (8 pm-midnight), and class 3 (7 am). Based on this labeling a confusion matrix, shown in Table 3.4, is generated to quantify the separation accuracy among the three groups. The matrix indicates high consistency between predicted and actual time intervals, with minimal overlap between adjacent classes, confirming the robustness of the PCA-based model.

3.4 Conclusions of the Chapter

This chapter presented a thorough analysis on the development and experimental validation of a non-invasive, low-cost microwave sensor for skin hydration monitoring based on a CSRR resonator. The sensor is designed to operate at 2.4 GHz and fabricated on an FR4 substrate, demonstrating compactness, mechanical stability, and the ability to operate in electrode-free conditions. The sensor's performance is evaluated through both electromagnetic simulations and experimental measurements, confirming the sensor's high sensitivity to hydration changes. The collected spectral data are initially used to develop a multivariate classification model employing SIMCA algorithm, capable of distinguishing between hydrated and dehydrated states in different anatomical regions. The low misclassification error and high F1 scores indicate that the SIMCA-based model, even when trained on relatively small datasets, is effective in accurately classifying hydration levels, validating both the sensor and statistical approach. To extend these results to a more realistic and comprehensive assessment of skin hydration, a multi-day measurement campaign is conducted, acquiring spectral data at four different time slots per day over six consecutive days. This extended dataset allowed the investigation of natural daily variations in hydration and the transition from a binary to a multiclass classification problem. For this purpose, a PCA-based unsupervised multivariate analysis is performed. Unlike SIMCA, PCA revealed the natural clustering of spectral data without predefined class labels, highlighting the sensor's ability to detect gradual and intermediate variations in skin hydration. The first three principal components captured over 95% of the total variance, and the PCA score plots clearly separated the spectra corresponding to different time intervals, demonstrating the feasibility of multi-level hydration monitoring.

The results confirm that the integration of compact, non-invasive sensing hardware with data-driven algorithms, both supervised and unsupervised, enables accurate, adaptive, and scalable skin hydration assessment. This approach demonstrates significant potential for the development of autonomous, non-invasive devices capable of real-time skin hydration monitoring. Furthermore, the method can be adapted to assess other hydration-related signals, thereby extending the sensor's applicability across a wide range of physiological and practical contexts.

Chapter 4

Compact Ku-Band Sensor for Atopic Dermatitis Detection

This Chapter is based on the following publications:

A. Di Florio Di Renzo, S. Trovarello, D. Masotti, M. Tartagni, and A. Costanzo, "Atopic Dermatitis Detection with a Compact Ku-Band CSRR-Based Sensor," in *2025 IEEE International Conference on RFID Technology and Applications (RFID-TA)*, Valence, France, 2025, pp. 1-4.

4.1 Introduction of the Chapter

Atopic Dermatitis is characterized by significant dysfunction of the *stratum corneum*, a thin layer which is only 15 μm thick, that acts as the main barrier against TEWL. In patient with AD, the SC undergoes microstructural and compositional changes that compromise its integrity, resulting in dehydration, pruritus, inflammation, and increased susceptibility to infections, as schematically illustrated in Fig. 4.1.

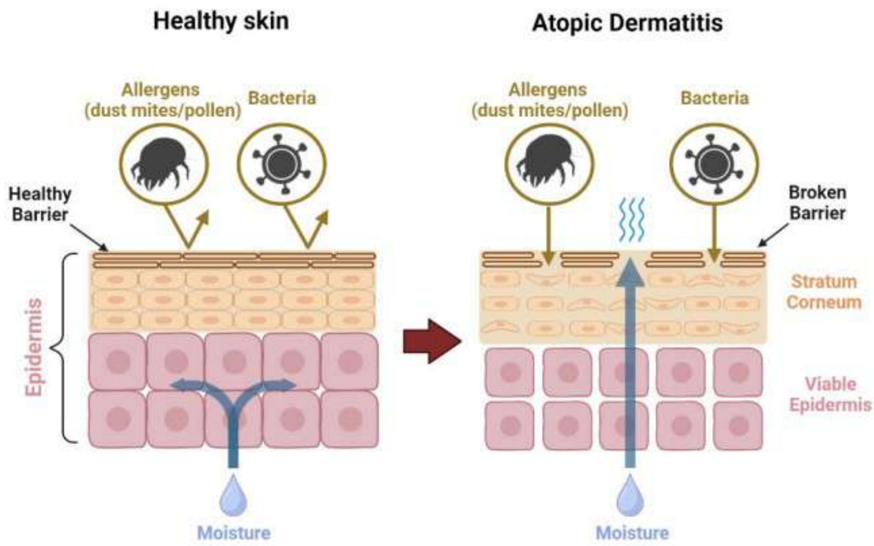

Figure 4.1: Cellular structure in healthy skin and AD-affected skin. Cracks in the stratum corneum alter skin electrical properties [60] © 2024 IEEE.

Traditional approaches to AD sensing typically model the skin as a single homogeneous layer, neglecting its true multilayered structure composed of *stratum corneum*, epidermis, and dermis. Since AD affects the SC, this simplification significantly reduces the sensitivity to relevant biomarkers. More advanced multilayer models have been proposed, but they mostly rely on hydration-based measurements. These methods lack specificity for AD, as dehydration can result from various physiological conditions. [56–60] A more selective approach is therefore required to detect structural changes uniquely associated with AD.

In the work presented in this Thesis, AD is not treated as a manifestation of dehydration, but rather as a condition characterized by the formation of microscopic fissures within the SC. The size,density, and severity of these fissures depend on the disease stage and serve as direct structural markers of AD. Targeting these features enables a more specific and reliable diagnostic assessment than hydration-based techniques. Detecting such microscopic fissures, however, require sensor with both high spatial resolution and shallow E-field penetration depth to selectively probe the SC without interference from deeper vascularized tissues. To address these requirements, a CSRR-based sensor operating in the Ku-band is employed. The high operating frequency of the sensor confines the electric field primarily to the SC and upper EP layer, minimizing interaction with the vascularized DR and thereby enhancing sensitivity to superficial structural changes. Microscopic fissures locally alter the permittivity and conductivity of the SC, leading to detectable shifts in sensor's resonance response. This approach enables a non-invasive, highly sensitive detection of AD-specific alterations that conventional hydration-based sensors cannot capture. Moreover, to ensure accurate characterization and prediction of the sensor, a multilayer electromagnetic model of human skin is implemented. This model accounts for the distinct electrical properties of each skin layer and simulates the sensor's response to varying degrees of SC fissures, offering a comprehensive tool to explore the interactions between skin structure and sensor response, providing insight into how structural changes affect sensor measurements.

4.2 Microstrip-Coupled CSRR Sensor Design for Dermatitis Detection

The proposed solution for detecting different stages of AD relies on a near-field resonant structure operating in the Ku-band. As discussed in the previous section, AD primarily affects the outermost skin layer, the *stratum corneum*. Since the dermis and hypodermis are vascularized tissues, sensing beyond the non-vascularized SC can introduce noise and lead to inaccurate detection. Therefore, the proposed dermatitis sensors is specifically designed to selectively probe only the SC, minimizing interference from deeper biological tissues.

The sensing device employs a CSRR etched in a defected ground plane configuration and excited through an open-ended microstrip line. Its operating principle is based on the interaction between the resonator's near-field fringing field and the SC, where structural disruptions caused by AD modify the local dielectric properties of the skin surface and consequently alter the resonant response of the structure.

From an electromagnetic point of view, a CSRR etched in the ground plane operates as an electrically small resonator. Unlike the coaxial-fed configuration presented in the previous chapter, in this case the excitation is provided by a microstrip transmission line located on the top layer of the substrate, while the CSRR is etched in the metallic ground plane on the bottom layer. The introduction of the CSRR defect perturbs the local current distribution in the ground plane, thereby generating a resonant electric response.

The complete equivalent circuit model of the defected-ground CSRR sensor is identical to that of the coaxial-fed loaded-CSRR presented in Fig. 3.1. The resonance condition can therefore be described using the same parallel LC tank model introduced for the coaxial-fed configuration in Section 3.2. When the CSRR is positioned in close proximity to the *stratum corneum*, the surrounding dielectric environment alters the electric field distribution within the slot regions. This dielectric loading effect, analogous to that described for the coaxial-fed CSRR, can be modeled in the equivalent circuit as an additional capacitance C_{load}, placed in parallel with the intrinsic resonator capacitance, C_{eq}. Consequently, the effective capacitance increases, and the resonance frequency shifts accordingly. An increase in the effective permittivity of the SC leads to an higher equivalent capacitance, resulting to a downward of the resonance frequency. Conversely, structural disruptions caused by AD, such as fissures in the SC, reduce the effective permittivity within the gap region. This reduction in capacitive loading leads to a shift of the resonance toward higher frequencies.

Starting from the target operating frequency of 16 GHz, selected to ensure

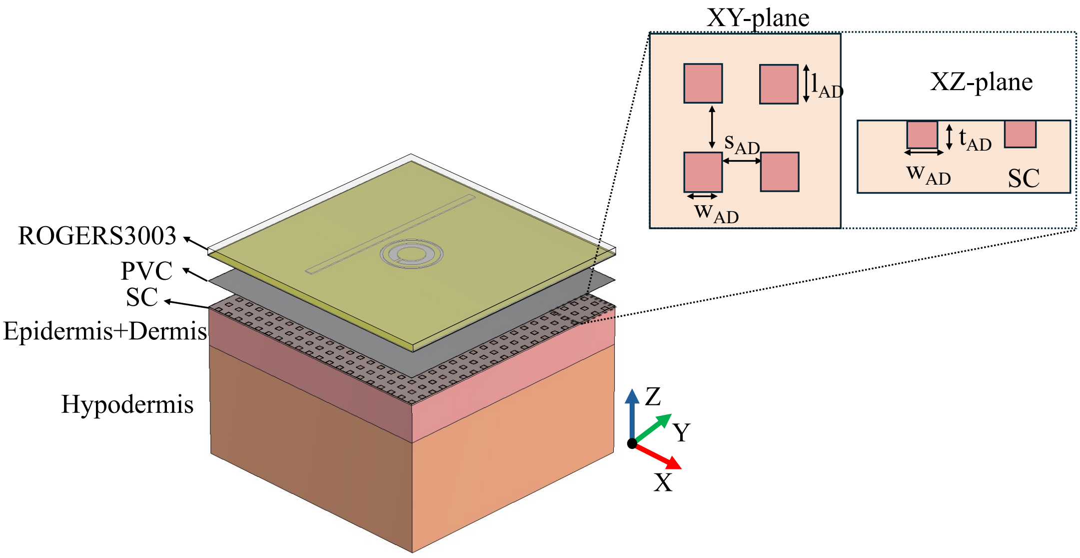

(a)

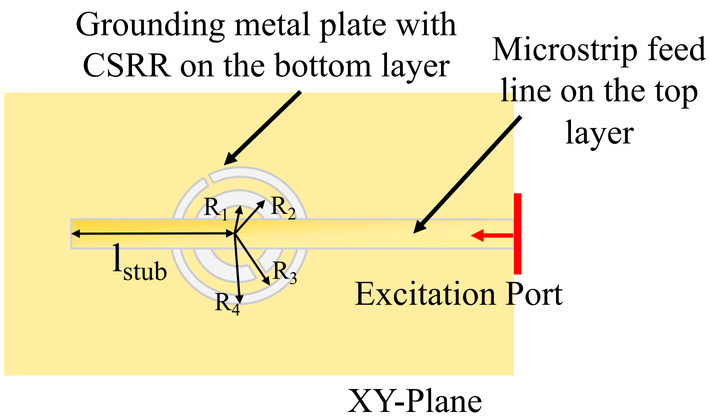

(b)

Figure 4.2: (a) 3D view of the loaded AD sensor, with a schematic of the AD fissures on the SC layer, (b) top view of the proposed AD sensor, showing the CSRR on the bottom layer [18] © 2025 IEEE.

both high surface sensitivity and maintaining a compact footprint, the resonator is initially dimensioned using the parallel LC model to estimate the required effective inductance and capacitance. Preliminary geometrical parameters are calculated to position the resonance near 16 GHz under reference loading conditions.

In this phase, the dielectric loading induced by the multilayer skin model and by the PVC isolation layer is considered through effective permittivity approximations. The open-ended microstrip line is tuned to ensure efficient excitation of the CSRR and proper impedance matching. Full-wave electromagnetic simulations are subsequently employed to refine the geometrical parameters and accurately position the resonance at 16 GHz under healthy-skin loading conditions, which is defined as the reference state. The multilayer structure of the resonator is schematically illustrated in Fig. 4.2, along with a 3D representation of the skin slab used in EM simulations, which acts as the resonator load. The CSRR is etched on the bottom layer of the sensor and positioned to interact with the upper skin layer, where fissures of varying thickness (t_{AD}), and width (w_{AD}) appear depending on the severity of the dermatitis. To ensure a non-contact configuration, a $10\,\mu$m polyvinyl chloride (PVC) layer is inserted between the skin slab and the resonator. This layer provides electrical isolation while maintaining sufficient electromagnetic coupling. The planar sensor is designed to maintain full contact with the skin, without any air gap, because the rapid decay of the E-field within the skin slab means that any air gap between the PVC and the resonator could affect the sensor read-out. Therefore, firm adhesion between the device and the skin is essential to ensure accurate detection. The final design parameters are summarized in Table 4.1, with all dimensions in mm.

R_1	R_2	R_3	R_4	GAP	l_{stub}
0.5	0.8	1.0	1.1	0.1	3.0

Table 4.1: CSRR-based sensor geometrical dimensions.

The electrical and geometrical properties of the multilayer skin model are obtained from literature [61, 62], and derived for the adopted operating frequency using the Djordjevic–Sarkar dispersion model, as reported in Table 4.2. During the design phase, a representative healthy skin model, without AD-related fissures, is first adopted as the sensor load to establish the reference response.

Skin Layer	**Thickness (mm)**	ε'	σ **(S/m)**
SC	0.015	3.9	0.65
Epidermis	0.05	23.4	15.19
Dermis	1.4	23.4	15.19
Hypodermis	4.3	6.51	4.4

Table 4.2: Geometric and electric properties of the skin slab at 16 GHz.

Full-wave electromagnetic simulations, performed in CST Studio Suite, are conducted to evaluated both the reflection coefficient at the excitation port and the E-field penetration of the loaded-resonator. Fig. 4.3 shows the reflection coefficient both in magnitude and phase for healthy SC condition. The magnitude exhibits -36 dB at 15.97 GHz,indicating strong coupling and proper impedance matching between the resonator and the dielectric load. The phase shows a rapid transition around the resonance frequency, confirming the resonant behavior of the structure. To verify that the electric field excited by the CSRR interacts exclusively with the superficial, non-vascularized layers of the skin, the mean norm of the electric field, taken over an XY area approximately corresponding to the square circumscribed around the CSRR, is computed over a set of discrete XY-planes at various depths z_k along the Z-direction. The normalized mean field norm is computed as in Eq. 2.2.

The results, depicted in Fig. 4.4, confirm that the E-field intensity is maximum at the interface between the resonator and the PVC layer, decreasing by approximately 20% at the SC interface. Within the SC, the E-field intensity drops by 50%, and beyond a penetration depth of about 30 μm, the mean E-field norm is reduced to 10% of its maximum value. This result confirms that the sensor is able to selectively probe the SC, while remaining insensitive to the deeper, vascularized layers.

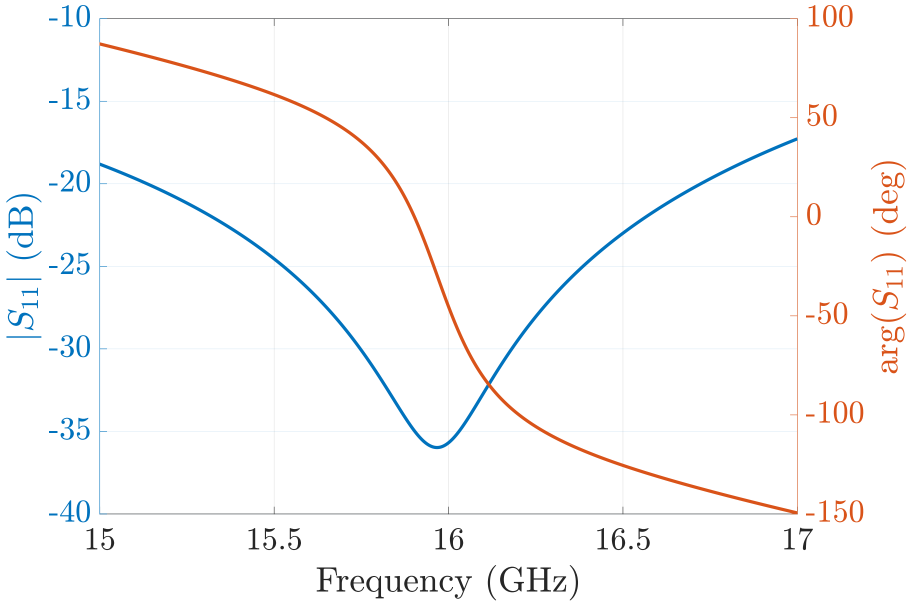

Figure 4.3: Magnitude and phase of the S_{11} for the CSRR-based sensor loaded with the multilayer skin model, considering a healthy SC [18].

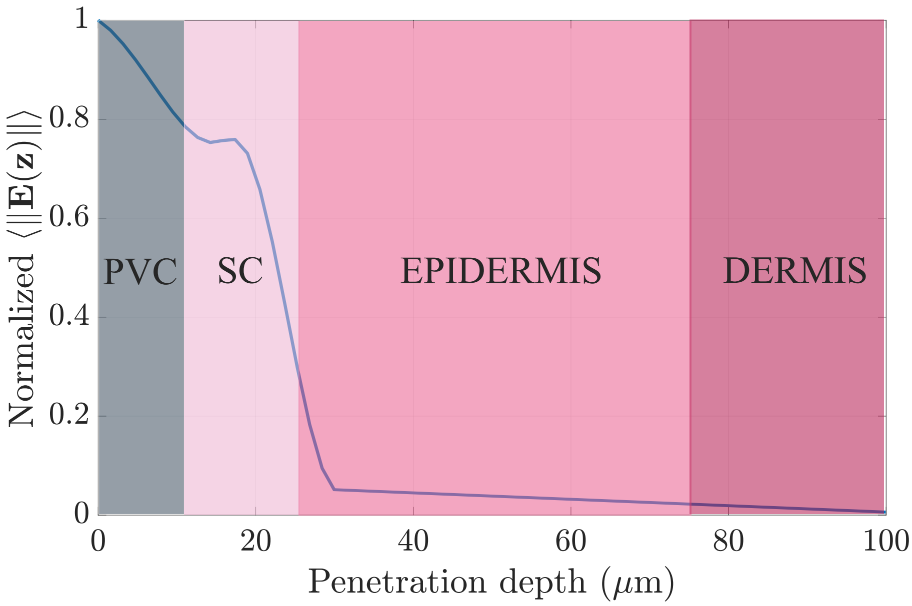

Figure 4.4: EM simulated mean value of the normalized E-field norm along the penetration direction for the healthy skin case. The plot is limited to $z_k = 100\,\mu$m, as the E-field becomes negligible at greater penetration depths [18] © 2025 IEEE.

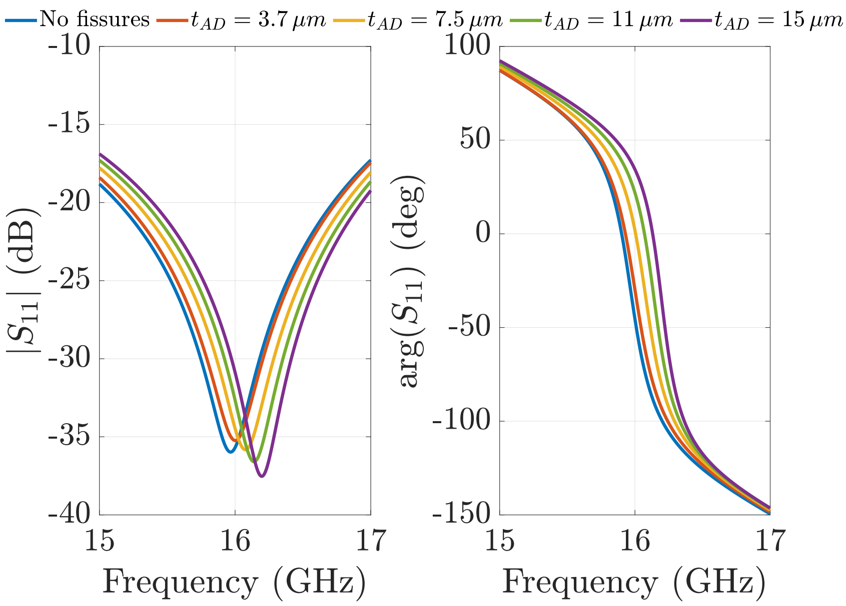

Figure 4.5: Predicted S_{11} of the CSRR resonator loaded with SC exhibiting fissures of varying thickness, with the healthy skin condition included for reference [18]
© 2025 IEEE.

4.3 EM Simulation of the Atopic Dermatitis Sensor: Detection Principle and Sensitivity Analysis

This section presents the electromagnetic response of the CSRR-based sensor interacting with *stratum corneum* affected by atopic dermatitis. The analysis focuses on how variations in fissure thickness (t_{AD}) and width (w_{AD}) affect the sensor's reflection coefficient and E-field distribution within the multilayer skin model. By systematically modifying the SC to emulate AD-induced fissures, the study evaluates the sensor's ability to discriminate between different severities of AD, while confirming that deeper vascularized layers, dermis and hypodermis, have negligible influence on its response. In the EM simulations, AD-affected SC regions are represented as small air cavities, corresponding to fissures of varying geometry.

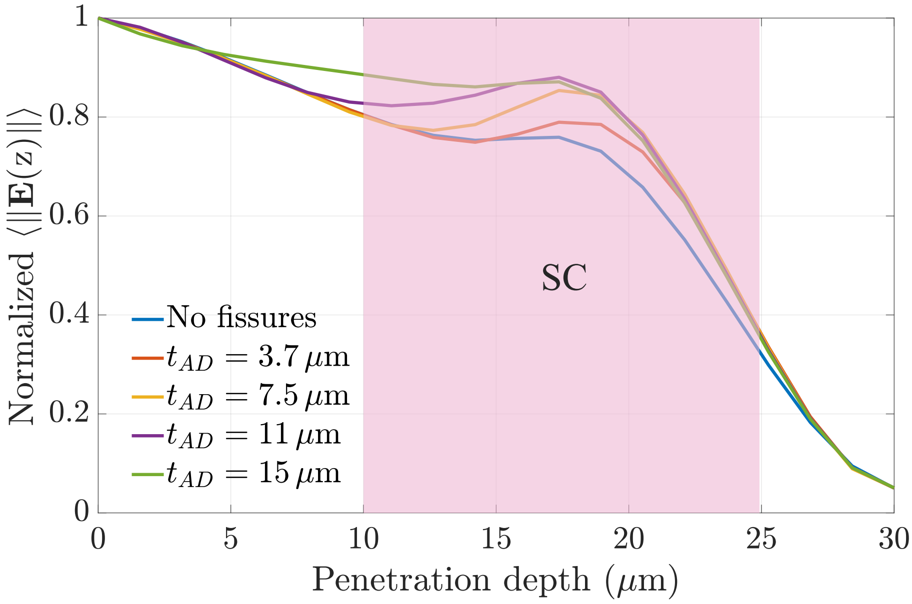

Figure 4.6: Normalized mean E-field norm along the first 30 μm of the skin layer, obtained from EM simulations, for varying fissure thicknesses [18] © 2025 IEEE.

EM simulations are first carried out to investigate the behavior of both the reflection coefficient and the mean E-field norm as function of the SC fissure thickness. In this analysis, t_{AD} is varied form 0 to 15 μm, representing the transition from healthy skin to fully damaged SC. The fissure width and length are fixed to 200 μm. Fig. 4.5 shows the variation in both the magnitude and phase of S_{11}, highlighting the sensor's high sensitivity to changes in AD severity. Specifically, a monotonic upward shift in the resonance frequency is observed as the fissures increase in thickness: the S_{11} negative peak occurs at 15.97 GHz for healthy skin and shifts to 16.2 GHz for fully damaged SC, corresponding to a frequency shift of 230 MHz. These observations are further supported by the trends of $\langle\|E(z)\|\rangle$ with varying t_{AD}, as shown in Fig. 4.6. The $\langle\|E(z)\|\rangle$ vanishes beyond the SC even in AD-affected skin, confirming that deeper vascularized layers have negligible impact on the sensor response. Moreover, increased t_{AD}, associated with deeper fissures, reduces the effective conductivity of the SC, allowing the E-field to penetrate more

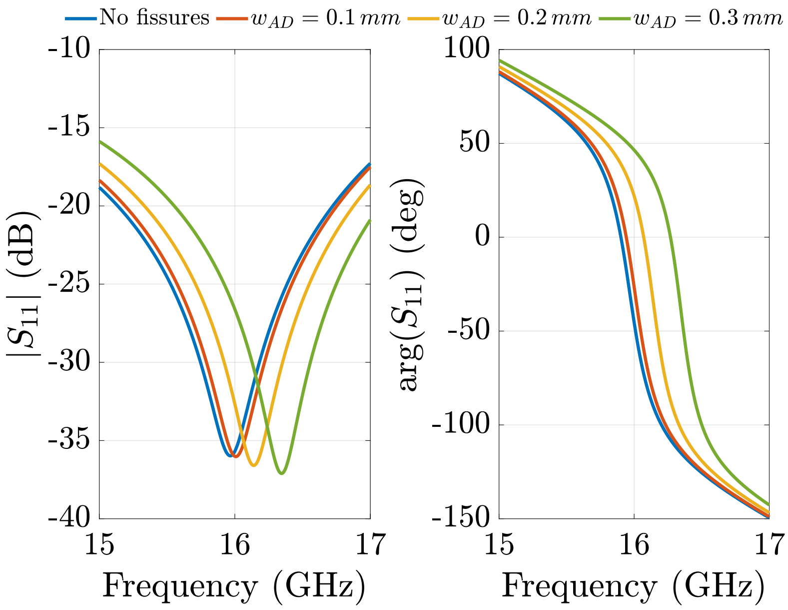

Figure 4.7: Predicted S_{11} of the CSRR resonator loaded with SC exhibiting fissures of varying width, with the healthy skin condition included for reference [18] © 2025 IEEE.

deeply into the superficial layers.

After validating the sensor concept for variations in fissure thickness, an additional set of simulation is carried out to further assess its response to lateral geometrical changes. This analysis aims to confirm the sensor's capability to detect three-dimensional variations in fissure geometry, thereby providing a more comprehensive validation of its electromagnetic sensitivity. In this case, the fissure length and thickness are fixed at $l_{\mathrm{AD}} = 200\,\mu\mathrm{m}$ and $t_{\mathrm{AD}} = 11\,\mu\mathrm{m}$, respectively, while the fissure width (w_{AD}) is varied to evaluate its effect on the sensor's S_{11} and $\langle \|E(z)\| \rangle$. Fig. 4.7 presents the predicted S_{11} for w_{AD} ranging from 0.1 mm to 0.3 mm, highlighting the sensor's capability to detect AD-induced fissures with varying lateral dimensions within the SC. A clear upshift in the resonant frequency is observed with increasing fissure width: from 16 GHz for a $w_{\mathrm{AD}} = 0.1\,\mathrm{mm}$ to 16.15 GHz for $w_{\mathrm{AD}} = 0.3\,\mathrm{mm}$, corresponding to a 150 MHz shift. As in the case of thickness variations, similar trends in the E-field distribution are observed, as shown in Fig.4.8.

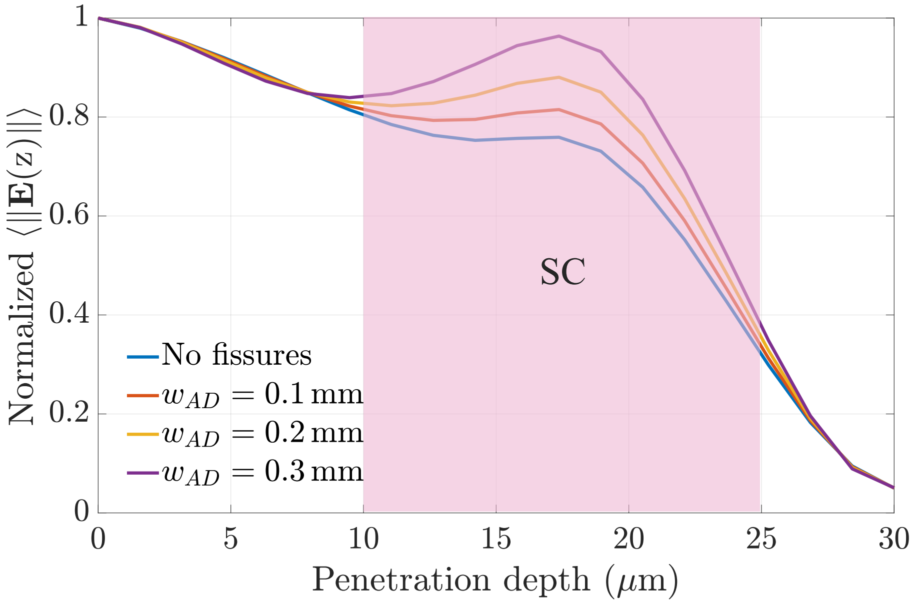

Figure 4.8: Normalized mean E-field norm along the first 30 μm of the skin layer, obtained from EM simulations, for varying fissure width [18] © 2025 IEEE.

Wider fissures lead to a deeper field penetration within the skin slab, due to the enhanced coupling between the resonator and the larger air-filled regions. This selective dependence of the EM response on fissure geometry confirms the sensor's capability of distinguishing different AD severities.

The sensitivity of the CSRR-based sensor to changes in the *stratum corneum* fissure geometry is systematically evaluated. For a generic geometrical parameter d, in this case fissure thickness t_{AD} or fissure width w_{AD}, the sensor sensitivity S_d is defined as the ratio of the change in resonant frequency to the corresponding variation in the parameter:

$$S_d = \frac{\Delta f_{\text{res}}}{\Delta d} = \frac{f_{\text{res},i+1} - f_{\text{res},i}}{d_{i+1} - d_i} \quad [\text{MHz}/\mu\text{m}] \tag{4.1}$$

where $f_{\text{res},i+1}$ and $f_{\text{res},i}$ are the sensor resonant frequencies corresponding to two consecutive values of the geometrical parameter d. In the proposed analysis, a step size of 1 μm is used for t_{AD} and 10 μm for w_{AD}.

EM simulations demonstrate that the sensor exhibits high sensitivity to both thickness and width variations of fissures. Specifically, the worst-case sensitivity values are found to be $S_{t_{AD}} = \frac{15\text{ MHz}}{1\,\mu\text{m}}$ and $S_{w_{AD}} = \frac{1\text{ MHz}}{1\,\mu\text{m}}$, confirming the sensor's ability to accurately detect microscopic structural changes in the SC. These results indicate that the proposed sensor is well suited for the quantitative assessment of AD severity, providing a robust metric for distinguishing between fissures of different geometries and enhancing its applicability in real-time skin condition monitoring.

4.4 Conclusion of the Chapter

This chapter presented the design and electromagnetic evaluation of a miniaturized CSRR-based sensor for the detection of atopic dermatitis. Operating in the Ku-band, the sensor confines the fringing E-field to the *stratum corneum*, where AD-related biomarkers are located, effectively isolating the response from deeper vascularized layers. The sensor concept is thoroughly assessed through full-wave EM simulations, analyzing the impact of fissures in the *stratum corneum* by systematically varying their thickness and width. A multilayer skin model, comprising the *stratum corneum*, epidermis, and dermis, with real geometric and dielectric properties, is adopted to ensure accurate representation of the biological load. The high operating frequency is chosen not only to enhance the spatial resolution of the measurements but also to restrict the sensing to superficial layers, enabling selective detection. The proposed sensor demonstrates high sensitivity, with measured frequency shift of $\frac{15\text{ MHz}}{\mu\text{m}}$ and $\frac{1\text{ MHz}}{\mu\text{m}}$ for fissure thickness and width variations, respectively. These results confirm the capability of the device to detect microscopic structural changes in the *stratum corneum*, highlighting its potential as a reliable tool for non-invasive AD assessment. The CSRR-based sensor is compact, lightweight, and easily miniaturized, and its design can be extended to detect other skin pathologies affecting the *stratum corneum.* This study shows that combining resonators with high-frequency electromagnetic sensing offers an effective and reliable approach for selective and sensitive skin diagnostics.

Conclusion

This Thesis has presented the design, development, and validation of innovative microwave sensing devices based on resonance techniques, addressing the growing requirements for low-cost, small, and stand-alone diagnostic tools in both environmental and biological applications. The common thread across all the proposed solutions is that they are autonomous, non-invasive, adaptive, and accurate, sometimes further enhanced by the synergy between resonant electromagnetic structures and data-driven algorithms. The presented research demonstrates that, by tailoring the resonator's operating frequency and geometry to the specific penetration depth required by the application, it is possible to achieve selective and reliable material characterization without the need for complex and bulky RF instrumentation.

In the first part of this work, a self-oscillating antenna-based sensor operating in the 2.4 GHz band is developed for the non-invasive monitoring of tree trunk moisture content. The sensor exploits the nonlinear steady-state behavior of the self-oscillating antenna to infer variations in the wood's dielectric properties directly from DC measurements. This approach removes the need for external RF instrumentation, thereby simplifying the measurement setup and minimizing power consumption, which enables fully stand-alone operation. The integration with a PLSR predictive model led to a compact, energy-efficient, and autonomous sensing platform. Experimental validation of the prototype confirms its suitability for distributed environmental monitoring and IoT-based smart agriculture system.

Then, a study on microwave sensor architectures for non-invasive and electrode-free skin hydration monitoring is presented. A CSRR operating at 2.4 GHz is designed and fabricated on a low-cost FR4 substrate, achieving compactness and mechanical robustness. The integration with multivariate statistical models proved the system's ability to accurately detect and track skin-hydration levels over time. These results underline the potential of combining resonant microwave sensing with data analytics to achieve continuous and autonomous assessment of physiological parameters in real-world conditions.

Finally, the study extends resonance-based sensing to high-frequency biomedical diagnostics, introducing a miniaturized CSRR-based sensor operating in the Ku-band for AD detection. By confining the E-field within the superficial, non-vascularized skin layer, the *stratum corneum*, the sensor achieved high spatial resolution and selective sensitivity to microstructural fissures associated with AD. The numerical analysis, revel the system's capability to detect microscopic changes in fissure thickness and width, confirming its potential for non-invasive and high-resolution dermatological diagnostics. A prototype of this Ku-band resonator is under construction at the time of this Thesis writing.

Overall, this Thesis work shows that resonance-based microwave sensing is a versatile and scalable approach for diagnostics. The proposed systems share the advantages of compactness, cost-effectiveness, non-invasiveness, and the ability to operate without the need for complex RF equipment. Moreover, the integration with machine learning enables the development of intelligent and autonomous sensing systems.

I am grateful to the Reviewers Prof. Maurizio Bozzi from the University of Pavia and Prof. Almudena Suarez Rodriguez from the University of Cantabria for the time and effort devoted to assessing this thesis, and for their insightful and constructive comments, which have helped strengthen and refine the manuscript.

Bibliography

[1] K. K. Adhikari and N. -Y. Kim, "Ultrahigh-Sensitivity Mediator-Free Biosensor Based on a Microfabricated Microwave Resonator for the Detection of Micromolar Glucose Concentrations," in *IEEE Transactions on Microwave Theory and Techniques*, vol. 64, no. 1, pp. 319-327, Jan. 2016.

[2] O. Peytral-Rieu, D. Dubuc and K. Grenier, "Microwave-Based Sensor for the Noninvasive and Real-Time Analysis of 3-D Biological Microtissues: Microfluidic Improvement and Sensitivity Study," in *IEEE Transactions on Microwave Theory and Techniques*, vol. 71, no. 11, pp. 4996-5003, Nov. 2023.

[3] Y. Xiong, Z. Liu, S. Li, G. Meng and Z. Peng, "Scanning Microwave Vibrometer: Full-Field Vibration Measurement via Microwave Sensing With Phase-Encoded Beam Scanning," in *IEEE Transactions on Instrumentation and Measurement*, vol. 72, pp. 1-11, 2023.

[4] C. Wang et al., "High-Accuracy Complex Permittivity Characterization of Solid Materials Using Parallel Interdigital Capacitor- Based Planar Microwave Sensor," in *IEEE Sensors Journal*, vol. 21, no. 5, pp. 6083-6093, 1 March1, 2021.

[5] F. Benassi, G. Paolini, D. Masotti and A. Costanzo, "A Wearable Flexible Energy-Autonomous Filtenna for Ethanol Detection at 2.45 GHz," in *IEEE Transactions on Microwave Theory and Techniques*, vol. 69, no. 9, pp. 4093-4106, Sept. 2021.

[6] N. Javanbakht, G. Xiao and R. E. Amaya, "Portable Microwave Sensor Based on Frequency-Selective Surface for Grain Moisture Content Monitoring," in *IEEE Sensors Letters*, vol. 5, no. 11, pp. 1-4, Nov. 2021.

[7] J. Guo, Y. Tang, Y. Wu, C. Zhu and J. Huang, "Embeddable Soil Moisture Content Sensor Based on Open-End Microwave Coaxial Cable Resonator," in *IEEE Sensors Journal*, vol. 23, no. 12, pp. 13575-13584, 15 June15, 2023.

[8] A. Di Florio Di Renzo et al., "A Stand-Alone Moisture Content Sensor Based on a Loaded Self-Oscillating Antenna," in *2024 IEEE/MTT-S International Microwave Symposium - IMS 2024*, Washington, DC, USA, 2024, pp. 284-287.

[9] A. Di Florio Di Renzo, S. Trovarello, O. Afif, M. Tartagni, D. Masotti, and A. Costanzo, "A Predictive-Model-Assisted Moisture Content Sensor by Monitoring the DC-Unstable States of a Microwave Self-Oscillating Antenna," in *IEEE Transactions on Microwave Theory and Techniques*, vol. 73, no. 8, pp. 5580–5591, Aug. 2025.

[10] L. Peng et al., "A Fused Learning and Enhancing Method for Accurate and Noninvasive Hydration Status Monitoring With UWB Microwave Based on Phantom," in *IEEE Transactions on Microwave Theory and Techniques*, vol. 71, no. 9, pp. 4027–4036, Sept. 2023.

[11] A. Cataldo et al., "Portable Microwave Reflectometry System for Skin Sensing," in *IEEE Transactions on Instrumentation and Measurement*, vol. 71, pp. 1–8, 2022.

[12] S. Bing, K. Chawang, and J.-C. Chiao, "A Flexible Tuned Radio-Frequency Planar Resonant Loop for Noninvasive Hydration Sensing," in *IEEE Journal of Microwaves*, vol. 3, no. 1, pp. 181–192, Jan. 2023.

[13] S. Trovarello, O. Afif, A. Di Florio Di Renzo, D. Masotti, M. Tartagni and A. Costanzo, "A Non-Invasive, Machine Learning Assisted Skin-Hydration Microwave Sensor," in *2024 54th European Microwave Conference (EuMC)*, Paris, France, 2024, pp. 932-935.

[14] O. Afif, A. Di Florio Di Renzo, S. Trovarello, A. Costanzo, and M. Tartagni, "Boosting Microwave Hydration Sensors Performance with Machine Learning Techniques," in *2024 International Microwave and Antenna Symposium (IMAS)*, Marrakech, Morocco, 2024, pp. 1–4.

[15] Elias PM. The skin barrier as an innate immune element. Semin Immunopathol. 2007 Apr;29(1):3-14.

[16] A. Rizwan et al., "Non-Invasive Hydration Level Estimation in Human Body Using Galvanic Skin Response," in IEEE Sensors Journal, vol. 20, no. 9, pp. 4891-4900, 1 May1, 2020.

[17] Huang X, Cheng H, Chen K, Zhang Y, Zhang Y, Liu Y, Zhu C, Ouyang SC, Kong GW, Yu C, Huang Y, Rogers JA. Epidermal impedance sensing sheets for precision hydration assessment and spatial mapping. IEEE Trans Biomed Eng. 2013 Oct;60(10):2848-57.

[18] A. Di Florio Di Renzo, S. Trovarello, D. Masotti, M. Tartagni, and A. Costanzo, "Atopic Dermatitis Detection with a Compact Ku-Band CSRR-Based Sensor," in *2025 IEEE International Conference on RFID Technology and Applications (RFID-TA)*, Valence, France, 2025, pp. 1-4.

[19] S. Kim et al., "Ambient RF Energy-Harvesting Technologies for Self-Sustainable Standalone Wireless Sensor Platforms," in *Proceedings of the IEEE*, vol. 102, no. 11, pp. 1649-1666, Nov. 2014.

[20] Marina Vera Zambrano, Baishali Dutta, Donald G. Mercer, Heather L. MacLean, Marianne F. "Touchie, Assessment of moisture content measurement methods of dried food products in small-scale operations in developing countries: A review", in *Trends in Food Science & Technology*, Volume 88, 2019, Pages 484-496.

[21] A. Joshi, D. P. Kanungo and R. K. Panigrahi, "Multi-Frame Fringing Field Capacitive Soil Moisture Sensor With Enhanced Sensitivity and Penetration Depth," in *IEEE Transactions on Instrumentation and Measurement*, vol. 73, pp. 1-13, 2024.

[22] C. -H. Pai and C. -H. Tseng, "A New Microwave Oscillator-Based Microfluidic Sensor for Complex Permittivity Measurement," in *2023 IEEE/MTT-S International Microwave Symposium - IMS 2023*, San Diego, CA, USA, 2023, pp. 967-970.

[23] V. Sekar, W. J. Torke, S. Palermo and K. Entesari, "A Self-Sustained Microwave System for Dielectric-Constant Measurement of Lossy Organic Liquids," in *IEEE Transactions on Microwave Theory and Techniques*, vol. 60, no. 5, pp. 1444-1455, May 2012.

[24] Z. Cao, Z. Lu, P. Liu and J. Tan, "Nondestructive Microwave Self-Oscillating Sensor Based on Complementary Spiral Resonator for Defect Evaluation of Metallic Mesh," in *IEEE Transactions on Microwave Theory and Techniques*, vol. 72, no. 3, pp. 1754-1765, March 2024.

[25] G. Paolini, M. Shanawani, D. Masotti, D. M. M. . -P. Schreurs and A. Costanzo, "Respiratory Activity Monitoring by a Wearable 5.8 GHz SILO With Energy Harvesting Capabilities," in *IEEE Journal of Electromagnetics, RF and Microwaves in Medicine and Biology*, vol. 6, no. 2, pp. 246-252, June 2022.

[26] C. -H. Tseng and C. -Z. Wu, "A Novel Microwave Phased- and Perturbation-Injection-Locked Sensor With Self-Oscillating Complementary Split-Ring Resonator for Finger and Wrist Pulse Detection," in *IEEE Transactions on Microwave Theory and Techniques*, vol. 68, no. 5, pp. 1933-1942, May 2020.

[27] T. Sokoll and A. F. Jacob, "Self-Oscillating Measurement System for In Situ-Monitoring Moisture in Buildings," in *IEEE Transactions on Instrumentation and Measurement*, vol. 63, no. 12, pp. 2911-2918, Dec. 2014.

[28] J. F. Cadima and I. T. Jolliffe, "Size-and shape-related principal com- ponent analysis," in *Biometrics*, pp. 710–716, 1996.

[29] G. Luciani, A. Berardinelli, M. Crescentini, A. Romani, M. Tartagni, and L. Ragni, "Non-invasive soil moisture sensing based on open-ended waveguide and multivariate analysis," in *Sensors and Actuators A: Physical*, vol. 265, pp. 236–245, 2017.

[30] O. Afif, L. Franceschelli, E. Iaccheri, S. Trovarello, A. Di Florio Di Renzo, L. Ragni, A. Costanzo, and M. Tartagni, "A versatile, machine-learning-enhanced rf spectral sensor for developing a trunk hydration monitoring system in smart agriculture," in *Sensors*, vol. 24, no. 19, p. 6199, 2024.

[31] Razafindratsima, S., Sbartaï, Z.M. & Demontoux, F. "Permittivity measurement of wood material over a wide range of moisture content", in *Wood Sci Technol*, 51, 1421–1431 (2017).

[32] V. Rizzoli, A. Costanzo, F. Mastri, C. Cecchetti, "Harmonic-balance optimization of microwave oscillators for electrical performance, steady-state stability, and near-carrier phase noise," in *(1994) IEEE MTT-S IMS*, pp. 1401 – 1404, 1994.

[33] V. Rizzoli, D. Masotti and A. Costanzo, "Behavioural Models of Injection-Locked Self-Oscillating Microstrip Antennas for Multimedial Communications Systems," in *2003 33rd European Microwave Conference*, Munich, Germany, 2003, pp. 499-502, 2003.

[34] V. Rizzoli, and A. Costanzo, "Accurate bilateral FET model suitable for general nonlinear and power applications" in *International Journal of RF and Microwave Computer-Aided Engineering*, Wiley, 2000.

[35] M. Golio, "The push toward low voltage devices," in *IEEE Microwave Magazine*, vol. 1, no. 1, pp. 38-45, March 2000.

[36] "Modern Harmonic-Balance Techniques for Oscillator Analysis and Optimization," in *RF and Microwave Oscillator Design.*

[37] Dietsch, P., Franke, S., Franke, B. et al., "Methods to determine wood moisture content and their applicability in monitoring concepts, in *J Civil Struct Health Monit*, 5, 115–127 (2015).

[38] Bishop, C. M., & Nasrabadi, N. M., in *Pattern recognition and machine learning*, Vol. 4, No. 4, p. 738, 2006.

[39] S. Wold, M. Sj¨ostr¨om, and L. Eriksson, "Pls-regression: a basic tool o chemometrics," in *Chemometrics and intelligent laboratory systems*, vol. 58, no. 2, pp. 109–130, 2001.

[40] H. Wold, “Path Models with Latent Variables: The NIPALS Approach,” in *Quantitative Sociology*, Elsevier, 1975, pp. 307–357.

[41] H. M. Logan-Sprenger, G. J. Heigenhauser, G. L. Jones, and L. L. Spriet, "The effect of dehydration on muscle metabolism and time trial performance during prolonged cycling in males," in *Physiological Reports*, vol. 3, no. 8, e12483, Aug. 2015.

[42] G. Arnaoutis and P. Neophytou, "The Effect of Acute Dehydration upon Muscle Strength Indices at Elite Karate Athletes: A Randomized Crossover Study," in *Nutrients*, vol. 17, 1452, 2025.

[43] O. R. Barley, D. W. Chapman, A. J. Blazevich, and C. R. Abbiss, "Acute Dehydration Impairs Endurance Without Modulating Neuromuscular Function," in *Frontiers in Physiology*, vol. 9, 1562, Nov. 2018.

[44] InBody Co., Ltd., "InBody Official Website," *InBody*, 2025.

[45] C. Gocen and M. Palandoken, "Machine Learning Assisted Novel Microwave Sensor Design for Dielectric Parameter Characterization of Water–Ethanol Mixture," in *IEEE Sensors Journal*, vol. 22, no. 3, pp. 2119–2127, Feb. 1, 2022.

[46] N. Kazemi, M. Abdolrazzaghi and P. Musilek, "Comparative Analysis of Machine Learning Techniques for Temperature Compensation in Microwave Sensors," in *IEEE Transactions on Microwave Theory and Techniques*, vol. 69, no. 9, pp. 4223–4236, Sept. 2021.

[47] T. Reimer and S. Pistorius, "The Diagnostic Performance of Machine Learning in Breast Microwave Sensing on an Experimental Dataset," in *IEEE Journal of Electromagnetics, RF and Microwaves in Medicine and Biology*, vol. 6, no. 1, pp. 139–145, March 2022.

[48] A. E. Omer, G. Shaker and S. Safavi-Naeini, "Portable Radar-Driven Microwave Sensor for Intermittent Glucose Levels Monitoring," in *IEEE Sensors Letters*, vol. 4, no. 5, pp. 1–4, May 2020.

[49] A. Cataldo, E. De Benedetto, R. Schiavoni, G. Monti, A. Tedesco, A. Masciullo, E. Piuzzi and L. Tarricone, "Portable Microwave Reflectometry System for Skin Sensing," in *IEEE Transactions on Instrumentation and Measurement*, vol. 71, pp. 1–8, 2022.

[50] J. Kilpijärvi, J. Tolvanen, J. Juuti, N. Halonen, and J. Hannu, "A Non-Invasive Method for Hydration Status Measurement With a Microwave Sensor Using Skin Phantoms," *IEEE Sensors Journal*, vol. 20, no. 2, pp. 1095–1104, Jan. 15, 2020.

[51] E. Jones, H. N. Mughal, R. Moscalu, M. Columb, C. Duff, M. Dickinson, A. J. Reid and R. N. A. Murphy, "Quantification of Palmar and Digital Epidermal Thickness and Sweat Duct Density," *Clinical Anatomy*, online ahead of print, Jun. 4, 2025.

[52] J. Kilpijärvi, J. Tolvanen, J. Juuti, N. Halonen and J. Hannu, "A Non-Invasive Method for Hydration Status Measurement With a Microwave Sensor Using Skin Phantoms," in *IEEE Sensors Journal*, vol. 20, no. 2, pp. 1095–1104, Jan. 15, 2020.

[53] P. A. Hasgall, F. Di Gennaro, C. Baumgartner, E. Neufeld, B. Lloyd, M.-C. Gosselin, D. Payne, A. Klingenböck and N. Kuster, "IT'IS Database for Thermal and Electromagnetic Parameters of Biological Tissues," Version 4.1, Feb. 22, 2022.

[54] S. Wold, K. Esbensen and P. Geladi, "Principal Component Analysis," in *Chemometrics and Intelligent Laboratory Systems*, vol. 2, no. 1–3, pp. 37–52, 1987.

[55] L. Franceschelli, M. A. Casu, G. Mazzarella, F. Montisci, G. Montisci and M. Mussetta, "Non-Intrusive Microwave Technique for Direct Detection of Concrete Compressive Strength Monitoring by Multivariate Modeling," in *Measurement*, vol. 206, p. 112332, Jan. 2023.

[56] J. Kilpijärvi, J. Tolvanen, J. Juuti, N. Halonen and J. Hannu, "A Non-Invasive Method for Hydration Status Measurement With a Microwave Sensor Using Skin Phantoms," in *IEEE Sensors Journal*, vol. 20, no. 2, pp. 1095–1104, Jan. 15, 2020.

[57] M. Baghelani, Z. Abbasi, M. Daneshmand and P. E. Light, "Noninvasive Microwave Sensor for Real-Time Continuous Dehydration Monitoring," in *IEEE Sensors Journal*, vol. 24, no. 7, pp. 9959–9969, Apr. 1, 2024.

[58] A. I. Sunny, M. P. Chowdhury, P. K. Biswas, D. K. Paul and E. K. Yeasmin, "Feasibility Experiments to Detect Skin Hydration Using a Bio-Impedance Sensor," in *Proceedings of the 41st Annual International Conference of the IEEE Engineering in Medicine and Biology Society (EMBC)*, Berlin, Germany, 2019, pp. 6032–6035.

[59] S. Bing, K. Chawang and J.-C. Chiao, "A Flexible Tuned Radio-Frequency Planar Resonant Loop for Noninvasive Hydration Sensing," in *IEEE Journal of Microwaves*, vol. 3, no. 1, pp. 181–192, Jan. 2023.

[60] A. R. Todorov, M. Z. Turaev, L. K. Ivanov, D. S. Petrov and P. N. Dimitrov, "Design of a Flexible, Wearable Interdigitated Capacitive Sensor for Monitor-

ing Biomarkers of Atopic Dermatitis," in *IEEE Sensors Journal*, vol. 24, no. 5, pp. 6856–6866, Mar. 1, 2024.

[61] G. Sacco, S. Pisa and M. Zhadobov, "Age-Dependence of Electromagnetic Power and Heat Deposition in Near-Surface Tissues in Emerging 5G Bands," in *Scientific Reports*, vol. 11, p. 3983, 2021.

[62] M. C. Ziskin, S. I. Alekseev, K. R. Foster and Q. Balzano, "Tissue Models for RF Exposure Evaluation at Frequencies Above 6 GHz," in *Bioelectromagnetics*, vol. 39, no. 3, pp. 173–189, 2018.